Finite amplitude solutions in sliding Couette flow(Dissertation_全文)

AUTHOR(S):

Deguchi, Kengo

CITATION:

Deguchi, Kengo. Finite amplitude solutions in sliding Couette flow. 京都大学, 2013, 博士(工学)

ISSUE DATE:

2013-03-25

URL:

https://doi.org/10.14989/doctor.k17559

Finite amplitude solutions in sliding Couette flow

Kengo Deguchi

To

My Mother and the Memories of My Father

Abstract

We exhibit nonlinear studies of sliding Couette flow, the flow between two infinitely long co-axial cylinders generated by the sliding motion of the inner cylinder in the axial direction. As a result, two types of finite-amplitude solutions of the Navier-Stokes equations are discovered.

First we confirm Gittler (1993)'s axisymmetric linear stability result, namely that the flow can be linearly unstable to axisymmetric perturbations when the radius ratio $\eta = a/b$, where a and b denote the radii of the inner and outer cylinders respectively, is smaller than 0.1415. A bifurcation analysis reveals that Tollmien-Schlichting wave like axisymmetric finite-amplitude solutions bifurcate from the basic flow due to this instability. For these obtained numerical equilibrium solutions, the relationship to the theoretical study, valid for asymptotically large values of Reynolds number, R, is discussed. We continue the numerical axisymmetric solution branch, which comes into exist once at $R \sim O(10^4)$, to $R \sim O(10^8)$, and confirm the quantitative agreement with axisymmetric asymptotic theory developed in this thesis. All of these axisymmetric numerical solutions vanish with increasing η in the range $(0.33, 0.40)$, exhibiting a streamwise localized long-wave structure as this cut-off is approached. Consistent with this observation, the asymptotic theory breaks down when the disturbance wavelength is comparable with R.

Secondly, our nonlinear analysis leads to the discovery of non-axisymmetric travelling-wave solutions which appear abruptly at a finite Reynolds number for wide range of η where the linear instability is absent. We also show these solutions of sliding Couette flow can be continued to plane Couette flow, which is the zero-curvature limit of sliding Couette flow. These solutions, including new solutions of plane Couette flow, are characterized by vortex-wave interaction asymptotic theory (Hall & Smith 1991, Hall & Sherwin 2010). We confirm the interaction sustaining solutions is localized at positions at which strong streak shear and outward jets in the roll velocity components are commonly observed. The fact that the interaction can be present for all values of η explains the robustness of the non-axisymmetric solutions against change of geometry. Thanks to this property, it is also possible to find some connections to pipe flow, which is obtained in the limit of vanishing inner cylinder of sliding Couette flow with proper axial pressure gradient.

Acknowledgements

First and foremost I would like to express a deep acknowledgment of thanks to Prof. Dr Masato Nagata, for his marathon supervision. Since he opened the door to such a vast field of interest for me six years ago, his respectable endurance and toughness have illuminated my long journey to this finish line.

I am greatly indebted to Dr Takashi Noguchi and Dr Darren P. Wall, who provided me with a powerful computational environment in which pursue these studies, and whose insightful advise during the course of my doctoral studies broadened my horizons.

My gratitude also extends to Prof. Dr Philip Hall and Dr Andrew G. Walton of Imperial College, London for many stimulating discussions and sharing their expertise with me during my stay. I would like to thank the latter particularly for his valuable input in discussions concerning the present thesis. Special thanks also go to Prof. Dr Richard R. Kerswell of the University of Bristol for his advise.

Furthermore I wish to thank to everyone of my current and former coworkers, rivals and friends who helped me sustain my motivation in various ways - I'm here and now from here on in!

Finally I would like to express sincerest gratitude to my family. This thesis is dedicated to my mother, Takami Deguchi and the memories of my father, Kazuichi Deguchi. I am also grateful to the continuous support of my grandfather, Takaaki Deguchi, and my grandmother, Etsuko Deguchi. Without their help, I could not have made it here.

Kengo Deguchi

'You can't tell until you see a kite caught by one ... an ordinary tree will let a kite go right away but a Kite-eating tree will hang on to a kite for weeks! Any one of these trees could be a monstrous Kite-eating tree ... you just can't tell ...'

Charlie Brown

Contents

List of Figures

List of Tables

Chapter 1

Introduction

1.1 Finite amplitude solutions of shear flows

Fluid motion can be observed in situations as diverse as a cup of coffee to blood circulation in the body. For these flows, it is well known that smooth laminar flow can reach a chaotic turbulent state when the flow speed is sufficiently fast. Although both of the states are effectively modelled by the nonlinear partial differential equations called the Navier-Stokes equations, when and how laminar-turbulent transition occurs is still not well understood.

Laminar-turbulent transition can be realized when a fluid flow experiences a strong shear typically due to the presence of a wall. After the flow reaches a turbulent state, the fluid flow shows a highly unpredictable motion exhibiting high energy and momentum (and heat if included) dissipation and transfer on the wall. The control of such turbulent states is practically important, but the Navier-Stokes equations are too difficult to solve for complex realistic situations. Therefore a number of simple wall bounded configurations, so-called canonical flows, have been studied in order to extract the essential nature of transition phenomena. Such canonical problems include:

- plane Couette flow: a flow between mutually moving two parallel plates,
- pipe flow: a pressure driven flow through a single pipe,

- plane Poiseuille flow: a pressure driven flow between two parallel plates,
- Rayleigh-Benard convection: a fluid layer on a heated horizontal plate,
- Taylor-Couette flow: a flow between independently rotating co-axial cylinders.

For these flows, a speed of fluid relative to a wall is controlled by moving another wall, pressure gradient or buoyancy which can define Reynolds number, i.e. non-dimensional shearing flow speed. One of the most important concerns in laminar-turbulent transition problem is to determine critical Reynolds number for this phenomena.

Laminar flow is obtained as a solution of the linearized Navier-Stokes equations. We can prove this "basic flow" solution exists for all Reynolds number and is unique when the Reynolds number is sufficiently small (Serrin 1959). However, recent advances in computing power allow us to compute nonlinear *finite-amplitude solutions* of the Navier-Stokes equations for sufficiently large values of the Reynolds number. Therefore, these solutions, which take a form of travelling waves, relative periodic orbits or more complex time-dependent orbits, have been attracting attention as a key to understanding turbulent transition.

The fact that such solutions are sometimes unstable and cannot be obtained by simulation requires the use of the Newton iterative method, which is much more computationally expensive than simulation. This leads to the obvious question: how to choose the initial guess for the iteration? Since the flow motion has a very high number of degrees of freedom (e.g. number of grid points needed to resolve the flow field), typically $O(10^3) - O(10^6)$ even for moderate R, any search for a solution with a poor initial guess likely to fail (for example, if we consider three discrete states for each 1000 variables, say corresponding to positive, zero and negative values, there are $3^{1000} = 1.3 \times 10^{477}$ possible initial guesses!).

One possible method to construct an initial guess is the linear instability, i.e. the stability to infinitesimally small disturbances, of the basic flow. We can rewrite the time-dependent Navier-Stokes problem as

$$\frac{d\mathbf{x}}{dt} = \mathbf{L}\mathbf{x} + \mathbf{N}(\mathbf{x}, \mathbf{x})$$

where vector $\mathbf{x}(t)$ represents 'disturbance to the basic flow', whose dimension determines a number of degrees of freedom, and $\mathbf{L}$ and $\mathbf{N}$ are linear and nonlinear operators respectively. For infinitesimally small $\mathbf{x}$, products of the disturbance can be neglected, and so the problem reduces to a linear one and it is possible to set $\mathbf{x} = \Re(\check{\mathbf{x}}e^{st})$ where s is a complex growth rate. The resultant eigenvalue problem

$$s\check{\mathbf{x}} = \mathbf{L}\check{\mathbf{x}}$$

yields an eigenvector $\check{\mathbf{x}}$. In the neighbourhood of linear critical point, where at least one of the eigenvalue satisfies $\mathbb{R}(s) = 0$, the associated eigenvector provides an initial guess fo the nonlinear problem because (i) the Jacobian matrix, which is defined by the action of $\mathbf{L}$ to $\mathbf{x}$, becomes singular implying that the uniqueness of the basic flow solution is not assured (c.f. implicit function theorem), i.e. the *bifurcation* of another solution branch is possible and (ii) the eigenvector $\check{\mathbf{x}}$ approximates the bifurcating finite-amplitude solution near the linear critical point. Successive bifurcating solution branches also can be detected from the finite-amplitude solution branch when the linear and nonlinear part of the equations are rearranged so that $\mathbf{x}(t)$ represents 'disturbance to the finite-amplitude solution'. These bifurcating solutions sometimes break the symmetry of the original solutions and therefore have more complex structures. The successive bifurcations of solutions starting from the linear critical point of the basic solution provide one of route to turbulence, called supercritical transition. This bifurcation scenario successfully explains some transition processes such as those due to convection (e.g. Rayleigh-Benard convection) or rotational instability (e.g. Taylor-Couette flow) for example.

However, for purely shear induced flow, such as plane Couette flow, pipe flow and plane Poiseuille flow, the story is much more complex. One of the theoretical difficulties of shear flow transition problem lies in the linear stability of basic flow, i.e. even when the basic flow is stable to infinitesimal disturbances, transition to turbulence can occur. Thus for this so-called subcritical transition, the dynamics should be fully nonlinear and the final state observed in any experimental or numerical simulation depends on finite-amplitude

initial conditions. This type of transition to chaotic turbulence typically occurs abruptly, as demonstrated by Reynolds' famous pipe flow experiment in 1883. As he observed from a flow visualized by dye, in contrast to supercritical transition, stable coherent states such as travelling waves cannot be realized.

Moreover, it is known that laminar-turbulent transition in shear flows involves two types of distinct vortical structures. The first of these structures arises by consideration of the linear stability of the basic flow at relatively high R. As Tollmien (1929) and Schlichting (1933) found for boundary-layer flow, an infinitesimally small growing mode typically has a two-dimensional orthogonally-aligned roll pattern. As a consequence of this instability the finite-amplitude solution inherits a similar two-dimensional flow structure (Zahn *et al.* 1974, Herbert 1976 for plane Poiseuille flow).

In contrast, experimental results (e.g. Davies & White 1928 and Nishioka *et al.* 1975) and direct Navier-Stokes simulations (e.g. Orszag & Kells 1980 and Henningson *et al.* 1987) indicate that shear flows can lose stability to three-dimensional streamwise roll structures. This second type of flow structure typically occurs at much lower Reynolds numbers than those associated with the two-dimensional linear and corresponding nonlinear disturbances mentioned above. In addition, there exist anomalistic flows which do not exhibit any linear instability: plane Couette flow (Romanov 1973), and pipe flow (Meseguer & Trefethen 2003). Hereinafter we abbreviate these flows as PCF and PF respectively since they are frequently cited in the present thesis.

One possible explanation to resolve this apparent conflict between theories and experiments has been found through the computation of three-dimensional finite-amplitude solutions of the Navier-Stokes equations (e.g. Nagata 1990 and Clever & Busse 1992 for PCF, Faisst & Eckhardt 2003 and Wedin & Kerswell 2004 for PF, Waleffe 1998 for plane Poiseuille flow). These nonlinear states are disconnected from any linear instability and are therefore difficult to obtain. Instead, they appear abruptly by means of a saddle-node bifurcation at values of R as low as that at which the corresponding flow dynamics begin to show instability according to experiments or unsteady Navier-Stokes simulations. Visualiza-

tions of such solutions reveal that they commonly have similar flow structures including quasi-streamwise rolls and streaks, as are frequently observed in flows in laminar-turbulent transitions of shear flows. For this reason, these travelling wave solutions are sometimes termed "exact coherent structures".

To obtain nonlinear solutions that do not arise from linear instability, related problems, such as those that include additional forces (whether physical or non-physical) or different boundary conditions may be considered. Such augmented systems typically have linear instabilities. Solutions to the original problem may then be obtained by continuing in small steps from the problem that includes the additional effects by applying the Newton-Raphson iterative method. This is the so-called *homotopy method*, and has been widely used to obtain solutions of nonlinear systems, for example those arising in electrical circuit problems (e.g. Melville *et al.* 1993) and economic problems (e.g. Judd *et al.* 2000). Nevertheless, the success of the homotopy continuation from one solution to another is not always assured, and thus the choice of additional effects is crucial importance.

This difficulty has been resolved by Waleffe (1995, 1998) for shear flows, revealing the physical mechanism of coherent structures as follows: small streamwise rolls create an inhomogeneous streamwise mean flow, i.e. streaks, and then linear instability of the streaks excites sinuous waves. Finally the rolls gain energy from the waves and so on. This successive interaction of rolls, streaks and waves is now called Waleffe's self sustaining process (SSP). He showed that the choice of additional effect as an artificial forcing term that mimics streak instability in SSP is a promising way to obtain exact coherent structures.

1.2 Role of solutions in dynamics

These finite-amplitude solutions provide a stepping stone to understanding subcritical shear flow transition phenomena in terms of a dynamical systems theory context. In this theory, we consider the dynamics of a flow as a trajectory in phase space spanned by each element of $\mathbf{x}(t)$. Thus for a subcritical shear-flow transition problem, this trajectory is attracted to

either the basic flow or a turbulent state depending on the given condition.

From linear stability theory we know that all small-amplitude disturbances decay to the basic flow, while large-amplitude disturbances could trigger transition. For subcritical transition an 'edge state' approach has been developed that, for given initial conditions, seeks to control the amplitude of the disturbance in simulations so that the flow neither becomes turbulent nor returns to the laminar basic flow. These studies showed that the so-called lower-branch of three-dimensional solutions, which typically produce a smaller modification to the basic flow than other solution branches, are frequently found in the resultant trajectory, i.e. the edge of laminar-turbulent attractor (e.g. Itano & Toh 2001 and Skufca, Yorke & Eckhardt 2006). Thus lower-branch states are considered to be embedded in this edge state and play a 'gatekeeper' role in the transition dynamics. Though these edge states are obtained by a numerical approach, a recent study has revealed that they can indeed be observed in real controlled experimental flows (de Lozar *et al.* 2012).

An alternative approach to understanding subcritical transition is provided by Gibson *et al.* (2007), who projected the finite-amplitude solutions and turbulent trajectory onto a carefully chosen low-dimensional phase space and showed that the turbulent trajectory hangs around for a long time in the neighborhood of certain finite-amplitude solutions. Gibson *et al.* (2007) explains this behaviour with reference to the property that only have a few unstable eigenvalues. This means that a given trajectory in phase space is pulled away from such solution in a few directions while it is attracted to such a solution in the other $O(10^3)$–$O(10^6)$ directions. Gibson *et al.* (2007) also computed unstable manifolds, which can be obtained from time marching from linearly unstable eigenvectors of the solution, and found that trajectories near the solution are repelled away, guided by the unstable manifold.

Though above picture is based on travelling wave solutions which are regarded as fixed points in the state space in some sense, time periodic solutions also play a crucial role in turbulence according to periodic orbit theory by Civitanović *et al.* (2011), in which chaotic dynamics can be approximated by weighted sums of periodic orbits. One evidence for this

picture was presented in the pioneering work by Kawahara & Kida (2001) who showed the existence of time periodic solutions which give a surprisingly good approximation of turbulent trajectories and must have a large weight in the periodic orbit expansion. In addition, van Veen & Kawahara (2011) found orbits homoclinic to edge states which resemble to turbulent burst events. Such orbits have an infinite period, as they lie in the intersection of unstable and stable manifolds of the edge state. Importantly these homoclinic orbit solutions predict the presence of Smale's horseshoe which could explain chaotic dynamics of turbulence.

However, though these investigations for three-dimensional instability provide fairly comprehensive mechanisms of the transition dynamics, it should be noted that all such studies are undertaken far away from a parameter value region that yields linear and nonlinear two-dimensional instabilities. Therefore, this type of instability could 'pass the torch' to a Tollmien-Schlichting type disturbance as the critical Reynolds number for linear stability is approached. Consequently, two-dimensional finite-amplitude solutions bifurcating from the linear neutral point could play a crucial role when we consider laminar-turbulent transition control at high R. Thus the study of both two- and three-dimensional solutions are indispensable to understanding shear flow transition.

1.3 Nonlinear asymptotic theory of shear flows

One of the aims of present thesis is to attempt to describe the structure of the nonlinear travelling wave solutions using high Reynolds number asymptotic theory. There are two- and three-dimensional theories corresponding to two types of vortical structure described above.

This comparison of full Navier-Stokes finite amplitude solutions and asymptotic analysis is motivated in part by the work of Hall & Sherwin (2010), who recently successfully linked the asymptotic behaviour of the three-dimensional solutions described above to the high Reynolds number vortex-wave interaction (VWI) theory developed by Hall & Smith (1991).

The main point of this theory is that the wave described in the SSP satisfies the inviscid linearized Navier-Stokes equation in the limit as $R \to \infty$ exhibiting discontinuity at the critical layer. As a consequence, the forcing to the rolls emerges as a result of the effect of viscosity which smooths out the singularity. This forcing triggers interaction of the wave, roll and streaks as SSP.

It is known that both Waleffe's SSP and the VWI theory approaches describe the mechanism of the lower-branch exact coherent states predicting $O(R^{-1})$ streamwise rolls compared to the basic flow. Wang, Gibson & Waleffe (2007) confirmed that the lower-branch of the three-dimensional solution of PCF, first discovered by Nagata (1990), obeys this $O(R^{-1})$ scaling for a wide range of values of R. Therefore this lower-branch scaling is considered to represent threshold roll amplitude scaling of transition, when we recall the dynamical systems point of view described in the last section. Indeed, the same scaling has also been observed experimentally in a flow through a pipe (Darbyshire & Mullin 1995 and Hof *et al.* 2004) and a channel (Lemoult *et al.* 2012). They confirm that for moderate R, the $O(R^{-1})$ roll disturbances induced can destabilize the basic flow by the so-called lift-up mechanism, and ultimately generates the SSP.

Note that because of key differences in the explanations of how the wave is excited, only VWI theory is available to explain the asymptotic flow structure of high R finite-amplitude solutions qualitatively whereas only SSP elucidates how three-dimensional coherent structures evolve from small roll disturbances as above.

Wang *et al.* (2007) also discovered that the sinuous waves excite forcing in the vicinity of the critical layer, as explained by the VWI theory. This work inspired the study of Hall & Sherwin (2010) which refined the VWI theory deducing a closed system for infinite Reynolds number shear flows. They solved this "VWI system" for PCF numerically, and showed that the extrapolation of this solution from $R = \infty$ agrees with Wang *et al.*'s calculations. We will confirm these VWI asymptotic structures for numerical solutions in section 6.3.

In contrast to the VWI theory, where the flow must be necessarily three-dimensional, the

asymptotic theory we outline here in section 4.2 is derived under the assumption of two-dimensionality, so that the disturbances resemble Tollmien-Schlichting waves, i.e. they are invariant under any translation in one specific direction. The dominant physical balances are similar to those proposed in studies by Benney & Bergeron (1969) and Davis (1969), and the properties of such critical layers were investigated further by Haberman (1972), Brown & Stewartson (1978), Smith & Bodonyi (1982a,b) and Bodonyi, Smith & Gajjar (1983).

The asymptotic theory derived in these studies also involves the presence of a strongly nonlinear equilibrium critical layer as VWI theory. However, the asymptotic structure is directly sustained by the jump in vorticity across the layer, which acts as a forcing of the mean-flow distortion in the bulk of the flow outside the critical layer. Although the properties of these critical layers and the associated surrounding flow have been known for some time, the delicate structure of the overall solution, with its asymptotically thin internal and boundary layers, has proved difficult to detect in full Navier-Stokes computations thus far. In section 4.2, we are able, for the first time, to quantitatively compare the flow structures present in full Navier-Stokes finite-amplitude solutions with those resulting from an asymptotic analysis.

1.4 Sliding Couette flow

In this thesis, the specific flow we consider is the one where the fluid motion is produced by the mutual axial sliding motion of co-axial cylinders of circular cross-section, and the fluid occupies the annular region between the cylinders (see figure 2.1in the next chapter). We refer to this flow as sliding Couette flow (SCF), following the flow classification by Joseph (1976).

SCF is one of the simplest models to examine the effect of spanwise curvature on shear flows. The shear-spanwise curvature instability is relevant to many industrial and medical applications: pipelinings (Arney *et al.* 1993), wire coating (Tadmor & Bird 1974), the

production of optical fibres during the draw process (Chida *et al.* 1982, Panoliaskos *et al.* 1985 and Vaskopulos *et al.* 1993) and medical treatment by a thread injection (Frei *et al.* 2000; Walton 2003, 2004, 2005). These situations are effectively modelled when SCF is extended to annular Couette-Poiseuille flow, where the fluid motion is produced both by the streamwise pressure gradient and the axial motion of the cylinders.

In addition, the zero pressure gradient case has some relevance to the boundary-layer flow along a cylinder (e.g. Tutty 2008 and Cipolla & Keith 2003): see section 6 of Gittler (1993). Therefore applications of pure SCF, especially for its wide gap case results, can be found in various aeronautical and astronautical situations while one of the applicable situations for relatively narrow-gap SCF is flows around a train moving through a tunnel.

Despite these important applications, SCF has attracted much less attention than other shear flows. Hitherto, theoretical studies of SCF has extended only to linear results. The linear stability of SCF was first studied by Preziosi & Rosso (1990) who did not find any indication of instability within the parameter range they considered. However, Gittler (1993), restricting his analysis to axisymmetric perturbations, detected instability for radius ratio less than 0.1415 at much larger values of the Reynolds number than those considered by Preziosi & Rosso (1990). Although nonlinear asymptotic theory (Walton 2003, 2004 and 2005) and axisymmetric finite-amplitude solutions (Wong & Walton 2012) have already been developed for annular Couette-Poiseuille flow, corresponding nonlinear results have yet to be found for SCF. Experimental results for annular flow with a sliding inner core can only found in Shands *et al.* (1980) and Frei *et al.* (2000).

Another special property of SCF is that we recover PCF from this problem in the narrow-gap limit, while PF can also be obtained in the limit as the radius of the inner cylinder vanishes with a proper axial pressure gradient. PCF, the simplest shear flow, and PF, whose applications can be found everywhere in our daily lives are particularly important shear flows, and much research attention has been devoted to these problems as a consequence. We will discuss some homotopy connections between the finite-amplitude solutions of these flows in chapters 5 and 6.

The rest of the thesis is organized as follows: We formulate the problem in chapter 2, followed by the linear stability analysis with respect to an arbitrary three-dimensional perturbation in chapter 3. In this chapter we confirm the result by Gittler (1993) that SCF is linearly stable against axisymmetric perturbations for $\eta \leq 0.1415$. In addition, we find that the critical state is determined by axisymmetric perturbations. Axisymmetric finite-amplitude solutions that bifurcate from the linear critical state for $\eta \leq 0.1415$ are obtained in our nonlinear analysis in chapter 4. These solutions exist at relatively high Reynolds numbers. We also present in this chapter, the corresponding axisymmetric high Reynolds number asymptotic theory and the results thus obtained are compared to numerical solutions quantitatively. In chapter 5 we explore the possibility that other types of finite-amplitude solutions exist at lower Reynolds numbers. Using the fact that SCF approaches PCF in the narrow-gap limit we continue the three-dimensional finite-amplitude solutions of PCF (Nagata 1990) to wider gap cases. As a result a family of finite-amplitude non-axisymmetric solutions is found at relatively low Reynolds numbers. We further identify a second class of non-axisymmetric solutions that bifurcate from the first class of solutions. In contrast to the latter solutions, this second class of solutions has a mirror symmetric flow structure. In chapter 6 we describe how these bifurcating solutions are continued to PCF and PF by gradually changing flow configuration. The associated complex bifurcation scenario is examined in detail, while their flow structure is examined by applying VWI theory. Finally, in chapter 7, we summarize our findings and draw some conclusions.

Chapter 2

Formulation of the problem

2.1 The governing equations and the basic state

We consider an incompressible viscous fluid with kinematic viscosity ν and density ρ between two infinitely long concentric cylinders with radii a and b ($b > a$). The fluid experiences a shear motion when the inner cylinder is pulled with the axial speed U_s while the outer cylinder is kept at rest. The flow defines sliding Couette flow (SCF) when the axial pressure gradient is set to zero. We adopt a cylindrical coordinate system (x, r, θ) as shown in figure 2.1. To nondimensionalise the problem we use $(b-a)/2$, $(b-a)^2/4\nu$ and $4\rho\nu^2/(b-a)^2$ as the length, time and pressure scales, respectively. These length and time scales reduce the velocity scale to $2\nu/(b-a)$, which is consistent with the one chosen by Nagata (1990) for PCF (c.f. chapter 5). This choice of the velocity scale is also useful when one considers an extension to the Couette-Poiseuille flow problem, which is controlled by two independent velocities (c.f. chapter 6). With the present length scale, inner, outer and mean radius can be written as a function of the radius ratio $\eta = a/b$ as $r_a = 2\eta/(1-\eta)$, $r_b = 2/(1-\eta)$ and $r_m = (1+\eta)/(1-\eta)$, respectively. The nondimensional total velocity $\mathbf{U} = U\mathbf{e}_x + V\mathbf{e}_r + W\mathbf{e}_\theta$, where $\mathbf{e}_x$, $\mathbf{e}_r$ and $\mathbf{e}_\theta$ are the unit vectors in the axial, radial, and azimuthal directions, and pressure P are governed by dimensionless

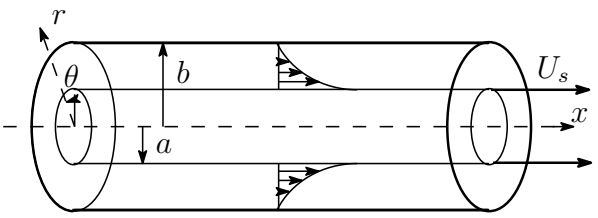

Figure 2.1: The configuration of sliding Couette flow.

Navier-Stokes equations

$$\nabla \cdot \mathbf{U} = 0, \tag{2.1}$$

$$\frac{\partial \mathbf{U}}{\partial t} + (\mathbf{U} \cdot \nabla)\mathbf{U} = -\nabla P + \nabla^2 \mathbf{U}, \tag{2.2}$$

subject to the no-slip boundary condition on the inner and outer cylinders at $r = r_a$ and $r = r_b$, respectively:

$$\mathbf{U} = R\mathbf{e}_x \qquad \text{at} \qquad r = r_a = 2\eta/(1-\eta), \tag{2.3}$$

$$\mathbf{U} = \mathbf{0} \qquad \text{at} \qquad r = r_b = 2/(1-\eta) \tag{2.4}$$

where $R = U(b-a)/2\nu$ is the Reynolds number. In equations (2.1) and (2.2), the standard notation for the gradient operator, ∇, is used. This system is equivalent under axial and azimuthal translations and azimuthal reflection.

The axial basic flow $\mathbf{U}_B$ depending on only r,

$$\mathbf{U}_B(r) = U_B(r)\mathbf{e}_x = R\frac{\ln(r/r_b)}{\ln \eta}\mathbf{e}_x, \tag{2.5}$$

can be solved as an exact solution of linearized governing equations $0 = \partial_{rr}^2 U_B + r^{-1}\partial_r U_B$ subject to boundary conditions (2.3) and (2.4). Note that the zero pressure gradient constraint leads basic pressure $P_B(r)$ =const.

2.2 The disturbance equations written in terms of potentials

We assume that the flow is periodic in the azimuthal and axial directions with the wavenumbers m_0 and α, respectively. This assumptions allows us to use potential notation which is convenient to reduce computational costs (Marques 1990). The disturbance velocity $\mathbf{u}$ to the basic flow is decomposed into a spatially varying fluctuation part $\tilde{\mathbf{u}} = \tilde{u}\mathbf{e}_x + \tilde{v}\mathbf{e}_r + \tilde{w}\mathbf{e}_\theta$ and a spatial mean part $\overline{\mathbf{u}} = \overline{u}\mathbf{e}_x + \overline{v}\mathbf{e}_r + \overline{w}\mathbf{e}_\theta$. The latter is defined by the (θ, x)-average:

$$\bar{\cdot} = \frac{m_0\alpha}{4\pi^2}\int_0^{\frac{2\pi}{m_0}}\int_0^{\frac{2\pi}{\alpha}} \cdot \, d\theta dx. \tag{2.6}$$

Notice that radial mean flow $\overline{v}$ vanishes by the incompressibility condition (2.1) with the boundary conditions (2.3) and (2.4). The fluctuation part $\tilde{\mathbf{u}}$ is further decomposed into a poloidal part, $\nabla\times\nabla\times(\phi\mathbf{e}_r)$, and a toroidal part, $\nabla\times(\psi\mathbf{e}_r)$, so that the total velocity field $\mathbf{U}$ is expressed as

$$\begin{aligned}\mathbf{U} &= (U_B+\overline{u})\mathbf{e}_x + \overline{w}\mathbf{e}_\theta + \nabla\times\nabla\times(\phi\mathbf{e}_r) + \nabla\times(\psi\mathbf{e}_r) \\ &= \begin{bmatrix} U_B + \overline{u} + \frac{1}{r}\partial_{rz}^2 r\phi - \frac{1}{r}\partial_\theta\psi \\ -(\frac{1}{r^2}\partial_{\theta\theta}^2 + \partial_{zz}^2)\phi \\ \overline{w} + \partial_{r\theta}^2\frac{\phi}{r} + \partial_z\psi \end{bmatrix}.\end{aligned} \tag{2.7}$$

Note that this expression ensures the incompressibility condition (2.1) is satisfied. The equations for ϕ and ψ are obtained by operating $\mathbf{e}_r\cdot\nabla\times\nabla\times$ and $\mathbf{e}_r\cdot\nabla\times$, respectively, on the momentum equation (2.2):

$$\begin{aligned}&r(\partial_t - \grave{\triangle})(\grave{\triangle}\triangle_2\frac{\phi}{r} + \frac{2}{r^3}\partial_r\frac{\phi_{\theta\theta}}{r}) - \frac{2}{r^2}(\partial_r\triangle\frac{\phi_{\theta\theta}}{r} - \frac{2}{r^2}\phi_{\theta\theta xx}) + \frac{2}{r}(\partial_t - 2\triangle)\frac{\psi_{\theta x}}{r} \\ &+ \overline{\mathbf{U}}\cdot\nabla_c(r\triangle_2\triangle\frac{\phi}{r} + 2\partial_r\frac{\phi_{xx}}{r} + \frac{2}{r^2}\psi_{\theta x}) + \overline{\mathbf{U}}'\cdot\nabla_c\triangle_2\frac{\phi}{r} - r\overline{\mathbf{U}}''\cdot\nabla_c\triangle_2\frac{\phi}{r} \\ &- \frac{2}{r^2}\overline{W}'\triangle_2\phi_\theta - \frac{3}{r^3}\overline{W}\phi_{\theta xx} + \frac{1}{r^5}\overline{W}\phi_{\theta\theta\theta} + \frac{2}{r}\overline{W}\triangle_2\psi_x \\ &+ \mathbf{e}_r\cdot\nabla\times\nabla\times(\tilde{\mathbf{u}}\cdot\nabla_c\tilde{\mathbf{u}} + \frac{\tilde{v}}{r}\mathbf{e}_z\times\tilde{\mathbf{u}}) = 0,\end{aligned} \tag{2.8}$$

and

$$
\begin{aligned}
&-r(\partial_t - \grave{\triangle})\triangle_2\frac{\psi}{r} + \frac{2}{r^2}\partial_r\frac{\psi_{\theta\theta}}{r} + \frac{2}{r}(\partial_t - 2\triangle)\frac{\phi_{\theta x}}{r} \\
&+ ((r\overline{W})'\partial_x - \overline{U}'\partial_\theta)\triangle_2\frac{\phi}{r} + \overline{\mathbf{U}}\cdot\nabla_c(\frac{2}{r^2}\phi_{\theta x} - \triangle_2\psi) \\
&+ \mathbf{e}_r\cdot\nabla\times(\tilde{\mathbf{u}}\cdot\nabla_c\tilde{\mathbf{u}} + \frac{\tilde{w}}{r}\mathbf{e}_x\times\tilde{\mathbf{u}}) = 0,
\end{aligned}
\tag{2.9}
$$

where the prime, $'$, denotes differentiation with respect to r and

$$
\begin{aligned}
\triangle_2 &= \frac{1}{r^2}\partial^2_{\theta\theta} + \partial^2_{xx}, \\
\triangle &= \partial^2_{rr} + \frac{1}{r}\partial_r + \frac{1}{r^2}\partial^2_{\theta\theta} + \partial^2_{xx}, \\
\grave{\triangle} &= \partial^2_{rr} + \frac{3}{r}\partial_r + \frac{1}{r^2}\partial^2_{\theta\theta} + \partial^2_{xx}, \\
\nabla_c &= \mathbf{e}_r\partial_r + \mathbf{e}_\theta\frac{1}{r}\partial_\theta + \mathbf{e}_x\partial_x.
\end{aligned}
$$

In order to obtain equations for $\overline{U}$ and $\overline{W}$ we take the (θ, x)-average of the azimuthal and axial components, respectively, of equation (2.2):

$$
\partial_t\overline{u} = r^{-1}\partial_r\{r\overline{(\triangle_2\phi)(r^{-1}\partial_r r\partial_x\phi - r^{-1}\partial_\theta\psi)} + r\overline{u}'\},
\tag{2.10}
$$

$$
\partial_t\overline{w} = r^{-2}\partial_r\{r^2\overline{(\triangle_2\phi)(\partial_\theta\partial_r r^{-1}\phi + \partial_x\psi)} + (r^2\overline{w}' - r\overline{w})\}.
\tag{2.11}
$$

The no-slip boundary conditions become

$$
\overline{u} = \overline{w} = \phi = \partial_r\phi = \psi = 0 \qquad \text{at} \qquad r = r_a \text{ and } r_b.
\tag{2.12}
$$

2.3 Numerical method to solve finite-amplitude solutions

In this section we describe how to compute solutions of equations (2.8)–(2.11) that take the form of travelling waves, propagating with the axial wavespeed c and the azimuthal wavespeed c_θ. The scalar variables ϕ, ψ, $\overline{u}$ and $\overline{w}$ therefore become functions of the radial coordinate r and the travelling-wave coordinates

$$\xi = \alpha(x - ct) \in [0, 2\pi], \tag{2.13}$$

$$\zeta = m_0(\theta - c_\theta t) \in [0, 2\pi]. \tag{2.14}$$

These variables are approximated by the truncated sums

$$\phi(\xi, y, \zeta) = \sum_{\substack{m=-M \\ (m,n)\neq(0,0)}}^{M} \sum_{n=-N}^{N} \sum_{l=0}^{L} X^{(1)}_{lmn} \Phi_l(y) e^{\mathrm{i}(m\zeta + n\xi)}, \tag{2.15}$$

$$\psi(\xi, y, \zeta) = \sum_{\substack{m=-M \\ (m,n)\neq(0,0)}}^{M} \sum_{n=-N}^{N} \sum_{l=0}^{L} X^{(2)}_{lmn} \Psi_l(y) e^{\mathrm{i}(m\zeta + n\xi)}, \tag{2.16}$$

$$\overline{u}(y) = \sum_{l=0}^{L} X^{(1)}_{l00} U_l(y), \tag{2.17}$$

$$\overline{w}(y) = \sum_{l=0}^{L} X^{(2)}_{l00} W_l(y), \tag{2.18}$$

where $\Phi_l = (1 - y^2)^2 T_l(y)$ and $\Psi_l = U_l = W_l = (1 - y^2) T_l(y)$ are modified lth-order Chebyshev polynomials of the first kind $T_l(y)$ in the transformed radial coordinate

$$y = r - r_m \in [-1, 1]. \tag{2.19}$$

The factors $(1 - y^2)$ and $(1 - y^2)^2$ in the basis are introduced in order for the boundary condition (2.12) to be satisfied. Throughout the present thesis, the radial, azimuthal and axial truncation levels are denoted by L, M and N respectively.

To restrict the flow field to be real, all the $X^{(j)}_{lmn}$ should have Hermitian redundancy, i.e.

$$\Re(X^{(j)}_{lmn}) = \Re(X^{(j)}_{l-m-n}),$$
$$\Im(X^{(j)}_{lmn}) = -\Im(X^{(j)}_{l-m-n}).$$

After Galerkin projection in the two periodic directions, equations (2.8)–(2.11) are evaluated at collocation points

$$y_l = \cos\left(\frac{l+1}{L+2}\pi\right), \qquad l = 0, ..., L. \tag{2.20}$$

We then obtain the nonlinear algebraic equations

$$F_i = D_{ij}X_j + H_{ijk}X_jX_k + \mathrm{i}(mm_0c_\theta + n\alpha c_z)B_{ij}X_j = 0. \tag{2.21}$$

In these equations, unknowns are $X_i \in X^{(j)}_{lmn}$ and the wavespeeds c and c_θ. The involvement of these additional variables for the solution requires that some conditions which fix the translation freedom of the solution in the ξ and ζ directions. The detailed conditions for two- and three-dimensional solutions will be shown in sections 4.1 and 5.1 respectively.

Equation (2.21) is solved by the Newton-Raphson iterative scheme with the tolerance

$$\epsilon = \max_j \epsilon_j < 10^{-5} \tag{2.22}$$

where

$$\epsilon_j = \begin{cases} \left|\frac{X_j^{I_t} - X_j^{I_t-1}}{X_j^{I_t-1}}\right| & \text{if} \quad |X_j^{I_t-1}| \ \text{ and } \ |X_j^{I_t}| > 10^{-10} \\ 0 & \text{otherwise} \end{cases} \tag{2.23}$$

and I_t is the iteration number. The choice of 10^{-5} in condition (2.22) is justified in Appendix 5.A.1.

The momentum transfer on the outer cylinder at $r = r_b$, normalized by that of the base

flow,

$$\Delta \equiv \left. \frac{\overline{u}' + U_B'}{U_B'} \right|_{r=r_b} \tag{2.24}$$

is used as a measure of how much a nonlinear solution differs from the basic flow. Note that we can confirm that $r_a \overline{u}'|_{r=r_a} = r_b \overline{u}'|_{r=r_b}$ by multiplying equation (2.10) by r and integrating with respect to r. Since the basic flow of SCF (2.5) satisfies $r_a U_B'|_{r=r_a} = r_b U_B'|_{r=r_b}$, the momentum transfer on the inner cylinder at $r = r_a$, given by $\left. \frac{\overline{u}' + U_B'}{U_B'} \right|_{r=r_a}$, is exactly equal to the right hand side of (2.24). Note however that the numerical values of momentum transfer differ slightly due to the finite truncation of the basis functions. This difference can be made to be insignificant if large enough truncation levels are used.

Chapter 3

The linear stability of the basic state

3.1 Numerical method

When the deviations from the basic state are infinitesimal the Reynolds stresses in (2.11) and (2.10) can be omitted to result in $\overline{u} = \overline{w} = 0$, i.e. $\overline{\mathbf{U}} = U_B \mathbf{e}_x$. Neglecting those terms that are quadratic in $\tilde{\mathbf{u}}$ in (2.9) and (2.8) we obtain the linearized disturbance equations,

$$r(\partial_t - \grave{\triangle})(\grave{\triangle}\triangle_2 \frac{\check{\phi}}{r} + \frac{2}{r^3}\partial_r \frac{\check{\phi}_{\theta\theta}}{r}) - \frac{2}{r^2}(\partial_r \triangle \frac{\check{\phi}_{\theta\theta}}{r} - \frac{2}{r^2}\check{\phi}_{\theta\theta xx}) + \frac{2}{r}(\partial_t - 2\triangle)\frac{\check{\psi}_{\theta x}}{r}$$
$$+ U_B \partial_x (r\triangle_2 \triangle \frac{\check{\phi}}{r} + 2\partial_r \frac{\check{\phi}_{xx}}{r} + \frac{2}{r^2}\check{\psi}_{\theta x}) + U_B' \partial_x \triangle_2 \frac{\check{\phi}}{r} - rU_B'' \partial_x \triangle_2 \frac{\check{\phi}}{r} = 0 \qquad (3.1)$$

and

$$-r(\partial_t - \grave{\triangle})\triangle_2 \frac{\check{\psi}}{r} + \frac{2}{r^2}\partial_r \frac{\check{\psi}_{\theta\theta}}{r} + \frac{2}{r}(\partial_t - 2\triangle)\frac{\check{\phi}_{\theta x}}{r}$$
$$- U_B' \partial_\theta \triangle_2 \frac{\check{\phi}}{r} + U_B \partial_x (\frac{2}{r^2}\check{\phi}_{\theta x} - \triangle_2 \check{\psi}) = 0 \qquad (3.2)$$

where we write $\tilde{\mathbf{u}} = \nabla \times \nabla \times (\check{\phi}\mathbf{e}_r) + \nabla \times (\check{\psi}\mathbf{e}_r)$. Note that the solution can be taken to be proportional to normal modes because equations are now linear. Thus the potentials $\check{\phi}$

and $\check{\psi}$ are approximated by

$$\check{\phi}(x,y,\theta,t) = \sum_{l=0}^{L} \check{X}_l^{(1)} \Phi_l(y) \exp\left(\mathrm{i}\alpha x + \mathrm{i}m_0\theta + st\right), \tag{3.3}$$

$$\check{\psi}(x,y,\theta,t) = \sum_{l=0}^{L} \check{X}_l^{(2)} \Psi_l(y) \exp\left(\mathrm{i}\alpha x + \mathrm{i}m_0\theta + st\right), \tag{3.4}$$

where $s = \sigma + \mathrm{i}\gamma$ is the (complex-valued) growth rate. The ansatz used in expressions (3.3) and (3.4) allows us to apply the separation of variables and reduce the resulting equations to a system that depends only on y. We substitute expansions (3.3) and (3.4) into the linearized disturbance equations (3.1) and (3.2), which are then evaluated at the collocation points defined by (2.20). The resulting linear algebraic eigenvalue problem with the growth rate s as the eigenvalue,

$$D_{ij}\check{X}_j = sB_{ij}\check{X}_j, \tag{3.5}$$

is solved numerically by using the LAPACK package ZGGEVX. The matrices D_{ij} and B_{ij} depend on η, R, m_0 and α, and so $s = s(\eta, R, m_0, \alpha)$. The azimuthal reflection symmetry of SCF allows the restriction to $m_0 \in \mathbb{Z}_{\geq 0}$ and $\alpha \in [0, \infty)$.

3.2 Results

Table 3.1 shows typical eigenvalues calculated at different truncation levels L. From the table we find $L = 120$ is sufficient when $R = 3.6 \times 10^6$ and $m_0 = 0$ (it will be shown later that this R is close to the critical value) whereas $L = 600$ is needed if the Reynolds number is ten times higher than the critical value and $m_0 \neq 0$. For a given η the stability of the basic state at R subject to a perturbation with m_0 is determined by the largest real part of σ of the growth rate s over all possible values of α, which we denote by σ_α. For $m_0 = 0$ and 1, we plot σ_α on the (η, R) plane in figure 3.1, where the truncation level $L = 600$ is used. As shown in the figure 3.1 (a) for axisymmetric perturbations ($m_0 = 0$) two eigenmodes are shown in the contour plot of σ_α in the (η, R) plane: one always has negative σ_α while the

flow is unstable to the other mode anywhere inside the locus of $\sigma_\alpha = 0$ (thick solid curve). For the non-axisymmetric perturbation ($m_0 = 1$), σ_α is always negative as shown in figure 3.1 (b). Other computations show that σ_α is always strictly negative for $m_0 = 2, 3, 4$. We, therefore, conclude that the flow is linearly stable to all non-axisymmetric perturbations. The locus of $\sigma_\alpha = 0$ in figure 3.1 (a) is reproduced in figure 3.2 (a) as the neutral curve. We can see from figure 3.2 (a) that as η is decreased from the narrow gap limit ($\eta = 1$) the neutral curve emerges from infinity at $\eta \approx 0.14$, drops sharply reaching a minimum at $\eta \approx 0.1$ and ascends sharply toward infinity as η approaches zero. Along the neutral curve, the critical axial wavenumber α_c decreases monotonically to zero as η approaches to the cut-off value as shown in figure 3.2 (b). When $\eta = 0.1$, $R_c = 3.61 \times 10^6$ at $\alpha_c = 0.6546$. This result is consistent with the findings of Gittler (1993), who restricted his linear stability analysis only to axisymmetric perturbations. According to his result, more precise cut-off value of η can be obtained as 0.1415 by solving a long-wave linear stability problem.

It can be shown that any infinitesimal axisymmetric perturbations, $[v, w] = [\breve{v}(r), \breve{w}(r)]e^{\mathrm{i}\alpha x + st}$, to the inviscid annular flow are governed by

$$(s + \mathrm{i}\alpha U_B)\breve{w}' = 0, \tag{3.6}$$

$$(s + \mathrm{i}\alpha U_B)(\breve{v}'' + r^{-1}\breve{v}' - (r^{-2} + \alpha^2)\breve{v}) - \mathrm{i}\alpha U_B(U_B'' - r^{-1}U_B')\breve{v} = 0 \tag{3.7}$$

subject to $\breve{v} = \breve{w} = 0$ at the walls. The former equation only has trivial solutions while later equation yields

$$\sigma \int_{r_a}^{r_b} \frac{(r^{-1}U_B')' r^2 |\breve{v}'|^2}{|U_B + \gamma|^2} dr = 0, \qquad s = \sigma + \mathrm{i}\gamma. \tag{3.8}$$

This leads to Rayleigh's inflection point theorem for the planar geometry extended to the annular geometry (Problem 3.2 in Drazin & Reid 1981, Walton 2004), i.e. $(r^{-1}U_B')' = 0$, which never occur with the basic flow given by (2.5), must be satisfied for some $r \in [r_a, r_b]$ in order to yield a growing disturbance ($\sigma > 0$). Therefore, the fact that SCF for $\eta < 0.1415$ becomes unstable implies that viscosity is necessary for linear instability.

(η, m_0, α, R)	L	$\Re(s) = \sigma$	$\Im(s) = \gamma$
$(0.1, 0, 0.6546, 3.6 \times 10^6)$	120	-7.25876×10^0	-2.26731×10^6
$(0.1, 0, 0.6546, 3.6 \times 10^6)$	130	-7.28065×10^0	-2.26731×10^6
$(0.1, 0, 0.6546, 3.6 \times 10^6)$	140	-7.28189×10^0	-2.26731×10^6
$(0.01, 1, 2.0, 4.0 \times 10^7)$	120	1.99913×10^5	-6.50952×10^7
$(0.01, 1, 2.0, 4.0 \times 10^7)$	550	-4.69859×10^4	-1.72860×10^5
$(0.01, 1, 2.0, 4.0 \times 10^7)$	600	-4.69859×10^4	-1.72860×10^5

Table 3.1: The eigenvalue s determined by the linear stability analysis.

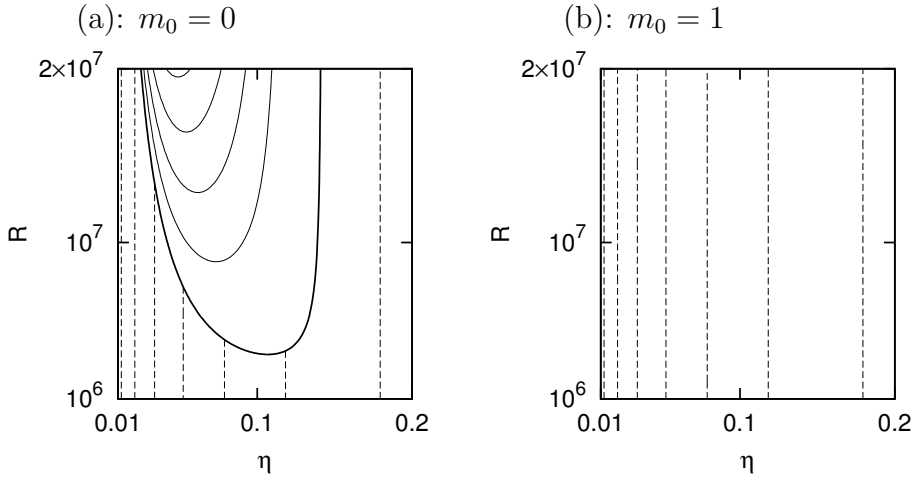

Figure 3.1: Contour plot of the largest real part σ_α of the eigenvalue s as a function of η and R. (a): dashed lines correspond to -8.2, -8.4, -8.5, -8.6, -8.8, -9.0, -9.2 (from left to right), the thick solid curve corresponds to 0 and thin solid curves correspond to 4000, 8000, 12000, 16000 (from bottom to top). (b): dashed lines correspond to -8.2, -8.4, -8.5, -8.6, -8.8, -9.0, -9.2 (from left to right).

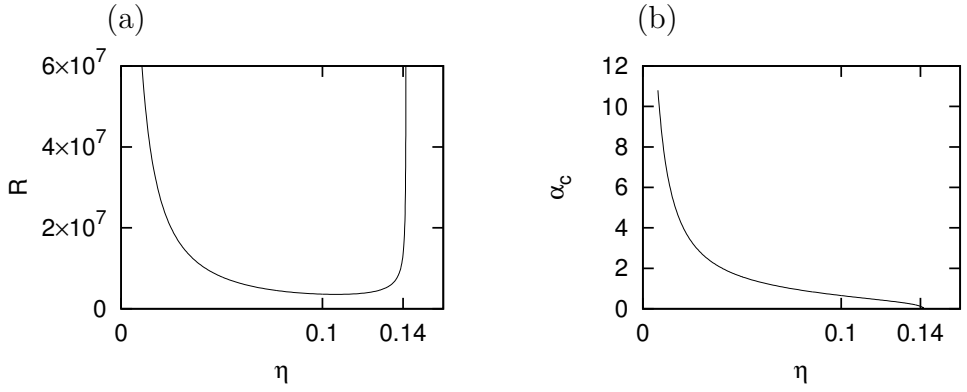

Figure 3.2: The neutral curve determined by axisymmetric perturbations ($m_0 = 0$). (a): the critical Reynolds number R_c. (b): the critical axial wavenumber α_c.

Chapter 4

Axisymmetric solutions

4.1 Bifurcation from the linear neutral curve

If $\eta \lesssim 0.1415$, where the long-wave cut-off of linear instability occurs, the basic flow can be destabilized by axisymmetric infinitesimal disturbances as we saw in the previous chapter. Since the linear approximation of the growing mode is accurate close to the neutral stability point, it can be used as an initial guess for a nonlinear calculation using Newton's method. As a consequence, the solution branch of the finite-amplitude axisymmetric travelling wave that bifurcates from this point can be computed. The spatial phase lock condition which we impose for two-dimensional solutions is

$$F(0) - \text{c.c.} = 0$$

where the first Fourier coefficient of axial velocity is defined as

$$F(y) \equiv 2\overline{ue^{-\mathrm{i}\xi}} \tag{4.1}$$

and c.c. denotes complex conjugate. This ensures that the $\sin\xi$ component of u vanishes at the midpoint of the gap. This property is useful when we compare numerical solutions with those obtained by asymptotic analysis (section 4.2).

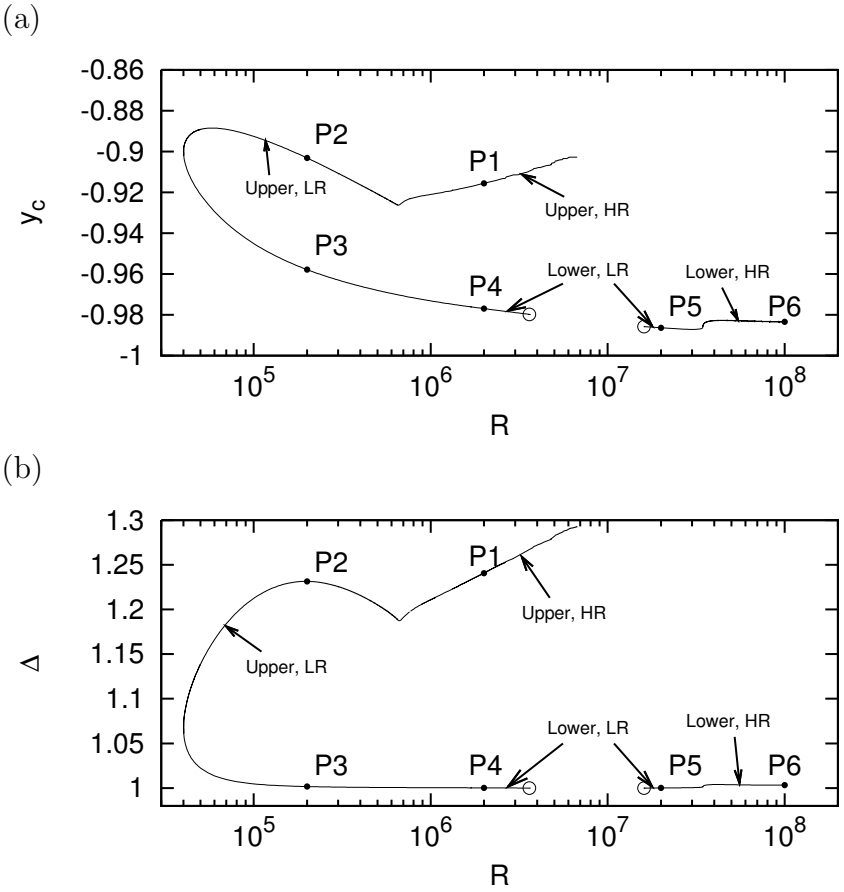

Figure 4.1: The axisymmetric travelling-wave bifurcation diagram for $(\eta, \alpha) = (0.1, 0.6546)$. The upper and lower figures represent the variation of the critical layer location y_c and the momentum transfer Δ respectively. Open circles in the figures represent linear critical points. The range of truncation level $L \in [120, 200]$ and $N \in [30, 60]$ is used to compute the solution branches.

	Upper				Lower			
(L, N)	Δ	c/R	$\|L_i\|_2$	$\|F_i\|_2$	Δ	c/R	$\|L_i\|_2$	$\|F_i\|_2$
(120,20)	1.11730	0.82654	6.8e9	2.5e-3	1.03183	0.85887	5.1e9	9.6e-4
(180,20)	1.11730	0.82654	8.6e9	7.1e-4	1.03183	0.85890	5.5e9	5.3e-4
(120,30)	1.11727	0.82650	8.5e9	3.6e-4	1.03174	0.85887	6.4e9	1.6e-3

Table 4.1: The momentum transfer Δ, the wavespeed c and the L_2-norms $\|L_i\|_2$ and $\|F_i\|_2$ at different truncation levels (L, N) for the axisymmetric solution at $(\eta, \alpha, R) = (0.1, 0.6546, 45000)$.

In section 3.2 the linear critical point for $\eta = 0.1$ was determined to be $(m0, \alpha, R) = (0, 0.6546, 3.6 \times 10^6)$. Firstly, we set $\eta = 0.1$, $m_0 = 0$ and $\alpha = 0.6546$ and it is found that the bifurcation is subcritical with a saddle-node at $R \approx 4.0 \times 10^4$ as shown in figure 4.1.

Table 4.1 shows the variation of various measures (Δ: the momentum transfer, c: the axial wavespeed and the L_2-norms of the linear part $L_i = D_{ij}X_j$ of equation (2.21), $\|L_i\|_2$, and the residual of equation (2.21), $\|F_i\|_2$) as a function of the truncation level (L, N) for a typical axisymmetric solution. We see the truncation level $(L, N) = (120, 20)$ is sufficient for approximating the axisymmetric solutions. However, we need to increase the truncation level as the value of R increases. For these cases, we performed a similar check of convergence.

At the same wavenumber $\alpha = 0.6546$, the basic flow restabilizes at $R = 1.6 \times 10^7$. From this second neutral point, another bifurcation of the axisymmetric solution is detected. This bifurcation scenario is also pictured in figure 4.1, and it can be seen in the figure that the resultant branch heads in the direction of increasing R, in which the basic flow becomes linearly stable; i.e. the new bifurcation is also subcritical. We adopt the terminology 'lower-branch' to represent the branch that passes through the neutral points, and the points such as passing through P3–P6 while the phrase 'upper-branch' is used to denote solutions at higher Δ, that lie on the solution curve that passes through P1 and P2. One of the striking features of this branch is the kink at $R \simeq 3.5 \times 10^7$, and a similar kink can also be found on the upper-branch in between the points P2 and P1, at $R \simeq 6.7 \times 10^5$. The branches behave differently before and after the kinks, although no bifurcations take place here, and the curves appear smooth when examined closely. Henceforth we denote the branches before and after the kinks as the LR (low Reynolds number) and HR (high Reynolds number) modes respectively.

Along the branches, the streamwise fluctuation flow-field, $\tilde{u}$, is visualized in figures 4.2 and 4.3. The plots labelled by P1–P6 represent solutions at the corresponding points in figure 4.1. For the upper-branch solution at sufficiently high Reynolds number (P1, P2), we can see a relatively slowly-varying, evenly-spaced strong positive/negative pattern in

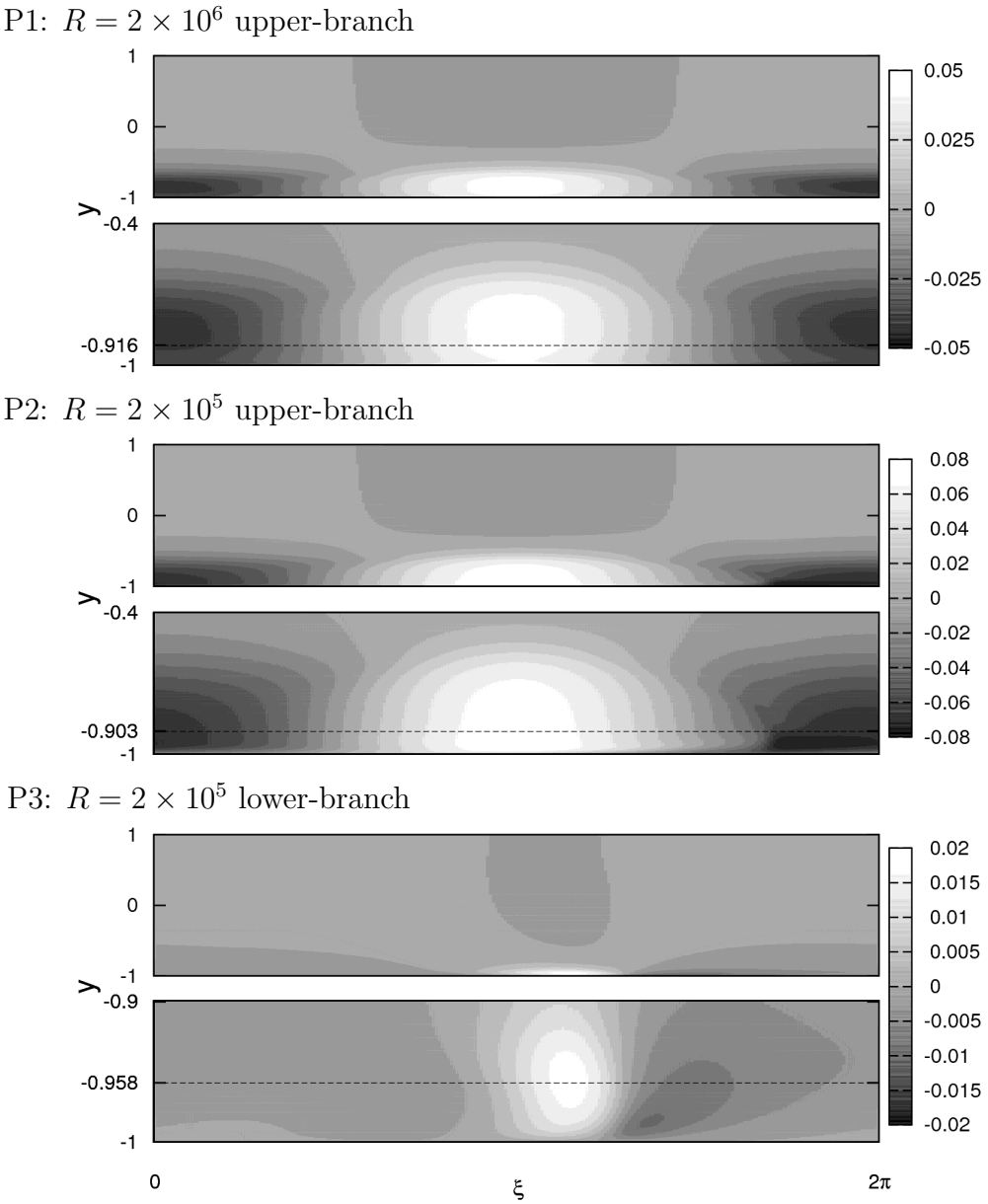

Figure 4.2: The axial fluctuation velocity field $\tilde{u}$ of the travelling-wave solutions for $(\eta, \alpha) = (0.1, 0.6546)$. Colour bar range is scaled by R. The dashed lines in the close-up figures, which are placed just below the full domain representation in each case, represent the critical layer locations y_c. P1, P2 and P3 correspond to the points in figure 4.1.

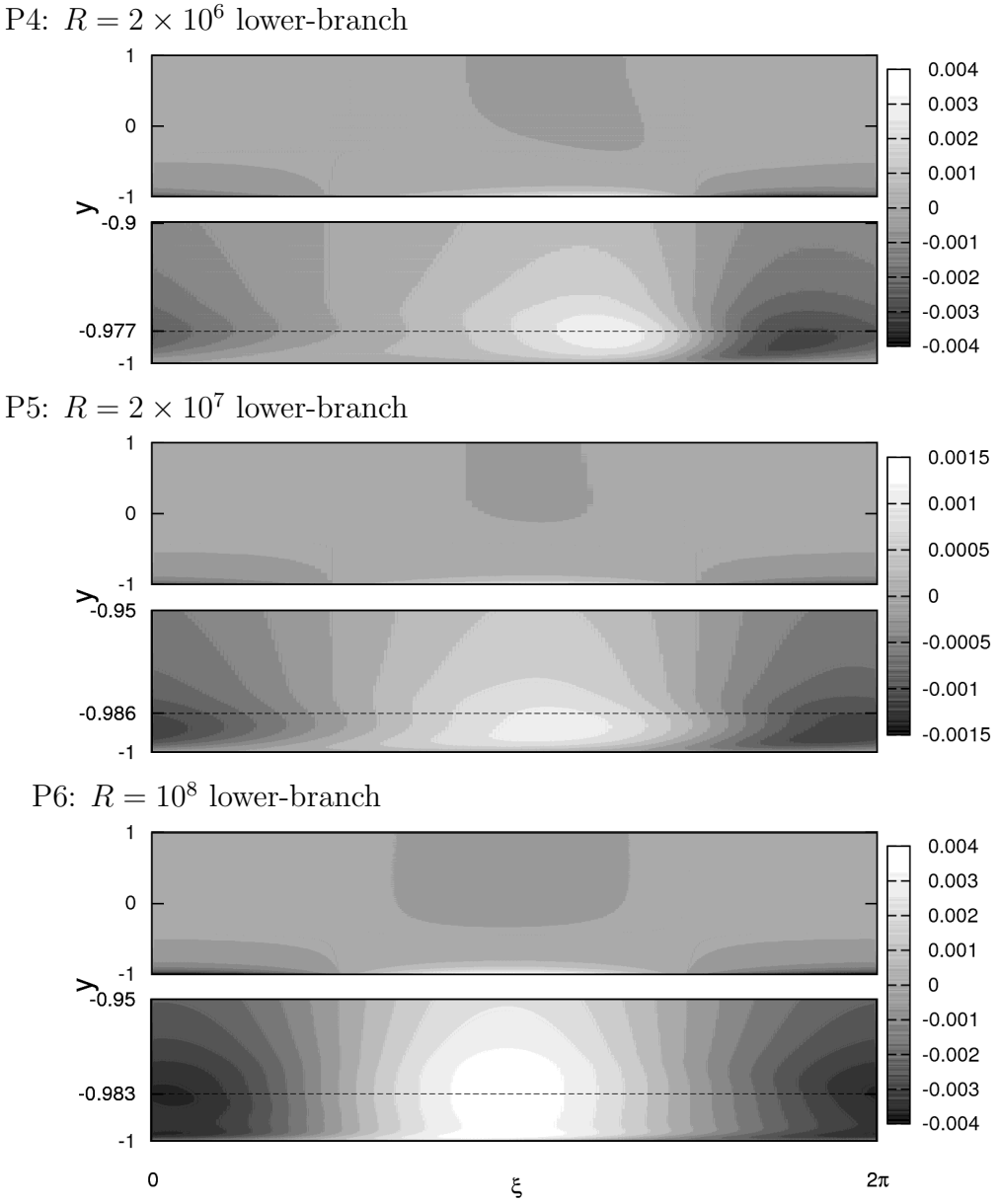

Figure 4.3: Same parameter values as figure 4.2 but for the solutions at the points P4, P5, P6.

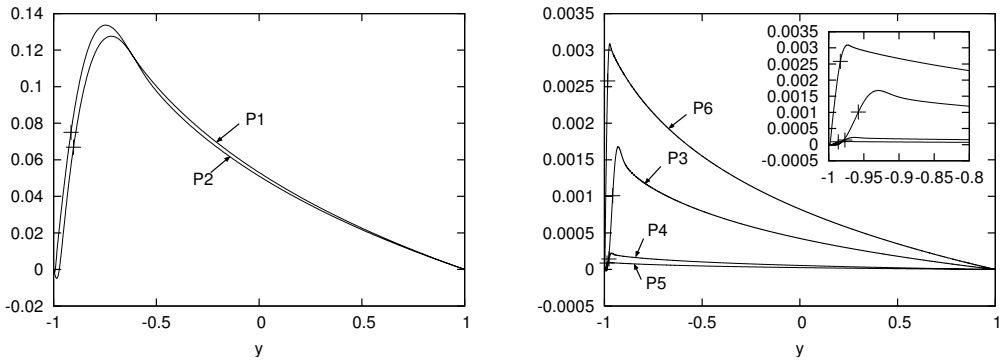

Figure 4.4: The mean-flow distortion $\bar{u}$ of the travelling-wave solutions. The vertical axis is normalized by R. Left and right figures correspond to upper- and lower-branch solutions. The crosses on the curves represent the critical layer locations y_c.

the vicinity of the critical layer y_c, where the basic flow speed, U_B, coincides with the wavespeed c of the travelling-wave solution. In these cases, the critical layer is situated near the inner wall: the distance between the critical layer and inner wall is only 5% of the gap (see figure 4.1(b)). As we move towards the point P3, which lies on the lower-branch, the positive part of the flow pattern begins to be squeezed in the axial direction. Then as R is increased along the lower-branch (P4, P5), the critical layer moves even closer to the inner wall (typically it is now at 1% of the gap from the inner wall) and the strong positive/negative flow pattern is again evenly-spaced, although it is now much more concentrated than it was on the upper-branch. The magnitude of the solution decreases as the branch approaches the linear instability, but it begins to grow again after the linear neutral point is passed (P6). The computation of the solution beyond P6, where R is in excess of 10^8, is very difficult because of the Gibbs phenomena of the Chebyshev basis due to large solution gradients in the neighbourhood of y_c. This feature can also be found in the mean-flow distortion plot for P1–P6, which is presented in figure 4.4. When we examine the high Reynolds number structure of this mode in the next section we will see that a thin critical layer, centred at $y = y_c$, regularizes this apparent singularity.

To examine the geometry dependence of the travelling-wave solutions, the solution branches are calculated for various η and R, fixing $\alpha = 0.6546$. The results are shown in figure 4.5, where the solution branches, shown as solid lines, bifurcate from the thick dashed curve traced in the $\Delta = 1$ plane, which represents the linear neutral curve for $\alpha = 0.6546$. When η is increased to 0.14, the HR mode and the LR mode are separated into an open branch and a closed branch respectively. Owing to this separation, the branch has three turning points when η is varied at fixed sufficiently high R. Since we originally defined the HR and LR modes in terms of their positions with respect to the kink, it seems reasonable to consider the first turning point encountered as Δ is increased from unity to represent the existence boundary for the LR mode. This boundary defines a critical value of η, beyond which the LR mode ceases to exist, and its variation with R is plotted in figure 4.6 for $\alpha = 0.6546, 0.2, 0.1$ and 0.05. The linear neutral curves and the branches of the solution in figure 4.5 are also projected on this figure. We can see clearly that the solution

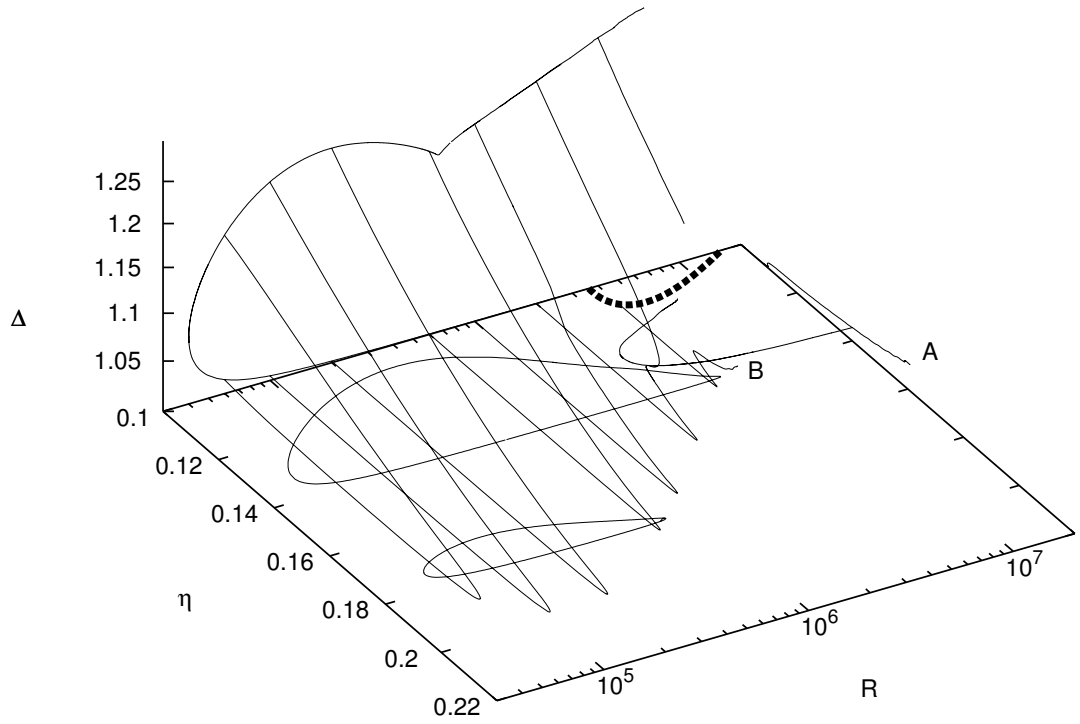

Figure 4.5: The bifurcating branches of the axisymmetric travelling-wave solutions (solid lines) from the linear neutral curve (thick dashed line) with $\alpha = 0.6546$. The base level is placed at $\Delta = 1$. The range of truncation level $L \in [120, 200]$ and $N \in [30, 60]$ is used to compute the solution branches.

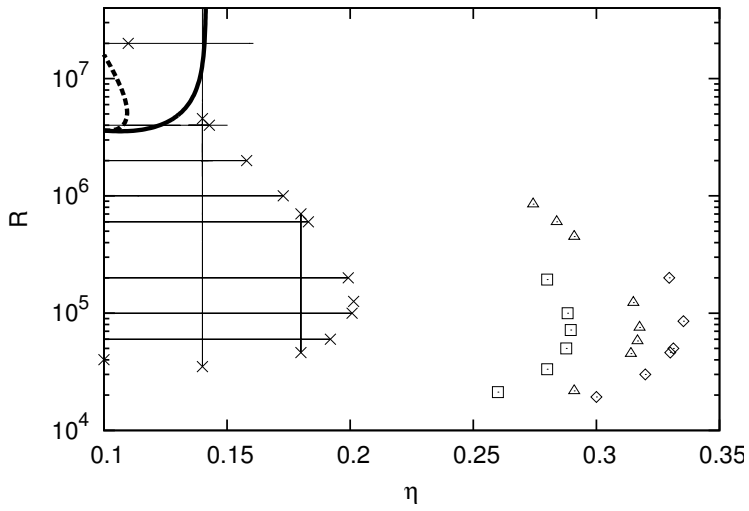

Figure 4.6: First turning points from the lower-branch, which represent the edge of the existence of the LR mode. $\times, \square, \triangle$ and $\diamond$ are calculated with $\alpha = 0.6546, 0.2, 0.1$ and 0.05 respectively. Lines in the figure are the projection of figure 4.5. The thick solid line represents the linear neutral curve taken over all wavenumbers.

can exist well beyond the longwave cut-off of linear instability, where the thick solid line heads sharply towards $R = \infty$ at $\eta = 0.1415$, and the branch extends to larger η as α is decreased. The maximum η of the LR mode is at relatively low R for all α, and then it monotonically decreases for higher R. In contrast, the present calculations suggest that the existence region of the HR mode expands as R is increased. We cannot be certain about this however, because there are resolution issues associated with continuing the branches beyond the points marked 'A' and 'B' in figure 4.5

4.2 Asymptotic solution at large Reynolds number

In this section we propose a nonlinear equilibrium travelling-wave structure for SCF, valid for asymptotically large values of the Reynolds number. For this purpose, only in this section the velocity scale is changed to the sliding velocity, U_s, so that the leading magnitude of velocity stays $O(1)$ for all R. Therefore, under the assumption of axisymmetry, the velocity disturbance $\mathbf{u} = u\mathbf{e}_x + v\mathbf{e}_r$ and the pressure disturbance p to the basic flow, which are rescaled by R and R^2 respectively from previous sections, satisfy

$$u_t + U_B\, u_x + vU_B' + \mathbf{u}\cdot\nabla u = -p_x + R^{-1}\triangle u, \tag{4.2}$$

$$v_t + U_B v_x + \mathbf{u}\cdot\nabla v = -p_r + R^{-1}(\triangle v - r^{-2}v), \tag{4.3}$$

$$u_x + v_r + r^{-1}v = 0, \tag{4.4}$$

together with the no-slip boundary conditions

$$u = v = 0 \text{ at } r = r_a \text{ and } r = r_b.$$

Here we use the notation

$$\nabla = \mathbf{e}_r\partial_r + \mathbf{e}_x\partial_x, \quad \triangle = \partial_{rr}^2 + r^{-1}\partial_r + \partial_{xx}^2 \tag{4.5}$$

and a prime denotes a derivative with respect to r.

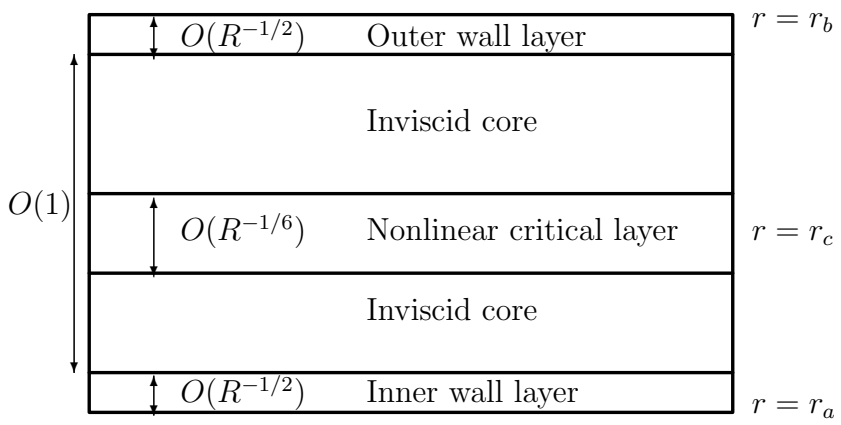

Figure 4.7: Sketch of the high Reynolds number asymptotic travelling-wave structure for axisymmetric SCF.

The asymptotic structure consists of a core region of $O(1)$ radial extent in which the flow dynamics are linear and inviscid to leading order, with viscous wall layers adjacent to the inner and outer cylinders. We assume that the wavenumber α is $O(1)$, with the unknown real wavespeed $c \sim O(1)$, and $1 - c \sim O(1)$ (note that c is also rescaled by R from the previous section). As a consequence, a singularity is encountered within the core region at the location r_c where $U_B(r_c) = c$. This singularity is regularized within a thin nonlinear critical layer. The phase shifts induced across the two wall layers must be balanced by the corresponding phase shift induced across the critical layer, and this requirement leads to the determination of the amplitude of the disturbance in terms of its axial wavenumber and the properties of the basic flow. A sketch of the flow structure is shown in Figure 4.7. The structure is similar to that found by Smith & Bodonyi (1982a) for fully-developed PF, and Walton (2002, 2003) for impulsively-started PF and pressure-driven annular Couette-Poiseuille flow. A key difference to the previous studies is the assumption of axisymmetry. We find that unlike for PF, axisymmetric solutions are indeed possible here. One of the reasons for this is that, for the fully-developed flow through a circular pipe, the combination $U_B'' - U_B'/r$ is zero, in contrast to the flow under consideration here, where this quantity remains positive throughout the annulus. It is the non-zero nature of this term that gives rise to the logarithmic singularity referred to above, and evident in (4.14) below. The same arguments mean that this structure is also absent for PCF, implying that the asymptotic structures presented here does not exist in the narrow gap limit.

The flow behaviour in the various regions is set out in the following subsections.

4.2.1 The inviscid core flow

In the core, the flow dynamics are inviscid to leading order, with the flow expansions assuming the form

$$\begin{aligned} u &= \varepsilon\overline{u}_1(r) + \varepsilon^2\left\{A_0F_2(r)\cos\xi + \overline{u}_2(r)\right\} \\ &\quad + \cdots + \varepsilon^2R^{-1/2}u_5(\xi,r) + \cdots, \\ v &= -\varepsilon^2A_0G_2(r)\sin\xi + \cdots + \varepsilon^2R^{-1/2}v_5(\xi,r) + \cdots, \\ p &= \varepsilon^2A_0P_2(r)\cos\xi + \cdots + \varepsilon^2R^{-1/2}p_5(\xi,r) + \cdots. \end{aligned} \tag{4.6}$$

Here $\overline{u}_1(r)$ is the leading-order mean-flow distortion term and ε is a small parameter that will be determined in terms of the Reynolds number subsequently. The real constant A_0 is also to be determined, and the variable ξ is the same travelling-wave coordinate defined in (2.13). The terms with subscript 5 are the highest-order terms that break the [even, odd, even] symmetry of $[u, v, p]$ about $\xi = \pi$, i.e.

$$[u_5, v_5, p_5] \text{ contain terms } A_0\left[F_5(r)\sin\xi, G_5(r)\cos\xi, P_5(r)\sin\xi\right]. \tag{4.7}$$

In order to fix the phase of the solution we impose the phase normalization condition

$$P_2(r_c) = 1, \tag{4.8}$$

where $r = r_c$ is the location of the critical layer, i.e. the radial location where $U_B(r_c) = c$, with U_B the basic flow defined in (2.5). The choice of (4.8) is mainly for algebraic simplicity. If we do not impose this condition then the quantity $P_2(r_c)$ will appear in expressions throughout the critical-layer analysis below.

4.2.1.1 The core-flow fluctuation

Substitution of (4.6) into the Navier-Stokes equations (4.4)–(4.4) leads to the following inviscid balances:

$$(U_B(r) - c)\alpha F_i + G_i U_B' = -\alpha P_i, \;\; (U_B(r) - c)\alpha G_i = P_i', \tag{4.9}$$

for $i \in \{2, 5\}$, together with the continuity equation. Further manipulation and elimination of the velocity components leads to Rayleigh equations for the pressure components

$$(U_B(r) - c)\left(P_i'' + r^{-1}P_i' - \alpha^2 P_i\right) = 2U_B' P_i', \;\; i \in \{2, 5\}. \tag{4.10}$$

For the P_2-component, the appropriate boundary conditions are

$$P_2'(r_a) = P_2'(r_b) = 0, \tag{4.11}$$

which arise from imposition of the condition of zero radial velocity at the wall. For the P_5-component, the wall-layer analysis (subsection 4.2.2) predicts the existence of a non-zero radial velocity component of $O(\varepsilon^2 R^{-1/2})$ as each wall is approached, implying that the appropriate conditions on the radial fluctuation in the core are

$$G_5(r_a) = g_a, \;\; G_5(r_b) = g_b, \tag{4.12}$$

with the precise values of g_a and g_b to be fixed in (4.31), (4.37). In terms of the pressure, the boundary conditions are therefore

$$P_5'(r_a) = (1 - c)\alpha g_a, \;\; P_5'(r_b) = -\alpha c g_b, \tag{4.13}$$

from the radial momentum balance in (4.9).

For the purposes of the critical-layer analysis to be presented in section 4.2.3, we need to know the limiting behaviour of the flow as the critical layer is approached. This can be

calculated by the Frobenius method, and the relevant asymptotes, as $r \to r_c\pm$, are:

$$\begin{aligned} P_i &\sim P_i(r_c)\left[1 - \frac{\alpha^2 r_c^2}{2}\left(\frac{r_c - r}{r_c}\right)^2 - \frac{2\alpha^2 r_c^2}{3}\left(\frac{r_c - r}{r_c}\right)^3\left(\ln\left|\frac{r_c - r}{r_c}\right| + j_\pm^{(i)}\right) + \cdots\right], \\ F_i &\sim 2\tau_0^{-1} P_i(r_c)\left[\ln\left|\frac{r_c - r}{r_c}\right| + j_\pm^{(i)} + \frac{1}{6}(1 + \frac{5\tau_1}{\tau_0}) + \cdots\right], \end{aligned} \tag{4.14}$$

(with a similar expansion for G_i) for $i \in \{2, 5\}$, with the $\pm$ denoting the limits $r \to r_c \pm$. Here we have defined

$$\tau_0 = -r_c U_B'(r_c) = -(\ln \eta)^{-1}, \;\; \tau_1 = (r_c^2/2) U_B''(r_c) = -(2 \ln \eta)^{-1}, \tag{4.15}$$

to represent the shear and curvature of the basic flow at the critical location, and we have made use of the property $2\tau_1/\tau_0 = 1$ to simplify the expressions slightly. The constants $j_\pm^{(i)}$ are determined by solving the Rayleigh equation for P_i numerically. This is described for P_2 in more detail in subsection 4.2.1.2 below. A feature of the nonlinear critical layer is the smallness of the jump in velocity and pressure induced across it, in contrast with a classical linear critical layer in which the phase shift is $O(1)$ (c.f. Healey 1995). This feature can be anticipated here by taking $j_+^{(2)} = j_-^{(2)}$. However it will be necessary for $j_+^{(5)} - j_-^{(5)}$ to be non-zero in order to accommodate the velocity jump across the critical layer. We shall see that the critical layer analysis shows that there is a jump

$$\varepsilon^2 R^{-1/2} \varphi \sin \xi \tag{4.16}$$

in the streamwise velocity as we cross the critical layer from $r = r_c-$ to $r = r_c+$, with φ determined specifically in (4.57). In terms of the core properties, we therefore have

$$\varphi = 2A_0 P_5(r_c) \tau_0^{-1} (j_+^{(5)} - j_-^{(5)}), \tag{4.17}$$

in view of the asymptotic expansion for F_5 in (4.14). The quantity $(j_+^{(5)} - j_-^{(5)})$ can be related to the wall velocities g_a, g_b, by considering the Wronskian of the solutions to (4.10),

which has the form

$$r(U_B(r) - c)^{-2}(P_5 P_2' - P_2 P_5') = \omega_{\pm}. \tag{4.18}$$

Applying the boundary conditions (4.11), (4.13), we can determine the constants $\omega_{\pm}$ as

$$\omega_+ = \alpha g_b r_b P_2(r_b)/c, \;\; \omega_- = -\alpha g_a r_a P_2(r_a)/(1-c). \tag{4.19}$$

Then, letting $r \to r_c\pm$ in (4.18), using the series expansions in (4.14) for P_2 and P_5, and the phase normalization (4.8) we find that (4.17) can be rewritten as

$$\varphi = -(\omega_+ - \omega_-)\alpha^{-2} r_c^{-2} A_0 \tau_0, \tag{4.20}$$

so that the velocity jump across the critical layer is now related to the wall-layer properties by (4.19) and (4.20).

4.2.1.2 The numerical solution of the Rayleigh equation

Aside from a number of numerical integrations, the only part of the asymptotic analysis where a non-trivial numerical approach is required is in the solution of the Rayleigh equation (4.10) for $P_2(r)$. This solution is important as it yields, for a given wavenumber α, the corresponding wavespeed c, and hence the location r_c of the critical layer. We briefly describe the method we used here for α of $O(1)$ and also the corresponding approach for the limiting case $\alpha \to 0$.

(i) *Solution for α of $O(1)$*

First we introduce a new radial variable s such that $r = r_c s$ and define $s_a = r_a/r_c, s_b = r_b/r_c, \widehat{\alpha} = \alpha r_c$. The Rayleigh equation (4.10) for $P_2(r) = Q(s)$ say, can then be rewritten as

$$Q''(s) + \frac{1}{s}Q'(s) - \widehat{\alpha}^2 Q(s) = \frac{2}{s}(\ln s)^{-1} Q'(s), \;\; Q'(s_a) = Q'(s_b) = 0, \; Q(1) = 1. \tag{4.21}$$

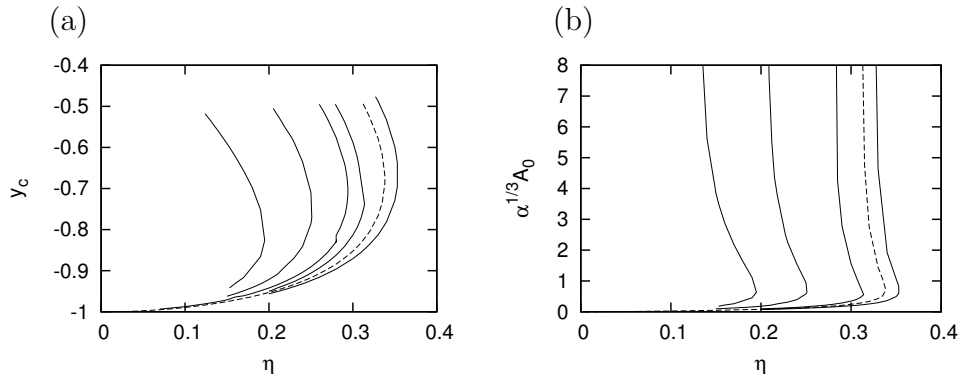

Figure 4.8: (a): Critical layer location y_c versus η. The solid lines are from left to right: $\alpha = 1.5, 1.0, 0.6546, 0.5, 0.1$ while the dotted line is the $\alpha \to 0$ asymptote. (b): Normalized amplitude $\alpha^{1/3}A_0$ versus η with same labeling as figure (a).

For fixed values of s_a and $\widehat{\alpha}$, (4.21) is marched forward from $s = s_a$ with a guess for $Q(s_a)$ (equal to Q_g, say). The values of Q and Q' are found at $s = s_1 = (1 + s_a)/2$. Equation (4.21) is then marched backwards from $s = s_2 = 1 - \varepsilon_1$ (with ε_1 suitably small) using the series expansion (4.14) to provide values for $Q(s_2), Q'(s_2)$. A guess is made for the constant $j_-^{(2)}$. As a result of this procedure we can calculate a second set of values for $Q(s_1), Q'(s_1)$. We then iterate on the guesses Q_g and $j_-^{(2)}$ until the two estimates for Q and Q' at s_1 are in agreement. Next we set $j_+^{(2)} = j_-^{(2)}$ (as discussed just below (4.15)) and march (4.21) forward from $s = 1 + \varepsilon_1$, again using the series expansion for P_2 in (4.14) to provide suitable starting values. The marching process is stopped when the location s_b is reached at which $Q'(s_b) = 0$. The required value for the critical layer location is then given by $r_c = r_b s_b^{-1}$. The wavespeed follows from $c = U_B(r_c)$ and the corresponding wavenumber and radius ratio from $\alpha = r_c^{-1}\widehat{\alpha}, \eta = s_a/s_b$. The pressure at both walls is also required later and so these values are also stored. Clearly this procedure can be repeated for a range of wavenumbers and radius ratios.

A typical computation result is plotted in figure 4.8 (a). The location of the critical layer gradually shifts from near the inner wall towards the centre of the gap as η increases. A turning point in the $y_c = y_c(\eta)$ profile can be observed typically at around $\eta = 0.1 \sim 0.4$. After the turning point, the branch is terminated at the point where the corresponding wave amplitude A_0, whose explicit form will be given in subsection 4.2.2.2, blows up as shown in figure 4.8 (b).

(ii) *Solution in the limit* $\alpha \to 0$

In addition to providing a partial check on the accuracy of the numerical procedure outlined in part (i), the form of the solution of the Rayleigh equation (4.10) as $\alpha \to 0$ is significant as it provides an important clue as to the form of the new long-wave solution structure that emerges in place of the present structure when $\alpha \sim O(R^{-1})$.

If we consider the inviscid disturbance equations (4.9) in the core, together with the continuity balance, we find that as $\alpha \to 0$:

$$F_2 \sim F_{20}(r) + O(\alpha^2), \;\; G_2 \sim \alpha G_{20}(r) + O(\alpha^3), \;\; P_2 \sim P_{20} + O(\alpha^2), \tag{4.22}$$

where P_{20} is a constant. The leading-order terms (F_{20}, G_{20}, P_{20}) satisfy the balances

$$F_{20} + G'_{20} + G_{20}/r = 0, \;\; (U_B(r) - c)F_{20} + G_{20}U'_B = -P_{20},$$

and elimination of F_{20} leads to the result

$$\frac{rG_{20}}{(U_B - c)} = \begin{cases} P_{20} \int_{r_a}^{r} s(U_B(s) - c)^{-2}\, ds, & (r < r_c), \\ P_{20} \int_{r_b}^{r} s(U_B(s) - c)^{-2}\, ds, & (r > r_c). \end{cases}$$

Across the critical layer we have a zero jump in the component G_{20} and this implies that the following integral condition must hold:

$$\fint_{r_a}^{r_b} \frac{r\, dr}{(U_B(r) - c)^2} = 0, \tag{4.23}$$

where the bar denotes the finite part of the integral. Equation (4.23) can be viewed as the $\alpha \to 0$ limit of the Rayleigh equation (4.10) and determines the solutions for the leading-order wavespeed c for a given value of radius ratio η. To evaluate the integral numerically we make the substitution $s = r/r_c$ as in part (i) and use the specific form for U_B given in

(2.5). The integral condition (4.23) can then be rewritten as

$$⨍_{\eta s_c}^{s_c} \frac{s\,ds}{(\ln s)^2} = 0, \tag{4.24}$$

which determines the values of the quantity $s_c = r_b/r_c$. The finite-part integral in (4.24) can then be easily evaluated by using integration by parts as, for example, in Appendix B of Walton (2011).

This result is also traced in figure 4.8 as the dashed line. The behaviour of the branch is consistent with the computational results for $\alpha \sim O(1)$, i.e. there exist turning and termination points on the branch, suggesting that the generic conclusion for SCF: there is no nonlinear asymptotic structure when $\eta \gtrsim 0.40$. It is also of interest that the cut-off point, i.e. maximum value of η is close to the value givem in the long-wave limit.

4.2.1.3 The mean-flow distortion in the core

Again, from substitution of the expansions (4.6) into the Navier-Stokes equations (4.4)−(4.4), we find that the leading-order contribution to the mean-flow distortion satisfies

$$\overline{u}_1'' + r^{-1}\overline{u}_1' = A_0^2\left(G_5F_2' - G_2F_5'\right)/2 = 0,$$

using (4.9) and (4.18), so that the distortion is unforced in the core at this order. The solution satisfying no-slip at the walls therefore has the simple form

$$\overline{u}_1 = \begin{cases} M_a \ln(r/r_a), & (r_a < r < r_c), \\ M_b \ln(r/r_b), & (r_c < r < r_b). \end{cases} \tag{4.25}$$

The solution in the critical layer requires that $\overline{u}_1$ be continuous across $r = r_c$, but that there is a jump in $\overline{u}_1'$. We therefore have

$$M_a \ln(r_c/r_a) = M_b \ln(r_c/r_b), \tag{4.26}$$

with $M_b - M_a$ non-zero and to be determined later, in terms of the disturbance amplitude, by the critical-layer analysis. Although the mean flow distortion is unforced in the core, it *is* forced in the wall layers, and the specific forms that it takes will be determined in the next subsection where we consider those layers in some detail.

4.2.2 The viscous wall layers

Since the dynamics in the core are inviscid to leading order, the leading-order axial fluctuation $F_2(r)$ does not tend to zero as $r \to r_a, r_b$. Viscous wall layers are therefore required in order that the no-slip condition can be satisfied.

4.2.2.1 The boundary-layer on the inner cylinder

The boundary-layer has the classical $O(R^{-1/2})$ thickness, and the relevant flow expansions are

$$\begin{aligned} U_B + u &= 1 + \varepsilon^2 u_a(\xi, Z_a) + R^{-1/2} U_B'(r_a) Z_a + \varepsilon^4 \overline{\mathcal{U}}_a(Z_a) + \cdots , \\ v &= \varepsilon^2 R^{-1/2} v_a(\xi, Z_a) + \cdots , \quad p = \varepsilon^2 A_0 P_2(r_a) \cos\xi + \cdots , \end{aligned} \tag{4.27}$$

with $r = r_a + R^{-1/2} Z_a$, where we have anticipated the independence of the pressure on the normal coordinate. The continuity and axial momentum balances for the fluctuation terms are

$$\alpha \frac{\partial u_a}{\partial \xi} + \frac{\partial v_a}{\partial Z_a} = 0, \quad \alpha(1-c)\frac{\partial u_a}{\partial \xi} = \alpha A_0 P_2(r_a) \sin\xi + \frac{\partial^2 u_a}{\partial Z_a^2},$$

with $u_a = v_a = 0$ on $Z_a = 0$ and the condition of no exponential growth as $Z_a \to \infty$. The appropriate solutions are

$$u_a = \frac{1}{2}\mathcal{F}_a(Z_a) e^{\mathrm{i}\xi} + \text{c.c.}, \quad v_a = \frac{1}{2}\mathcal{G}_a(Z_a) e^{\mathrm{i}\xi} + \text{c.c.}, \tag{4.28}$$

with

$$\mathcal{F}_a(Z_a) = -\frac{A_0 P_2(r_a)(1-e^{-\mu_a Z_a})}{(1-c)}, \tag{4.29}$$

$$\mathcal{G}_a(Z_a) = \frac{\mathrm{i}\,\alpha A_0 P_2(r_a)\left(Z_a+\mu_a^{-1}(e^{-\mu_a Z_a}-1)\right)}{(1-c)}, \tag{4.30}$$

and $\mu_a = (\mathrm{i}\,\alpha(1-c))^{1/2}$. Taking the limit of (4.30) as $Z_a \to \infty$ and matching to the core, we conclude that

$$g_a = -\alpha^{1/2}2^{-1/2}(1-c)^{-3/2}P_2(r_a). \tag{4.31}$$

The mean-flow distortion is forced by the fluctuation and satisfies

$$\overline{\mathcal{U}}_a'' = \frac{1}{4}\mathcal{G}_a^*(Z_a)\mathcal{F}_a'(Z_a) + \text{c.c.},$$

with $\overline{\mathcal{U}}_a \sim M_a Z_a/r_a$ as $Z_a \to \infty$ to match to the core flow (4.25) and $\overline{\mathcal{U}}_a(0) = 0$ to satisfy the no-slip condition. Use of (4.29), (4.30) for $\mathcal{F}_a, \mathcal{G}_a$ and integration leads to the explicit expression

$$\begin{aligned}\overline{\mathcal{U}}_a = {} & \frac{(A_0P_2(r_a))^2}{4(1-c)^3}(2(m_aZ_a+2)\cos(m_aZ_a)\,e^{-m_aZ_a} \\ & +2(m_aZ_a-1)\sin(m_aZ_a)e^{-m_aZ_a} - e^{-2m_aZ_a} - 3) + \frac{M_aZ_a}{r_a},\end{aligned} \tag{4.32}$$

with $m_a = \Re(\mu_a) = (\alpha(1-c)/2)^{1/2}$.

4.2.2.2 The boundary-layer on the outer cylinder

Since the basic flow is zero on the outer cylinder, the appropriate expansion in the upper layer is

$$\begin{aligned}U_B + u &= \varepsilon^2 u_b(\xi, Z_b) - R^{-1/2}U_B'(r_b)Z_b + \varepsilon^4\overline{\mathcal{U}}_b(Z_b) + \cdots, \\ v &= -\varepsilon^2 R^{-1/2}v_b(\xi, Z_b) + \cdots, \quad p = \varepsilon^2 A_0 P_2(r_b)\cos\xi + \cdots,\end{aligned} \tag{4.33}$$

with $r = r_b - R^{-1/2}Z_b$. The governing equations for the fluctuations and the mean-flow distortion are very similar to those in the inner boundary layer and the method of solution proceeds in an identical fashion to yield

$$u_b = \frac{1}{2}\mathcal{F}_b(Z_b)e^{\mathrm{i}\xi} + \text{c.c.}, \quad v_b = \frac{1}{2}\mathcal{G}_b(Z_b)e^{\mathrm{i}\xi} + \text{c.c.}, \tag{4.34}$$

with

$$\mathcal{F}_b(Z_b) = \frac{A_0 P_2(r_b)(1 - e^{-\mu_b Z_b})}{c}, \tag{4.35}$$

$$\mathcal{G}_b(Z_b) = -\frac{\mathrm{i}\alpha A_0 P_2(r_b)\left(Z_b + \mu_b^{-1}(e^{-\mu_b Z_b} - 1)\right)}{c}, \tag{4.36}$$

and $\mu_b = (-\mathrm{i}\alpha c)^{1/2}$. From the expression for $\mathcal{G}_b$ we can calculate that

$$g_b = \alpha^{1/2} 2^{-1/2} c^{-3/2} P_2(r_b). \tag{4.37}$$

The corresponding solution for the mean-flow distortion is found to be

$$\begin{aligned}\overline{\mathcal{U}}_b = &-\frac{(A_0 P_2(r_b))^2}{4c^3}(2(m_b Z_b + 2)\cos(m_b Z_b)\, e^{-m_b Z_b} \\ &+2(m_b Z_b - 1)\sin(m_b Z_b)e^{-m_b Z_b} - e^{-2m_b Z_b} - 3) - \frac{M_b Z_b}{r_b},\end{aligned} \tag{4.38}$$

with $m_b = \Re(\mu_b) = (\alpha c/2)^{1/2}$. Here we have applied no slip on $Z_b = 0$ and the core-matching condition $\overline{\mathcal{U}}_b \sim -M_b Z_b / r_b$ as $Z_b \to \infty$.

Now that we have determined the radial velocities g_a and g_b, we can rewrite the jump condition (4.20) as

$$\varphi = \frac{A_0 \tau_0}{(2\alpha)^{1/2} r_c^2}\left\{\frac{r_a\left[P_2(r_a)\right]^2}{(1-c)^{5/2}} - \frac{r_b\left[P_2(r_b)\right]^2}{c^{5/2}}\right\}. \tag{4.39}$$

The aim now is to investigate the dynamics of the critical layer with a view to obtaining an alternative, amplitude-dependent expression for φ, and hence determining the amplitude dependence of the neutral modes.

4.2.3 The critical-layer analysis

The aims of the critical-layer analysis are three-fold. The first is to determine the small parameter ε in terms of the Reynolds number R. Next, the jump in the mean-flow distortion across the critical-layer is calculated, and allows us to determine the constants M_a, M_b introduced in (4.25), thus fixing the core mean-flow distortion. Finally, we find the velocity jump across the layer in terms of the disturbance amplitude A_0, which can then be determined explicitly as a result.

The velocity and pressure expansions are as follows

$$\begin{aligned} U_B + u &= c + \varepsilon\widehat{U}_1 + (\varepsilon^2 \ln\varepsilon)\widehat{U}_{2L} + \varepsilon^2\widehat{U}_2 + \cdots + \varepsilon^5\widehat{U}_5 + \cdots, \\ v &= \varepsilon^2\widehat{V}_1 + (\varepsilon^3 \ln\varepsilon)\widehat{V}_{2L} + \varepsilon^3\widehat{V}_2 + \cdots + \varepsilon^6\widehat{V}_5 + \cdots, \\ p &= \varepsilon^2\widehat{P}_1 + \varepsilon^3\widehat{P}_2 + \cdots + \varepsilon^6\widehat{P}_5 + \cdots, \end{aligned} \tag{4.40}$$

with $r = r_c + \varepsilon Y$. The solutions at the first two orders, which match appropriately to the core via (4.6) and (4.14), are relatively simple and can be shown to be

$$\widehat{U}_1 = -\tau_0 Y/r_c + \overline{u}_1(r_c), \quad \widehat{V}_1 = -\mu\sin\xi, \quad \widehat{P}_1 = A_0\cos\xi, \tag{4.41}$$

$$\widehat{U}_{2L} = 2A_0\tau_0^{-1}\cos\xi, \quad \widehat{V}_{2L} = 2\alpha A_0\tau_0^{-1} Y\sin\xi, \tag{4.42}$$

where the amplitude parameter μ is defined by

$$\mu = \alpha r_c A_0 \tau_0^{-1}. \tag{4.43}$$

The terms with subscript 2 in (4.40) are the first to possess a non-trivial dependence on the radial coordinate. The governing equations for these terms are

$$\begin{aligned} \alpha\widehat{U}_{2\xi} + \widehat{V}_{2Y} + \widehat{V}_1/r_c = 0, \quad \widehat{P}_{2Y} = 0, \\ \alpha\left\{\widehat{U}_1\widehat{U}_{2\xi} + \widehat{U}_2\widehat{U}_{1\xi}\right\} + \widehat{V}_2\widehat{U}_{1Y} + \widehat{V}_1\widehat{U}_{2Y} = -\alpha\widehat{P}_{2\xi}, \end{aligned} \tag{4.44}$$

and the match to the core requires

$$\begin{aligned}\widehat{U}_2 \;\sim\; & \tau_1 Y^2/r_c^2 + \overline{u}_1'(r_c\pm)Y + 2A_0\tau_0^{-1}\ln\left|r_c^{-1}Y\right|\cos\xi \\ & + A_0\tau_0^{-1}\left(2j^{(2)} + (1/3)(1+5\tau_1/\tau_0)\right)\cos\xi, \end{aligned} \tag{4.45}$$

as $Y \to \pm\infty$, in view of (4.14). Differentiating the third of equations (4.44) with respect to Y, using (4.41) for $\widehat{U}_1, \widehat{V}_1$, and switching to a characteristic variable

$$\Xi = \frac{\alpha\tau_0}{2r_c}\left(Y - r_c\overline{u}_1(r_c)\tau_0^{-1}\right)^2 + \mu\cos\xi, \tag{4.46}$$

we eventually obtain the following expression for the shear term $\widehat{U}_{2Y}$:

$$\widehat{U}_{2Y} = \mp(2\tau_0/\alpha r_c^3)^{1/2}(\Xi - \mu\cos\xi)^{1/2} + \kappa(\Xi). \tag{4.47}$$

An asymptotic condition on the unknown function κ can be found by applying the matching condition (4.45), and this yields:

$$\kappa(\Xi) \sim \pm 2^{3/2}\tau_0^{1/2}(\alpha r_c^3)^{-1/2}\Xi^{1/2} + \Lambda_\pm, \text{ as } \Xi \to \infty, \tag{4.48}$$

where the constants $\Lambda_\pm$ are undetermined at this order. Here, the $\pm$ signs refer to the upper/lower parts of the critical layer wherein $Y - r_c\overline{u}_1(r_c)\tau_0^{-1} > (2r_c\mu(1-\cos\xi)/\alpha\tau_0)^{1/2}$, and $Y - r_c\overline{u}_1(r_c)\tau_0^{-1} < -(2r_c\mu(1-\cos\xi)/\alpha\tau_0)^{1/2}$, respectively. Later in the analysis it will become clear that $\Lambda_+ \neq \Lambda_-$, and this jump fixes the leading-order mean-flow distortion in the core, via the matching condition (4.45).

The [even, odd, even] symmetry about $\xi = \pi$ of the solution $[\widehat{U}_m, \widehat{V}_m, \widehat{P}_m]$ is not broken until viscous effects enter the critical layer equations. Since (from (4.41)) we have $\widehat{U}_{1YY} = 0$, the first non-zero term of this type is $\widehat{U}_{2YY}$, which makes a contribution at $O(R^{-1})$ in the axial momentum equation that determines the quantity $\widehat{U}_5$. Balancing inertia and viscosity at

this order requires $\varepsilon^3 R^{-1/2} \sim R^{-1}$, and hence fixes the small parameter

$$\varepsilon = R^{-1/6}. \tag{4.49}$$

If we then carry on to consider the equations at the $m = 5$ level and impose periodicity in ξ (which is now a non-trivial condition due to the presence of viscosity and inertia) we can determine fully the unknown function κ introduced in (4.47), and we find that

$$\kappa(\Xi) - \kappa_0 = \begin{cases} \pm 2^{3/2}\pi\tau_0^{1/2}(\alpha r_c^3)^{-1/2}\int_\mu^\Xi (I(\Xi_1))^{-1}\,d\Xi_1, & (\Xi > \mu), \\ 0, & (\Xi < \mu). \end{cases} \tag{4.50}$$

with

$$I(\Xi) = \int_0^{2\pi} (\zeta - \mu\cos\xi)^{1/2}\,d\xi. \tag{4.51}$$

The specific form given for κ in (4.50) can be deduced from equation (4.66) in Appendix 4.A.1, together with the asymptotic condition (4.48). A routine numerical calculation then shows that

$$\Lambda_+ - \Lambda_- = -(2\mu\tau_0/\alpha r_c^3)^{1/2} C_0, \;\; C_0 \simeq 3.90, \tag{4.52}$$

and this expression is equal to the distortion shear jump $\overline{u}_1'(r_c+) - \overline{u}_1'(r_c-)$, in view of (4.45). This enables us to fix the constants in the core mean-flow distortion as

$$M_a = C_1 \ln(r_c/r_b) {A_0}^{1/2}/\ln\eta, \;\; C_1 = 2^{1/2} C_0 \simeq 5.52, \tag{4.53}$$

with M_b following from (4.26). The same matching condition also allows us to determine the constant of integration κ_0 in (4.50) as

$$\kappa_0 = (2r_c)^{-1}(M_a + M_b) + 2{r_c}^{-1} M_a \ln(r_c/r_a). \tag{4.54}$$

Since κ is now fully determined, it is possible to go back and integrate (4.47) to obtain the

explicit expression

$$\widehat{U}_2 = -\frac{\Xi}{\alpha r_c} + \left(Y - \frac{r_c \overline{u}_1(r_c)}{\tau_0}\right)\kappa(\Xi) \mp \left(\frac{2r_c}{\alpha\tau_0}\right)^{1/2} \int_\mu^\Xi (\Xi - \mu\cos\xi)^{1/2}\kappa'(\Xi)\, d\Xi + q(\xi), \quad (4.55)$$

where

$$q(\xi) = \frac{\mu\cos\xi}{\alpha r_c}\left\{1 + \frac{1}{3}(1 + \frac{5\tau_1}{\tau_0}) - 2\ln\left(\alpha\tau_0/2r_c^3\mu\right)^{1/2} + 2j^{(2)}\right\} + q_0$$
$$+2(\alpha r_c)^{-1}\int_\mu^\infty \left\{2\pi(\Xi - \mu\cos\xi)^{1/2}(I(\Xi))^{-1} + (\mu\cos\xi)(2\Xi)^{-1} - 1\right\} d\Xi, \quad (4.56)$$

and q_0 is a constant, the determination of which would require higher-order analysis. Finally, in order to determine the amplitude A_0 we need to calculate the phase shift across the critical layer (i.e. the jump in the $\sin\xi$ component of axial velocity across the layer). The calculation is very similar to that performed in Walton (2003), but for the axisymmetric case. The details are given in an appendix, and lead to the expression

$$\varphi = \frac{2\tau_0 C_1}{\alpha r_c^2 A_0^{1/2}}. \quad (4.57)$$

Equating this to the expression (4.39) for φ found from the core and wall-layer analyses, enables us to derive an explicit expression for the amplitude dependence of the neutral modes:

$$A_0 = \frac{2\alpha^{-1/3}C_1^{2/3}}{\left(r_a\left[P_2(r_a)\right]^2(1-c)^{-5/2} - r_b\left[P_2(r_b)\right]^2 c^{-5/2}\right)^{2/3}}. \quad (4.58)$$

The high-Reynolds-number analysis is now complete. An independent check on the analysis can be performed by recalling from section 4 that the momentum transfer Δ defined in (2.24) is the same on both walls. In terms of our asymptotic solution this implies that $r_a\overline{\mathcal{U}}_a'(0) = -r_b\overline{\mathcal{U}}_b'(0)$ with the wall-layer solutions $\overline{\mathcal{U}}_a, \overline{\mathcal{U}}_b$ given in (4.32), (4.38). By explicit calculation it can be shown that this is indeed the case if and only if A_0 satisfies (4.58). This gives us a high degree of confidence in the correctness of the analysis presented in

this section. The corresponding expression for Δ is

$$\Delta = 1 + R^{-1/6}\left\{A_0^{1/2}C_1\ln(r_c/r_a) + \left(\frac{\alpha c}{2}\right)^{1/2} r_b \ln(1/\eta)\frac{(A_0P_2(r_b))^2}{2c^3}\right\}, \tag{4.59}$$

neglecting terms of $O(R^{-1/3})$, from which it can be seen that the perturbation to Δ is always positive.

For a given wavenumber α and radius ratio η we can compute all the necessary flow quantities to make a direct comparison with the full Navier-Stokes solutions presented in section 4.1. In order to determine quantities in the core we first solve the eigenvalue problem (4.10) to determine the pressure component $P_2(r)$, the wavespeed c and the critical layer location r_c. The amplitude of the neutral modes follows from (4.58) with C_1 given in (4.53). The core fluctuations $A_0F_2(r)\cos\xi, A_0G_2(r)\sin\xi$ can then be calculated from the solution for P_2 using (4.9). The mean-flow distortion $\overline{u}_1(r)$ in the core follows from (4.25), (4.26) and (4.53). The fluctuations in the wall layers are given by (4.27), (4.28), (4.29) and (4.30) for the inner layer, and (4.33), (4.34), (4.35) and (4.36) for the layer on the outer cylinder. The mean-flow distortions in the two wall layers can be calculated from (4.27), (4.32) and (4.33), (4.38). Finally, in the critical layer, we have found expressions for the first three terms $\widehat{U}_1, \widehat{U}_{2L}, \widehat{U}_2$ in the streamwise velocity expansion in (4.40) and these are given in (4.41), (4.42) and (4.55).

4.2.4 Comparison of asymptotic and numerical results

In the previous subsection we proposed an asymptotic form for the nonlinear instability of SCF. Now we wish to compare this solution with our Navier-Stokes computations from section 4.1. In particular, we are interested in: (i) how large the Reynolds number needs to be to obtain reasonable agreement between the solutions, (ii) which, if any, of the modes discovered in section 4.1 does the asymptotic solution best approximate and (iii) is it possible to see the delicate asymptotic flow structure in the finite Reynolds number computations?

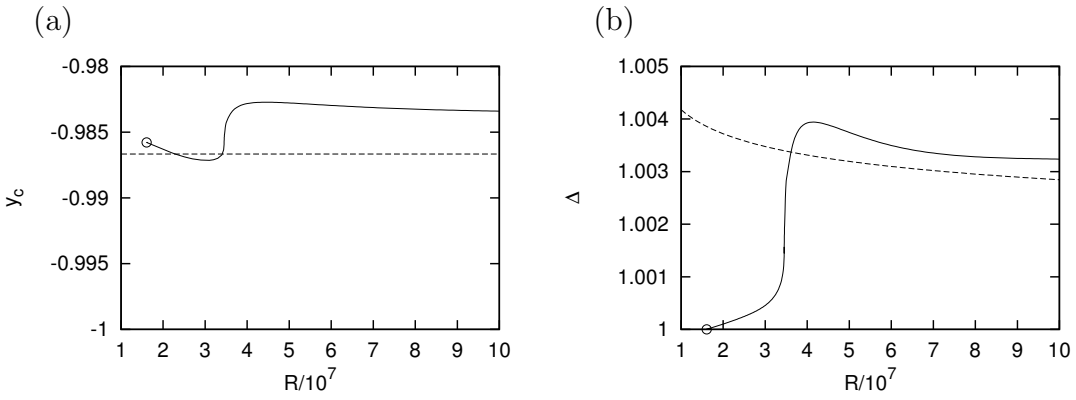

Figure 4.9: The solid lines represent the lower- branch solution for $(\eta, \alpha) = (0.1, 0.6546)$. The truncation level $(L, N) = (240, 100)$ is used. The dashed lines are asymptotic results $y_c = -0.9866$ and $\Delta = 1 + 0.0613R^{-1/6}$. Open circles in the figures represent linear critical points.

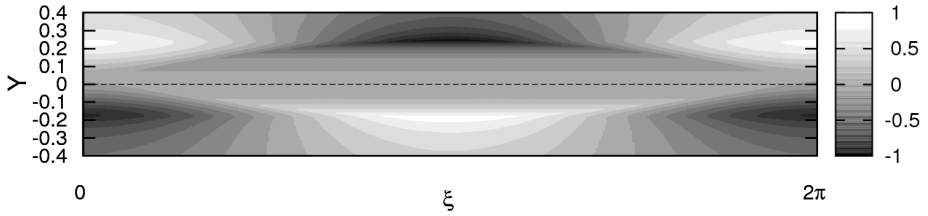

Figure 4.10: The asymptotic flow structure in the vicinity of the critical layer for $(\eta, \alpha) = (0.1, 0.6546)$. The grey scale represents contours of $\widetilde{\hat{U}}_{2Y}$.

First, from numerical computation of the Rayleigh equation (4.10) we find that there is a unique value $y_c = -0.9866$ at $(\eta, \alpha) = (0.1, 0.6546)$ for which A_0 in (5.53) is finite. It is therefore clear immediately from figure 4.1 (a) that the asymptotic theory is a better approximation to the lower-branch than the upper-branch. A close-up version of figure 4.1 (a) for the lower-branch at high R is shown in figure 4.9 (a), together with the corresponding asymptotic result. In the figure, we can see that the agreement between the numerical and asymptotic solutions is good once the kink at $R = 3.5 \times 10^7$ has been passed. In figure 4.9 (b) we compare the corresponding values of the momentum transfer Δ. Again, it can be seen that after the kink, the solution branch is approximated reasonably well by the asymptotic result.

Encouraged by the agreement obtained thus far, we now seek to compare the numerically and asymptotically determined flow structures. For this purpose, we make the comparisons for each layer using only the leading order asymptotic solutions as follows.

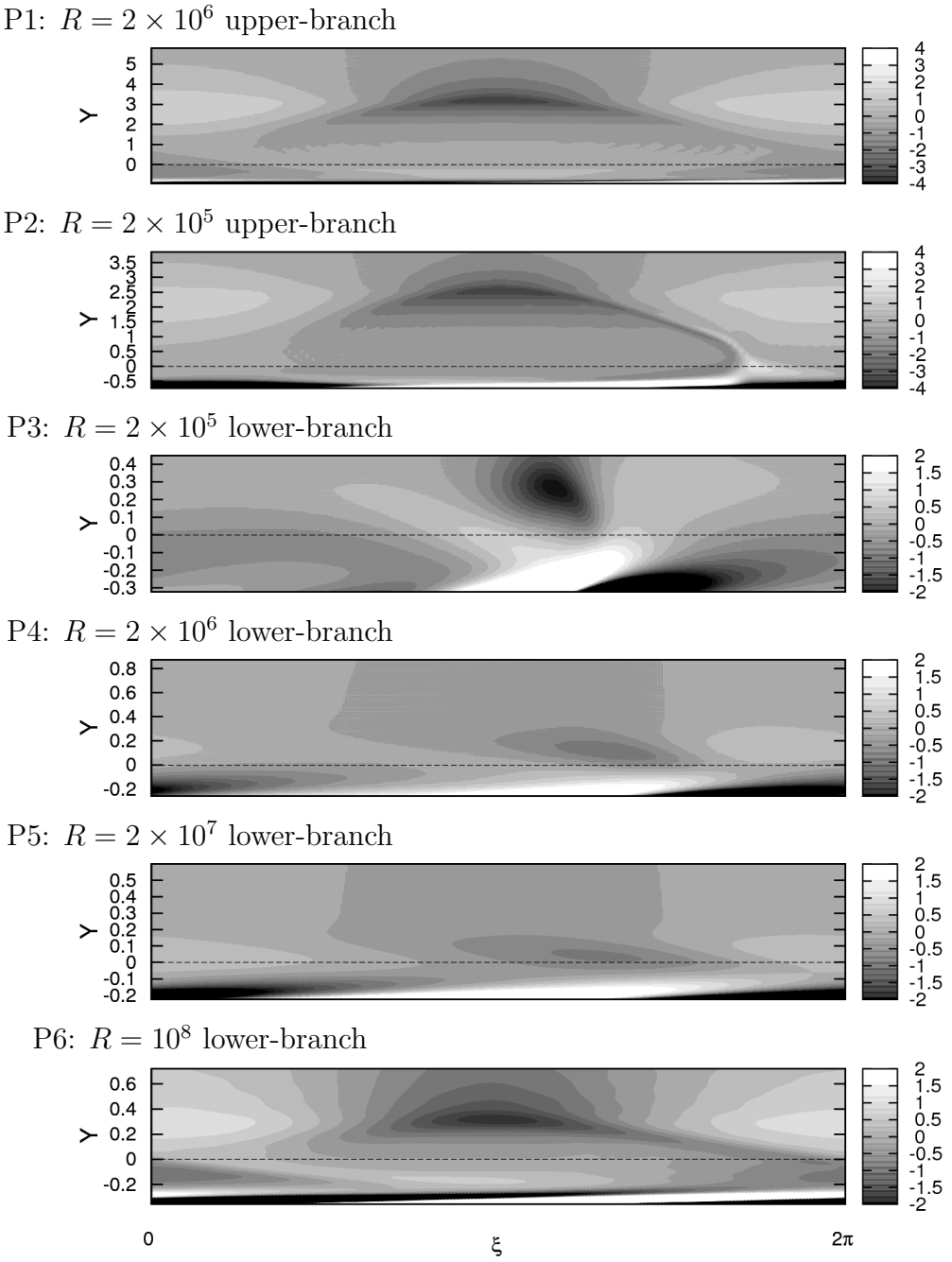

Figure 4.11: The flow structure the finite-amplitude solutions in the vicinity of the critical layer for $(\eta, \alpha) = (0.1, 0.6546)$. The grey scale represents contours of $\varepsilon^{-2}\tilde{u}_Y$. The radial plot intervals are the same as the close-up plots in figures 4.2 and 4.3.

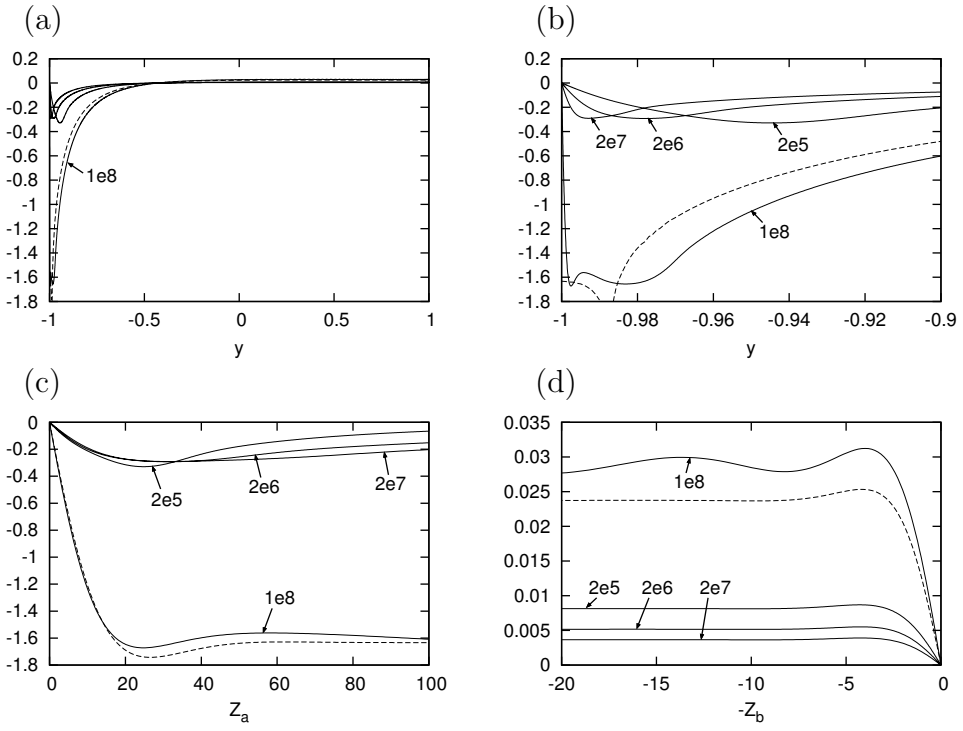

Figure 4.12: The comparison of the real part of the fluctuation F for the lower-branch finite-amplitude solutions (solid lines, $\varepsilon^{-2}F$) and the asymptotic results (dashed lines, A_0F_2 for (a) and (b), $\mathcal{F}_a$ for (c), $\mathcal{F}_b$ for (d)) for $(\eta, \alpha) = (0.1, 0.6546)$. The values of $R = \mathrm{A} \times 10^{\mathrm{N}}$ are abbreviated as AeN.

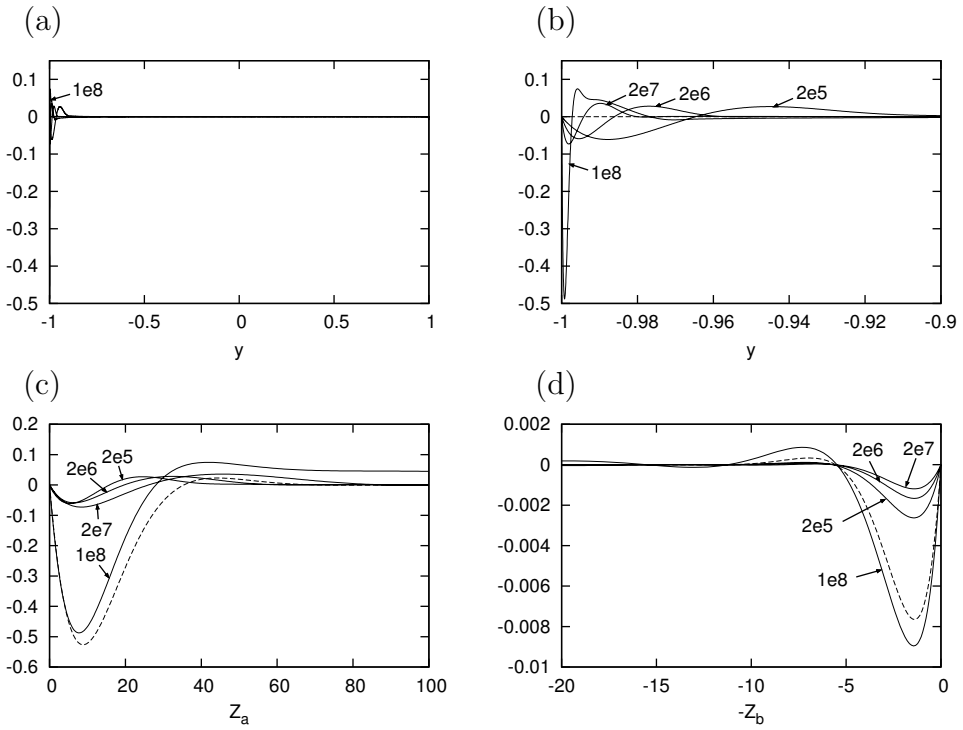

Figure 4.13: Caption as for figure 4.12 except that the imaginary parts are now compared.

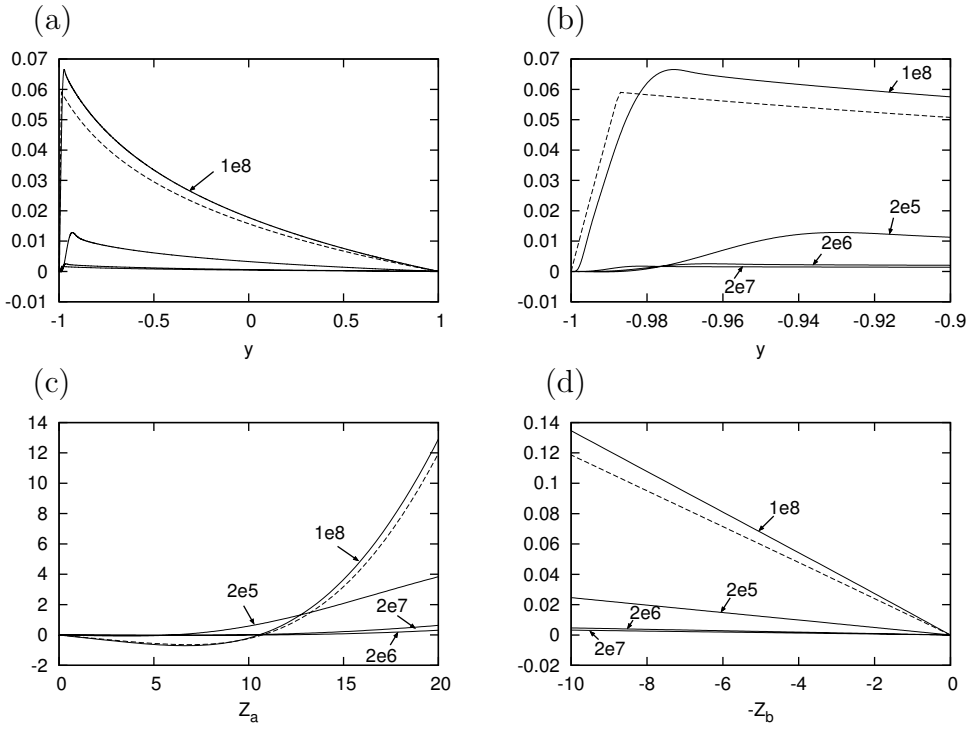

Figure 4.14: The comparison of the mean-flow distortion for the lower-branch finite-amplitude solutions (solid lines, $\varepsilon^{-1}\bar{u}$ for (a) and (b), $\varepsilon^{-4}\bar{u}$ for (c) and (d)) and the asymptotic results (dashed lines, $\bar{u}_1$ for (a) and (b), $\overline{U}_a$ for (c), $\overline{U}_b$ for (d)) for $(\eta, \alpha) = (0.1, 0.6546)$. The values of $R = \mathrm{A} \times 10^{\mathrm{N}}$ are abbreviated as AeN.

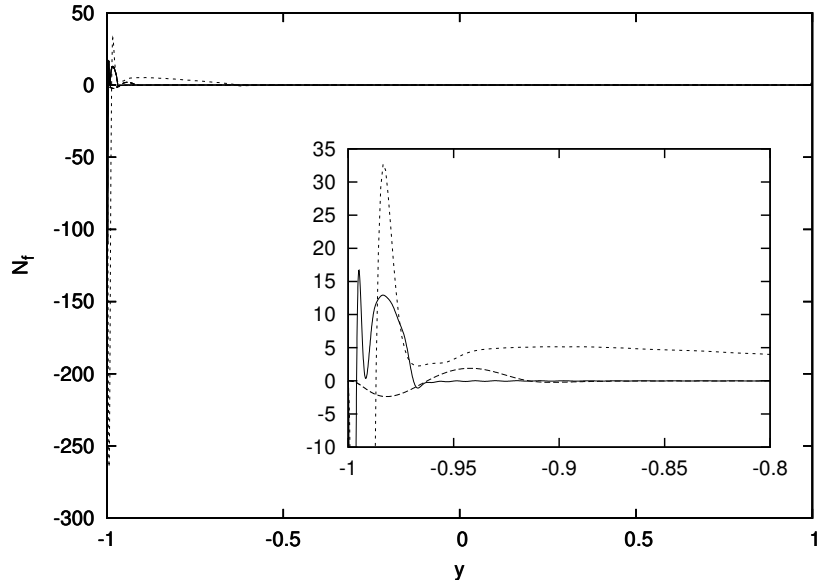

Figure 4.15: The nonlinear forcing of the mean-flow distortion for $(\eta, \alpha) = (0.1, 0.6546)$. The solid, dashed and dotted lines correspond to P6 ($R = 10^8$, lower- branch), P3 ($R = 2 \times 10^7$, lower-branch), P1 ($R = 2 \times 10^6$, upper-branch).

First we consider the nonlinear critical layer structure in terms of the stretched radial coordinate $Y = \varepsilon^{-1}(y - y_c)$. The asymptotic critical layer solution for the streamwise velocity has the expansion

$$u = \varepsilon \widehat{U}_1(Y) + \varepsilon^2 \ln \varepsilon \widehat{U}_{2L}(\xi) + \varepsilon^2 \{ \widetilde{\widehat{U}}_2(\xi, Y) + \overline{\widehat{U}}_2(Y) \} + \cdots , \tag{4.60}$$

where $\widehat{U}_2(\xi, Y)$ is numerically decomposed into the fluctuation $\widetilde{\widehat{U}}_2(\xi, Y)$ and the mean $\overline{\widehat{U}}_2(Y)$. For the sake of clarity, the fluctuation is differentiated with respect to Y, and the result is shown in figure 4.10. We compare this with the corresponding numerical result $\varepsilon^{-2}\tilde{u}_Y(\xi, Y)$ (figure 4.11). One of the characteristic structures associated with the asymptotic solution $\widetilde{\widehat{U}}_{2Y}$ is the cats-eye shape which possesses, at this order, a discontinuity in the first derivative at $Y - r_c \overline{u}_1(r_c)\tau_0^{-1} = \pm(2r_c\mu(1 - \cos\xi)/\alpha\tau_0)^{1/2}$. We can detect a similar quasi-discontinuous structure in the high R numerical solutions (P1 and P6). However, when R is smaller than its value at the kink, the discontinuity seems to be smoothed out due to the thicker nonlinear critical layer structure which effectively overlaps with the inner wall layer. For example, the visualization for P1 and P2 is similar at first glance, but there is only an upper (outer) discontinuity for P2 whereas we can see a lower (inner) discontinuity for P1. In other words the kink, which differentiates between the LR and HR modes, can be considered to be the product of the separation of the nonlinear critical layer and the inner wall layer structures. This feature is reminiscent of the role of kink investigated by Healey (1995) for the linear stability of the Blasius boundary layer, but seen in here in a nonlinear setting.

Next we compare asymptotic and numerical streamwise velocity solutions in the core and the wall layers, restricting our attention to the lower-branch numerical solution. The asymptotic core solution for the streamwise component expands in the form

$$u = \varepsilon \bar{u}_1(y) + \varepsilon^2 \{ A_0 F_2(y) \cos\xi + \bar{u}_2(y) \} + \cdots , \tag{4.61}$$

while the inner wall layer solution is written in terms of functions of $Z_a = R^{1/2}(1+y)$ as

$$u = \varepsilon^2\{\frac{1}{2}\mathcal{F}_a(Z_a)e^{\mathrm{i}\xi} + \text{c.c.}\} + \varepsilon^4\overline{\mathcal{U}}_a(Z_a) + \cdots, \tag{4.62}$$

and the outer wall layer solution is expressed in terms of the variable $Z_b = R^{1/2}(1-y)$ as

$$u = \varepsilon^2\{\frac{1}{2}\mathcal{F}_b(Z_b)e^{\mathrm{i}\xi} + \text{c.c.}\} + \varepsilon^4\overline{\mathcal{U}}_b(Z_b) + \cdots. \tag{4.63}$$

Therefore we see that the axial-dependence in the leading-order terms of the asymptotic solution in both the core and the wall layers consists of just a single harmonic. We recall that the numerical solution for the streamwise velocity takes the form

$$u = \bar{u}(y) + \{\frac{1}{2}F(y)e^{\mathrm{i}\xi} + \text{c.c.}\} + \text{higher order Fourier modes.} \tag{4.64}$$

The real and imaginary parts of $\varepsilon^{-2}F$ and A_0F_2, $\mathcal{F}_a, \mathcal{F}_b$ are compared in figures 4.12 and 4.13 respectively. Note that the real and imaginary parts of F correspond to the even ($\cos\xi$) and odd ($\sin\xi$) axial dependences respectively. In the outer part of the core, above the critical layer, both asymptotic and numerical solutions predict that F is even, to leading order. In the inner core, where the asymptotic theory again predicts an even streamwise velocity, such agreement is harder to obtain, in part due to the interaction of the nonlinear critical layer and inner wall layer referred to earlier. Except for this difference, the numerical solutions qualitatively agree with the asymptotic result. Furthermore, the solutions begin to show quantitative agreement after the kink is passed, as predicted in figure 4.9. The two peaks of F for $R = 10^8$ in figure 4.12 (b) also suggest that the separation of the inner wall layer and the nonlinear critical layer is underway.

The mean-flow distortion is also compared in figure 4.14. Since the leading order magnitude of the asymptotic solutions is different in each layer, we compare $\varepsilon^{-1}\bar{u}$ and $\bar{u}_1$ for the core region and $\varepsilon^{-4}\bar{u}$ and $\overline{\mathcal{U}}_a$, $\overline{\mathcal{U}}_b$ for the wall layers. Again, good qualitative and quantitative agreement of asymptotic and numerical solutions can be found before and after the kink. There are two prominent features close to the inner wall. One is the sharp peak, which is

related to the asymptotic discontinuity of the core solution at the critical layer. The other is the negative perturbation to the mean flow near the inner wall which arises in order to maintain the same value of momentum transfer Δ at the inner and outer walls (c.f. section 2.3). A plot of the normalized nonlinear forcing

$$N_f(y) \equiv (\alpha R) r^{-1} \partial_r \{ r \overline{\psi_\xi (\psi_r + r^{-1} \psi)} \} = -r^{-1} \partial_r (r \bar{u}'), \tag{4.65}$$

calculated from the numerical solution (figure 4.15), reveals that the mean-flow distortion is almost unforced in the outer core, as predicted by asymptotic theory.

4.3 The long-wave breakdown of the asymptotic structure

Here we focus on LR mode solutions which do not show quantitative agreement with the asymptotic analysis of section 4.2 due to the incomplete nature of the nonlinear critical layer structure (see, for example figure 4.11). One of the reasons that the limit of $\alpha \to 0$ is of interest is that numerical evidence suggests that the maximum value of η, $\eta_{\max}$ say, beyond which solutions do not exist, occurs at this limit.

From examination of figure 4.6, it appears that $\eta_{\max}$ tends to a maximum limiting value in the range 0.33–0.40 as $\alpha \to 0$. A more accurate estimate than this is difficult to obtain due to the high resolution required. In view of this, we choose to examine the behaviour as $\alpha \to 0$ by fixing $\eta = 0.33, R = 5 \times 10^4$. The fluctuation component of the streamwise velocity is visualized in figure 4.16 (a)–(c) for $\alpha = 0.05, 0.02$ and 0.01. These figures show an intriguing localization of the disturbance in the streamwise direction. To see the localization more clearly, the fluctuation field at the critical level $y = y_c$ is shown in figure 4.17 where we can see the concentration of both the axial and radial velocities in the localized region.

Due to the localization of the flow regime, there are small Gibbs oscillations in the stream-

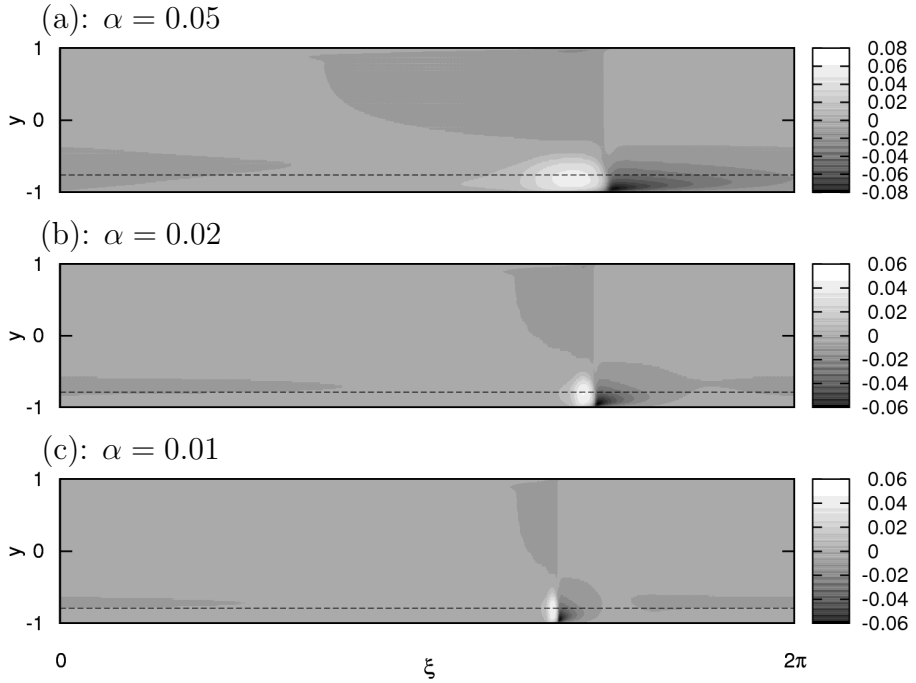

Figure 4.16: The axial fluctuation velocity field $\tilde{u}$ for $(\eta, R) = (0.33, 5\times10^4)$. The resolution $(L, N) = (50, 240)$ is used for (a) while $(L, N) = (30, 500)$ is used for (b) and (c). The dashed line represents the location of the critical layer.

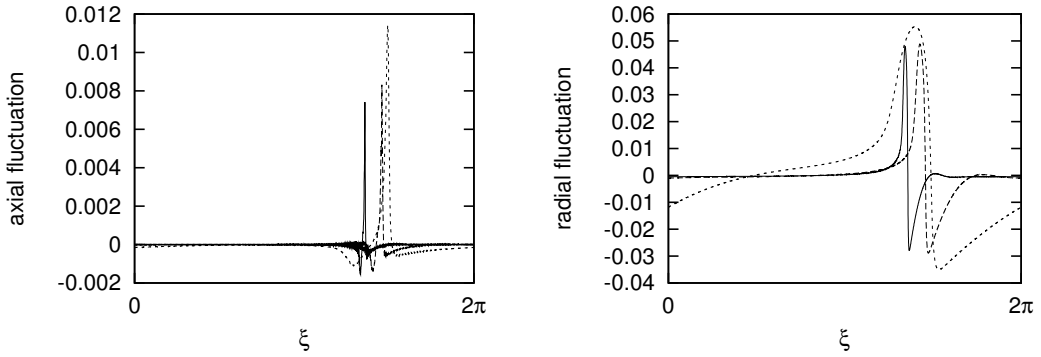

Figure 4.17: The fluctuation velocity field at the critical layer location $y = y_c$ for $(\eta, R) = (0.33, 5 \times 10^4)$. Left/right figure represents $\tilde{u}/\tilde{v}$. The solid, dashed and dotted curves correspond to $\alpha = 0.01, 0.02$ and 0.05 respectively. The truncation level is same as figure 4.16.

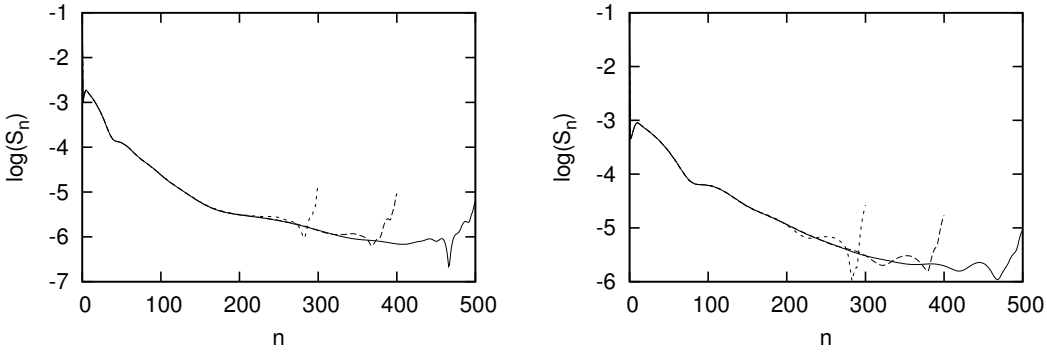

Figure 4.18: The spectral intensity $S_n = \left|\overline{ue^{-in\xi}}\right| |_{y=y_c}$ for various N. The parameters are same as figure 4.16. The radial truncation is fixed to $L = 30$. Left: $\alpha = 0.02$, Right: $\alpha = 0.01$. Solid, dashed and dotted curve represents the result of $N = 500$, $N = 400$ and $N = 300$ respectively.

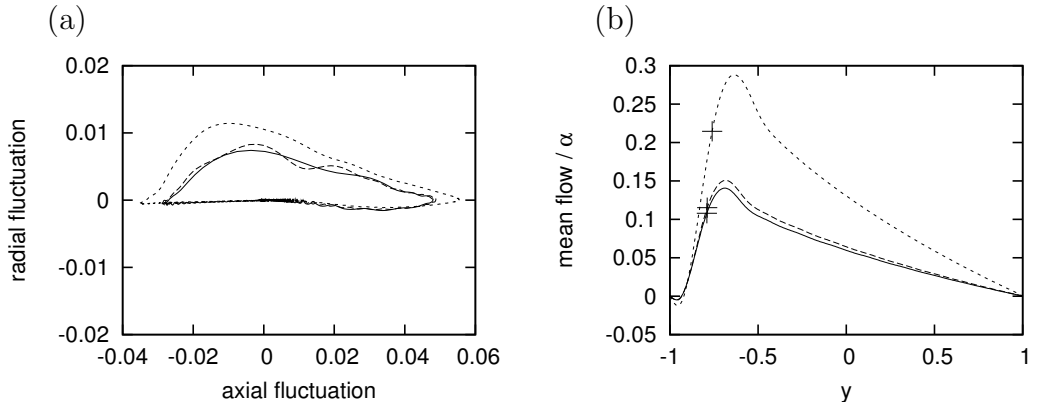

Figure 4.19: The convergence of the flow field as the wavenumber is decreased for $(\eta, R) = (0.33, 5 \times 10^4)$. The truncation level is the same as figure 4.16. (a): Plot of flow field along the axis in the phase space spanned by $\tilde{u}$ and $\tilde{v}$ for $\xi \in [0, 2\pi]$ at the critical layer location $y = y_c$. (b): The normalized mean flow $\bar{u}/\alpha$. The solid, dashed and dotted curves correspond to $\alpha = 0.01, 0.02$ and 0.05 respectively. The crosses indicate the critical layer locations.

wise direction. Hence to check reliability of solutions, we exhibit spatial resolution test in figure 4.18 by examining spectral intensity of streamwise disturbance at the critical layer location. From the figure, we can find the spectral coefficients decay rapidly with little change in the leading order intensities as streamwise resolution, N, is increased. The slightly upraised tail corresponds to Gibbs oscillations and we conclude these are artificial one because of their sensitivity to the resolution.

The smaller the value of α, the stronger the localization becomes and it appears that the shape of the fluctuation is converging to a limiting form as $\alpha \to 0$. Indeed, it is possible to obtain $\alpha = 0.02$ solution by Newton's method starting from superimposed two $\alpha = 0.01$ solutions so that the resultant peaks are evenly placed. To show this tendency more clearly, the plots of $\tilde{u}$ and $\tilde{v}$ are combined in figure 4.19 (a). The mean-flow distortion for the different values of α is compared in figure 4.19 (b) and we see that this quantity scales with α when α is small. This makes sense because the mean-flow distortion is sustained by the spatial average of the nonlinear self-interaction of the fluctuation (see (2.10)) and therefore if the shape of the fluctuation is becoming independent of α, the mean-flow distortion divided by α must converge to a limiting form. However when α is sufficiently small, specifically of $O(R^{-1})$, the solution cannot continue to exist in its present form at finite R as it would violate the criteria of energy analysis, which, for $\eta = 0.33$, shows that all disturbances must monotonically decay if $\alpha R \lesssim 108.20$ (see Appendix 4.A.2). Another feature of flow fields in figure 4.19 is multi-layered asymptotic structure is no more visible. To see why the asymptotic structure in the previous section fails in long-wave situation, consider the thickness of the critical layer. From expression (4.58) we observe that $A_0 \sim O(\alpha^{-1/3})$ as $\alpha \to 0$, which in turn means that from (4.43), the parameter $\mu \sim O(\alpha^{2/3})$. It follows that the critical-layer variable $Y \sim O(\mu/\alpha)^{1/2} \sim O(\alpha^{-1/6})$, from (4.46). Thus, in the long-wave limit, the critical-layer thickness $\sim O(\varepsilon Y) \sim O(\alpha R)^{-1/6}$, in view of (4.49). Turning to the viscous wall layers, the thickness of the layer on the inner cylinder is $O(R^{-1/2}\mu_a^{-1}) \sim O(\alpha R)^{-1/2}$, using expressions (4.27) and (4.29). A similar argument leads to the same order estimate for the thickness of the boundary-layer on the outer cylinder. Eventually, when α is sufficiently small, the thicknesses of the critical layer

and wall layers become comparable. In this new structure the wall layers and critical layer have grown and merged to fill the whole of the annulus.

4.4 Summary

In the nonlinear analysis presented here, we obtained finite-amplitude axisymmetric solutions travelling downstream. The initial computation of the axisymmetric solutions was conducted at a radius ratio $\eta = 0.1$, where we can find linear instability, and we fixed the wavenumber α at its linear critical value of 0.6546. There are two linear critical points for this particular wavenumber, and we detect two solution branches that bifurcate subcritically. The solution branch bifurcating from the smaller critical R has a turning point at $R = O(10^4)$. In other words, the resultant solution branch comes into existence with increasing R due to this saddle-node bifurcation, and the upper- and lower-branch solutions, which coincides with the linear solution for finite range of R, are formed in the R–amplitude space. At sufficiently high R, our calculations indicated that there exist kinks in both the upper- and lower-branches. The part of each branch before and after the kink is refereed to as LR (low Reynolds number) and HR (high Reynolds number) mode respectively.

A multi-structured analytic solution valid for asymptotically large R was derived in section 4.2: this asymptotic theory divides the shear layer into five decks (figure 4.7). At a leading order viscosity is only present in the boundary layers near the inner and outer walls and is also vital in the nonlinear critical layer where a cats-eye shape quasi-singularity exists and the mean flow is strongly modified. The asymptotic theory was then compared with the finite Reynolds number calculations.

For the LR mode, where R is in the range $O(10^4)$–$O(10^7)$, we observed good qualitative agreement between the asymptotic solutions for the various layers and the corresponding visualization of the numerical solutions. However, for this mode, the inner inviscid core layer is absent and hence the nonlinear critical layer structure is incomplete, due to the effective interaction with the inner wall layer. The reason for this is that the distance

between the nonlinear critical layer and the inner wall layer is so close that it is comparable with the thickness of the critical layer, which is of order $R^{-1/6}$ according to the theory. When we further increase R to 10^8, so that the relevant solution branch belongs to the HR mode, we find that the flow visualization of the lower-branch solution agrees quantitatively with the asymptotic solution, with visualizations showing a clear separation of the inner wall layer and the critical layer. Therefore we conclude that the kink in the solution branch results from the separation of the inner wall layer and the nonlinear critical layer. In the linear setting, Healey (1995) came to a similar conclusion when considering boundary-layer stability.

We also examined how the finite-amplitude solution branch behaved as η is varied. It is found that the solution branches of both the HR and LR mode can be continued well beyond the linear long-wave cut-off value of $\eta \simeq 0.1415$. For the LR mode, the nonlinear cut-off value of η increases as α decreases. The ultimate value for small α is estimated to lie between 0.33 and 0.40. This observation suggests that the nonlinear version of the cut-off is also a long-wave phenomenon. Although the present calculation failed to trace the HR mode solution branch beyond a value of $\eta \simeq 0.159$, it must also reach a cut-off if we assume that this mode asymptotes according to the large R theory which must itself experience a cut-off before the narrow gap limit of PCF is reached.

The viscous layers in the asymptotic structure become thinner as R is increased, but thicken as α is decreased. A distinguished limit $\alpha \sim O(R^{-1})$ arises at which the wall layers and the critical layer thicken to an $O(1)$ size and merge together. An identical effect is observed in the numerical solutions where we observe that as α is decreased to 0.01 for $\eta = 0.33$, the rapidly varying behaviour near the critical layer location is completely smoothed out. Instead, there is the formation of a prominent streamwise localized structure.

4.A Appendix

4.A.1 The phase shift calculation for the asymptotic solution

Here our aim is to calculate the jump in the $\sin\xi$ component of axial velocity across the critical layer considered in section 5.3. It is shown there that the term $\widehat{U}_5(\xi, Y)$ in (4.40) is the largest to possess an odd part about $\xi = \pi$. We therefore write

$$\widehat{U}_5 = \widehat{U}_{5\mathrm{O}} + \widehat{U}_{5\mathrm{E}},$$

with subscripts O and E to denote the odd and even parts of this expression, and we do likewise for the corresponding radial velocity and pressure components. From substitution of (4.40) into the Navier-Stokes equations (4.4−4.4), we find that $(\widehat{U}_{5\mathrm{O}}, \widehat{V}_{5\mathrm{E}}, \widehat{P}_{5\mathrm{O}})$ are governed by

$$\begin{aligned} \alpha\widehat{U}_{5\mathrm{O}\xi} + \widehat{V}_{5\mathrm{E}Y} &= 0, \\ \alpha\widehat{U}_1\widehat{U}_{5\mathrm{O}\xi} + \widehat{V}_1\widehat{U}_{5\mathrm{O}Y} + \widehat{V}_{5\mathrm{E}}\widehat{U}_{1Y} &= -\alpha\widehat{P}_{5\mathrm{O}\xi} + \widehat{U}_{2YY} + \widehat{U}_{1Y}/r_c. \end{aligned}$$

If we differentiate the second of these equations with respect to Y, use expressions (4.41), (4.47) for the velocity components, and change to the characteristic variable ζ defined in (4.46), we can simplify this system to

$$\frac{\partial}{\partial\widehat{\xi}}(\widehat{U}_{5\mathrm{O}Y}) = \mp\left(\frac{2\alpha\tau_0}{r_c}\right)^{1/2}\frac{\partial}{\partial\zeta}\left((\zeta - \mu\cos\xi)^{1/2}\kappa'(\zeta)\right), \tag{4.66}$$

where $\kappa(\zeta)$ is given by (4.50), and $\partial/\partial\widehat{\xi}$ denotes differentiation with respect to ξ, holding ζ fixed.

To determine the velocity jump we write

$$\widehat{U}_{5\mathrm{O}} = \sum_{n=1}^{\infty} b_n(Y)\sin n\xi,$$

so that the quantity φ defined in (4.16) is given by

$$\varphi = \lim_{Y\to\infty} b_1 - \lim_{Y\to-\infty} b_1,$$

where

$$b_1(Y) = \frac{1}{\pi}\int_0^{2\pi} \widehat{U}_{5\mathrm{O}}(\xi, Y)\sin\xi\, d\xi.$$

By changing variables from (ξ, Y) to $(\widehat{\xi}, \zeta)$, where $\xi = \widehat{\xi}$, integrating by parts with respect to $\widehat{\xi}$, and using (4.66), we finally obtain

$$b_1 = \frac{2}{\mu}(2\zeta\kappa' - \kappa) + \text{constant}.$$

Then, using the properties of κ given in (4.48), (4.50), (4.51) and (4.52), we can establish that

$$\varphi = \frac{2\tau_0 C_1}{\alpha r_c^2 A_0^{1/2}},$$

which is the result (4.57) quoted in the main text.

4.A.2 Energy analysis

Here we employ standard techniques of energy analysis (e.g. see Joseph & Carmi 1969 and Joseph 1976) to compute an energy Reynolds number R_E for axisymmetric SCF. This is a value of Reynolds number below which it is guaranteed that all disturbances to the basic flow decay monotonically in time, and it therefore represents a lower bound on R, below which finite-amplitude travelling waves cannot exist. Often, of course, this bound proves to be extremely pessimistic in practice; however it still provides a useful partial check on the validity of the travelling-wave solutions discussed in this paper and reduces the parameter space that needs to be investigated.

We begin by defining the kinetic energy of the disturbance flow as

$$E \equiv \frac{1}{2}\langle u^2 + v^2\rangle,$$

where the volumetric integrating operator takes the form

$$\langle\cdot\rangle \equiv \int_0^{2\pi/\alpha}\int_{r_a}^{r_b} \cdot\, r\, dr\, dx.$$

The development of the energy can be found by considering $\langle u(4.2) + v(4.4)\rangle$. This leads to the exact result

$$\frac{dE}{dt} = \frac{I_D}{R}(m-1),$$

where

$$I_D \equiv \langle |\nabla u|^2 + |\nabla v|^2 + r^{-2}v^2\rangle \geq 0,\;\; m \equiv R\frac{I_A}{I_D},\;\; I_A \equiv -\langle uv/\ln\eta^r\rangle.$$

It follows that we need $\grave{m} = \max_{\mathbf{u}} m > 1$ in order for the system to experience some energy growth. Suppose that the solution which realizes $\grave{m}$ is $[\grave{u}, \grave{v}]$. We then consider all solutions in the form $[u, v] = [\grave{u}, \grave{v}] + \delta[\acute{u}, \acute{v}]$. By definition, $\grave{m} = m|_{\delta=0}$ and $\frac{\partial m}{\partial \delta}\big|_{\delta=0}$. Using these relations and the definition of m, we obtain

$$\grave{m}\left.\frac{\partial I_D}{\partial\delta}\right|_{\delta=0} - R\left.\frac{\partial I_A}{\partial\delta}\right|_{\delta=0} = \langle \acute{\mathbf{u}}\cdot\mathbf{\Phi}\rangle = 0 \tag{4.67}$$

where

$$\mathbf{\Phi} = (-2\grave{m}\nabla^2\grave{u} + R\grave{v}/r\ln\eta)\mathbf{e}_x + (-2\grave{m}(\nabla^2\grave{v} - r^{-2}\grave{v}) + R\grave{u}/\ln\eta^r)\mathbf{e}_r.$$

Since equation (4.67) is satisfied for arbitrary $\acute{\mathbf{u}}$, $\mathbf{\Phi}$ must have a scalar potential ϱ. By introducing a stream function ϕ such that $[\grave{u}, \grave{v}] = [\phi_r + r^{-1}\phi, -\phi_x]$ and eliminating the potential ϱ by combining the axial and radial equations of $\nabla\varrho = \mathbf{\Phi}$, we find that ϕ satisfies

$$\begin{gathered}\phi_{xxxx} + 2\phi_{xxrr} + 2r^{-1}\phi_{xxr} - 2r^{-2}\phi_{xx}\\ +\phi_{rrrr} + 2r^{-1}\phi_{rrr} - 3r^{-2}\phi_{rr} + 3r^{-3}\phi_r - 3r^{-4}\phi =\\ \frac{R}{2\grave{m}}\partial_x(-2\phi_r/\ln\eta^r),\end{gathered} \tag{4.68}$$

together with $\phi = \phi_r = 0$ at $r = r_a$ and $r = r_b$. The solution can be taken to be proportional to $e^{\mathrm{i}\alpha x}$ because equation (4.68) is linear. As a consequence, we can solve this equation numerically by expanding ϕ in terms of lth Chebyshev polynomial of first kind

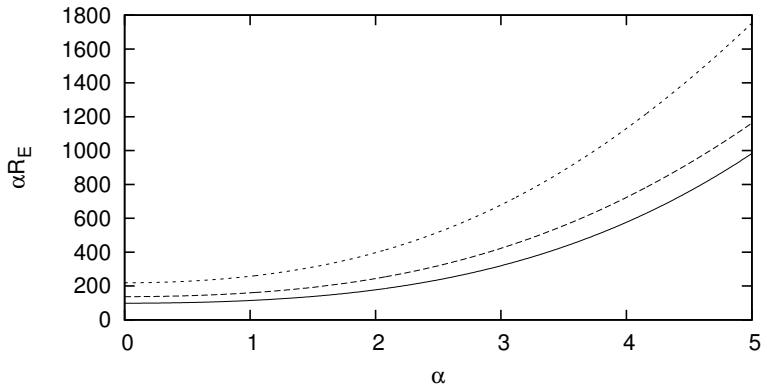

Figure 4.20: The energy Reynolds number R_E for axisymmetric disturbances. The solid, dashed and dotted lines are calculated for $\eta = 1, 0.1$ and 0.01 respectively.

$T_l(y)$ as

$$\phi(x,y) = \sum_{l=0}^{L} (1-y^2)^2 T_l(y) e^{\mathrm{i}\alpha x}$$

and evaluating (4.68) at the collocation points (2.20). The resultant algebraic eigenvalue problem

$$A_{l_0 l} X_l = \sigma B_{l_0 l} X_l$$

leads to $L+1$ eigenvalues $\sigma \equiv \alpha R/\dot{m}$. The minimum value of positive purely real σ gives αR_E where R_E is the energy Reynolds number. There are no finite-amplitude solutions if $R < R_E$, because all disturbances monotonically decay.

The results of numerical computations are shown in figure 4.20. We investigated the range $0.01 \leq \eta \leq 1$ and found that αR_E increases with decreasing η. Note that (4.68) reduces to its planar counterpart in the narrow-gap limit $\eta \to 1$. Because $\sigma(\alpha, \eta) = \sigma(-\alpha, \eta)$, αR_E must have a local extremal value at $\alpha = 0$. From the figure, we can see that this point is a global minimum for the current range of η. However, we note that the minimum of R_E is at a non-zero value of α, e.g. for $\eta = 0.1$, the minimum $R_E = 122$ occurs at $\alpha = 1.96$.

The axisymmetric finite-amplitude solutions found in section 4.1 have $\alpha = O(1)$ and exist over a range of $R = O(10^4)$, comfortably in excess of the energy Reynolds numbers calculated here.

Chapter 5

Non-axisymmetric solutions

It is likely that the laminar SCF can be destabilized in experiments at Reynolds numbers far below the values we saw in the linear and nonlinear analyses with respect to axisymmetric disturbances. Therefore, in this chapter we attempt to find other types of nonlinear solutions at relatively low Reynolds numbers. It is possible that these types of solutions have some connection with nonlinear solutions in PCF since the narrow-gap limit of SCF corresponds to PCF. With reference to the analysis of chapters 3 and 4 there are no linear and nonlinear two-dimensional instabilities in PCF. Yet, finite-amplitude three-dimensional streamwise roll type solutions as a result of the saddle-node bifurcation at $R = O(10^2)$ exist (Nagata 1990). Thus it is natural to anticipate that the three-dimensional solutions of PCF as our narrow gap limit ($\eta \to 1$) still exist in wider gap cases ($\eta < 1$).

5.1 Homotopy from the Nagata solution in plane Couette flow

In this section, we will consider a homotopy between the planer geometry of PCF and the cylindrical geometry of SCF. Therefore, first we need to construct a transformation between the Cartesian and cylindrical coordinates used in these systems. Note that the

(l,m,n)	$X^{(1)}_{lmn}$: $\eta = 0.9999$	$X^{(1)}_{lmn}$: $\eta = 1$
(0, 1,1)	(-0.531545990, 0.000342705)	(-0.531546101, 0.000000000)
(0, 1,2)	(0.015296839,-0.000020938)	(0.015296853, 0.000000000)
(0, 2,1)	(-0.000003429,-0.000523607)	(0.000000000,-0.000523609)
(0, 2,2)	(0.000000662, 0.000539484)	(0.000000000, 0.000539484)
(1, 1,1)	(0.000247443, 0.381802584)	(0.000000000, 0.381802665)
(1, 1,2)	(0.000015775, 0.013213093)	(0.000000000, 0.013213102)
(1, 2,1)	(-0.077862389, 0.000048121)	(-0.077862404, 0.000000000)
(1, 2,2)	(0.004590099,-0.000005700)	(0.004590102, 0.000000000)
(0,-1,1)	(0.531545990,-0.000342705)	(0.531546101, 0.000000000)
(0,-1,2)	(0.015296839,-0.000020938)	(0.015296853, 0.000000000)
(0,-2,1)	(0.000003429, 0.000523607)	(0.000000000, 0.000523609)
(0,-2,2)	(0.000000662, 0.000539484)	(0.000000000, 0.000539484)
(1,-1,1)	(-0.000247443,-0.381802584)	(0.000000000,-0.381802665)
(1,-1,2)	(0.000015775, 0.013213093)	(0.000000000, 0.013213102)
(1,-2,1)	(0.077862389,-0.000048121)	(0.077862404, 0.000000000)
(1,-2,2)	(0.004590099,-0.000005700)	(0.004590102, 0.000000000)

Table 5.1: The comparison of the leading amplitude coefficients of the narrow gap SCF for $\eta = 0.9999$ at $(\alpha, m_0) = (0.75, 31168)$ and the corresponding coefficients of PCF $(\alpha, \beta) = (0.75, 1.5585)$. $R = 400$. The lower-branch solution. $(L, M, N) = (20, 6, 4)$.

cylindrical coordinate system becomes singular in the narrow-gap limit because $r_m \to \infty$ in the limit as $\eta \to 1$. Thus we introduce new variables: distance along the mean radius $z = r_m\theta$, wavenumber $\beta = m_0/r_m$ and wavespeed $c_z = r_m c_\theta$, replacing θ, m_0 and c_θ. With the new coordinate system (x, y, z), all of the governing equations smoothly reduce to their planar counter part in the narrow gap limit $\eta \to 1$. In the case of $\eta < 1$, non-integer values of m_0 do not cause any mathematical and computational difficulties although physically we must have $m_0 \in \mathbb{Z}$ due to the azimuthal 2π periodicity. The new wavenumber β and wavespeed c_z coincide with the usual spanwise wavenumber and wavespeed respectively at $\eta = 1$ (note that x, y and z represent streamwise, wall-normal and spanwise directions respectively though the system becomes a left-handed system).

The basic flow (2.5) becomes the plane Couette profile

$$U_B(y) = R(1 - y)/2 \tag{5.1}$$

in the narrow-gap limit. The phase lock conditions we adopt for three-dimensional solutions

	Upper				Lower			
(L, M, N)	Δ	c/R	$\|L_i\|_2$	$\|F_i\|_2$	Δ	c/R	$\|L_i\|_2$	$\|F_i\|_2$
(16, 8, 9)	2.15290	0.49908	1.4e5	3.2e-8	1.54290	0.44516	2.9e4	2.0e-7
(24, 8, 9)	2.15328	0.49907	1.7e5	8.5e-7	1.54282	0.44515	3.5e4	1.2e-8
(16,12, 9)	2.15046	0.49976	1.4e5	2.7e-8	1.54277	0.44514	2.9e4	1.4e-9
(16, 8,14)	2.15323	0.49880	1.4e5	7.7e-5	1.54290	0.44516	2.9e4	1.7e-9

Table 5.2: The momentum transfer Δ, the wavespeed c and the L_2-norms $\|L_i\|_2$ and $\|F_i\|_2$ at different truncation levels (L, M, N) for the non-axisymmetric solution at $(\eta, \alpha, m_0, R) = (0.5, 0.51, 3, 350)$.

are $\Im(X^{(1)}_{120}) = 0$ and $\Im(X^{(1)}_{102}) = 0$.

First, in order to obtain the solution in cylindrical geometry, we consider the case of $\eta = 0.9999$ ($r_m = 19999, m_0 = 31168$ so that $\beta = 1.5585$ for PCF) and use the steady three-dimensional PCF solution with $(\alpha, \beta) = (0.75, 1.5585)$ by Nagata (1990) as the initial guess for the Newton-Raphson iterations. The iterations successfully converge and the leading amplitude coefficients for the potentials of the converged solution at $\eta = 0.9999$ are compared with the corresponding coefficients of the PCF solution at $R = 400$ in table 5.1. The solution in the cylindrical coordinates inherits some features of the PCF solution: we can see from table 5.1 that

$$X^{(1)}_{lmn} = -X^{(1)}_{l-mn} \qquad \text{if} \qquad n \in \text{odd integers},$$
$$X^{(1)}_{lmn} = X^{(1)}_{l-mn} \qquad \text{if} \qquad n \in \text{even integers}.$$

We also verified that (not listed in table 5.1)

$$X^{(2)}_{lmn} = X^{(2)}_{l-mn} \qquad \text{if} \qquad n \in \text{odd integers},$$
$$X^{(2)}_{lmn} = -X^{(2)}_{l-mn} \qquad \text{if} \qquad n \in \text{even integers}.$$

These relations imply the shift-reflection symmetry

$$\text{(i)} : [u, v, w](\xi, y, \zeta) = [u, v, -w](\xi + \pi, y, -\zeta), \tag{5.2}$$

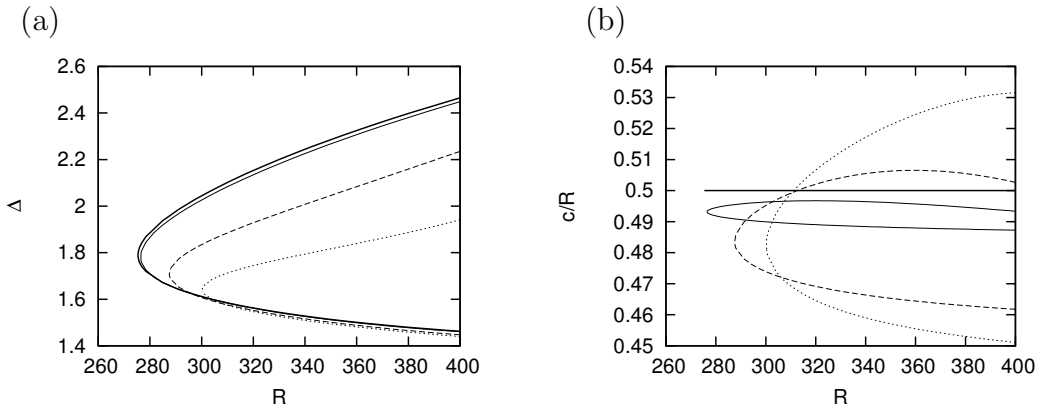

Figure 5.1: The saddle-node bifurcations of non-axisymmetric travelling-wave solutions for $(\alpha, \beta) = (0.75, 1.5585)$. The nonlinear measures are (a): the momentum transfer Δ on the inner cylinder and (b): the axial wavespeed c. Thick solid, thin solid, dashed and dotted curves indicate the cases for $\eta = 1, 0.8, 0.5$ and 0.4, respectively.

are possessed by both of these PCF and SCF solutions. It is known that the nonlinear PCF solution also possesses the shift-rotation symmetry

$$\text{(ii)} : [u, v, w](\xi, y, \zeta) = [-u, -v, w](-\xi + \pi, -y, \zeta + \pi). \tag{5.3}$$

This symmetry (ii) is obviously absent in SCF solutions because the reflection about the mean radius $y = 0$ corresponding to $r = r_m$ is broken due to the curvature in the cylindrical coordinates. The symmetry (ii) in PCF solutions is represented by

$$\Im(X^{(1)}_{lmn}) = \Im(X^{(2)}_{lmn}) = 0 \qquad \text{if} \qquad l + m \in \text{odd integers},$$
$$\Re(X^{(1)}_{lmn}) = \Re(X^{(2)}_{lmn}) = 0 \qquad \text{if} \qquad l + m \in \text{even integers}$$

which is not satisfied in SCF as can be verified in table 5.1. So, for SCF with $\eta < 1$ the nonlinear solution possesses only the shift-refection symmetry (i). Furthermore the present SCF solution does not possess any other symmetries other than (i); see a more detailed discussion in subsection 5.2.2. Once the solution for $\eta = 0.9999$ with $(\alpha, \beta) = (0.75, 1.5585)$ is obtained, solutions for wider gap cases are sought by continuation. Changing η implies that, according to $m_0 = \frac{1+\eta}{1-\eta}\beta$, m_0 does not necessarily take an integer value for fixed β. In order for the continuation to be smooth we allow m_0 to take a real number at the first stage (since we now fix the gap, it is reasonable to fix azimuthal fundamental periodicity

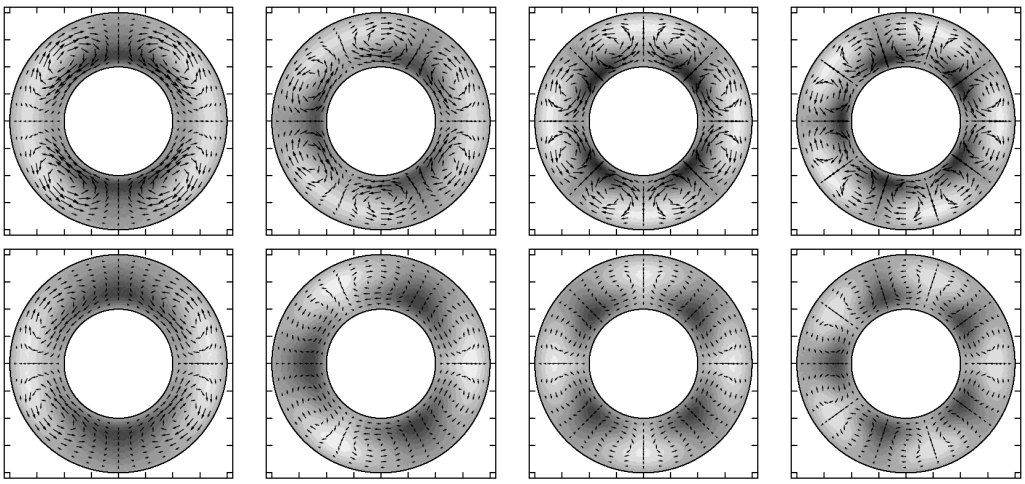

Figure 5.2: The axially averaged disturbance flow patterns for $(m_0, \alpha) = (2, 0.33)$, $(3, 0.51)$, $(4, 0.71)$, $(5, 0.90)$ (from left to right). $R = 350$ and $\eta = 0.5$. The top/bottom four figures correspond to the upper/lower-branch solutions. The grey scale represents the axial velocity component relative to the laminar state (light: fast, dark: slow).

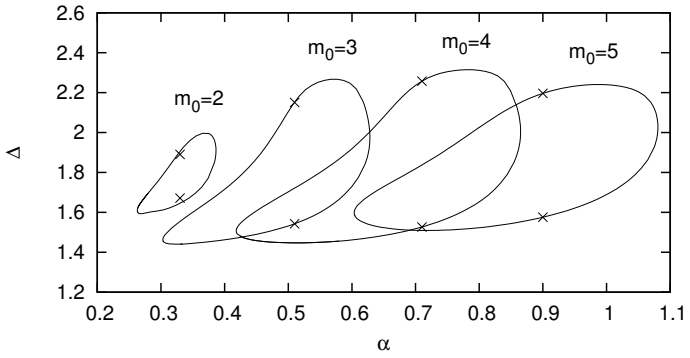

Figure 5.3: The existence region of the travelling-wave solutions for $m_0 = 2, 3, 4, 5$ at $R = 350$ for $\eta = 0.5$. The truncation level $(L, M, N) = (16, 8, 9)$ is used to draw the curve. Crosses indicate the result with higher truncation level $(L, M, N) = (20, 12, 12)$.

in terms of length keeping β). In the next stage, 2π-periodic solutions are sought for each η by changing β gradually so that m_0 becomes an integer.

Figure 5.1(a) shows the momentum transfer Δ of the solutions for $\eta = 0.8, 0.5$ and 0.4 with $(\alpha, \beta) = (0.75, 1.5585)$. With these wavenumbers, it is observed that the saddle-node points shift slightly toward larger values of R as η is decreased. We see from figure 5.1(b) that the wavespeed c in the axial direction for these cases are non-zero in general. The solutions of PCF are steady when the two boundaries are moving in the opposite directions with the same speed. Here, since the outer cylinder is stationary the wavespeeds c of both the upper- and lower-branch solutions for $\eta = 1$ are equal to half the speed of the inner cylinder. For

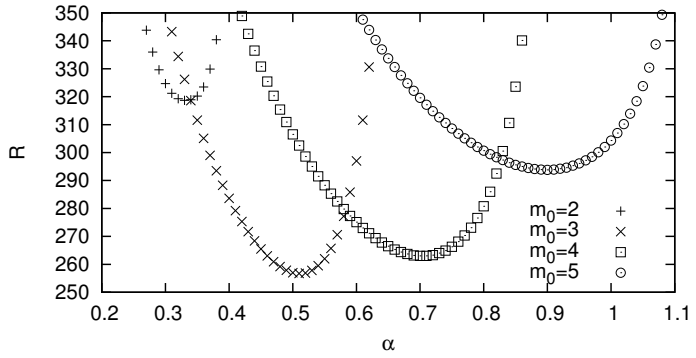

Figure 5.4: The Reynolds number near the saddle-node bifurcation point for the travelling-wave solutions with the wavenumber pairs (m_0, α) for $\eta = 0.5$.

wide gap cases, the wavespeed c of the upper-branch solution is faster than that of the lower-branch solution. Consistent with the shift-reflection symmetry (i), our calculation showed the wavespeed c_θ and the mean flow W in the azimuthal direction are always zero. As described above, we change β gradually to obtain non-axisymmetric travelling-wave solutions of SCF with $m_0 = 2, 3, 4, 5$ for $\eta = 0.5$. Table 5.2 shows the accuracy of a typical solution at various truncation levels. We see that $(L, M, N) = (16, 8, 9)$ gives sufficiently accurate solutions and we therefore adopt this truncation level for the calculations in this section unless stated otherwise. Figure 5.2 shows the axially averaged disturbance flow patterns for these solutions. Note that the patterns are still dependent on θ. It can be seen that for all the cases the region where the axial velocity is faster than the basic flow is located near the outer cylinder, whereas the region where the axial velocity slower than the base flow is located near the inner cylinder.

Figure 5.3 shows the existence region of the travelling-wave solutions with $m_0 = 2, 3, 4, 5$ with respect to the axial wavenumber α at $R = 350$. For other azimuthal wavenumbers, $m_0 = 1, 6$ and above, non-axisymmetric travelling-wave solutions appear at higher Reynolds numbers, and so their existence regions are not captured in figure 5.3. The solution family is created in a saddle-node bifurcation for each wavenumber pair (m_0, α) as shown in figure 5.4. From the figure we see that the lowest Reynolds number at the saddle-node bifurcations takes place at 256.6 with $(m_0, \alpha) = (3, 0.51)$.

The axial mean-flow profiles $\overline{U}$ of the travelling-wave solution with the 'optimum wavenum-

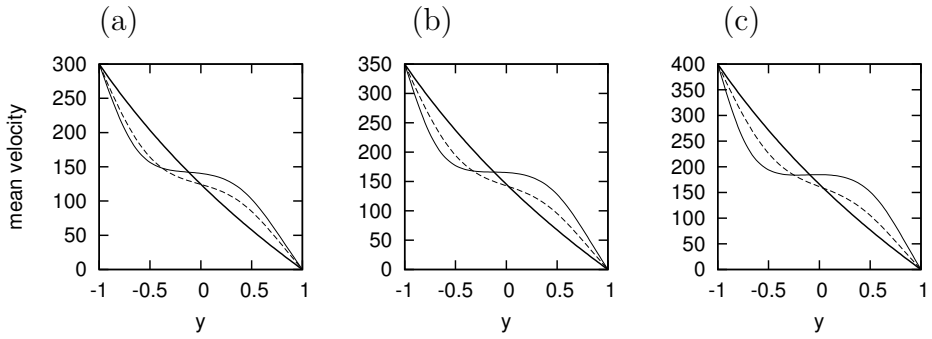

Figure 5.5: The axial mean-flow profile $\overline{U}$ for $(\eta, m_0, \alpha) = (0.5, 3, 0.51)$. (a): $R = 300$, (b): $R = 350$, (c): $R = 400$. Thin solid and dashed curves indicate the mean flows for the upper- and lower-branch solutions, respectively. Thick curves correspond to the base flow.

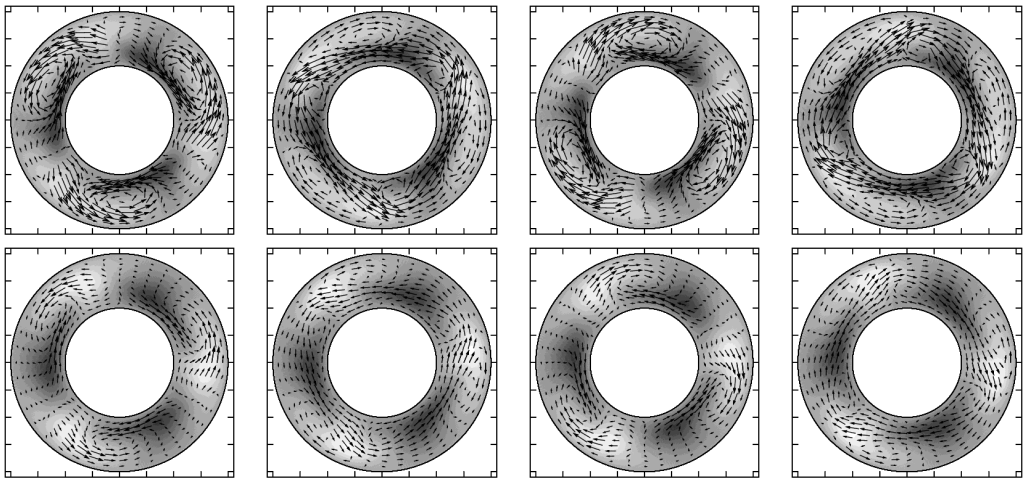

Figure 5.6: The disturbance flow field $\mathbf{u}$ for $(\eta, m_0, \alpha, R) = (0.5, 3, 0.51, 350)$. The top/bottom four figures correspond to the upper/lower- branch solutions. Arrows indicate the projection of the velocity on the cross-section, $\xi = (k/4)(2\pi/\alpha)$, $k = 0, 1, 2, 3$ (from left to right). The grey scale represents the axial velocity component (light: fast, dark: slow).

ber pair', $(m_0, \alpha) = (3, 0.51)$, for $\eta = 0.5$ are given in figure 5.5. It is seen that as R increases the profile becomes sharper near the cylinders with larger momentum transfer than in the central region. The flat central region becomes wider, especially for the upper-branch.

Also, the disturbance flow field $\mathbf{u}$ in the axial direction is shown in figure 5.6. It can be observed that slow speed streaks occupy the region near the inner cylinder whereas fast speed streaks are located near the outer cylinder. The structure of the streaks along the axial direction is also depicted in figure 5.7. Sinusoidal variation of the fast and slow speed streaks can be seen. At $r = r_m$ the fast speed streaks are accompanied by radially outward velocities whereas the slow speed streaks are accompanied by radially inward

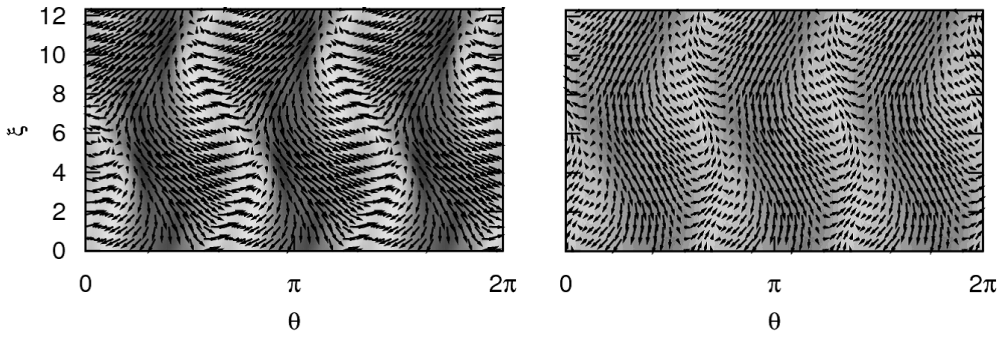

Figure 5.7: The disturbance flow field $\mathbf{u}$ for $(\eta, m_0, \alpha, R) = (0.5, 3, 0.51, 350)$ on the mean radius $r = r_m$. The grey scale represents the radial velocity component. The left/right figures correspond to the upper/lower-branch solutions.

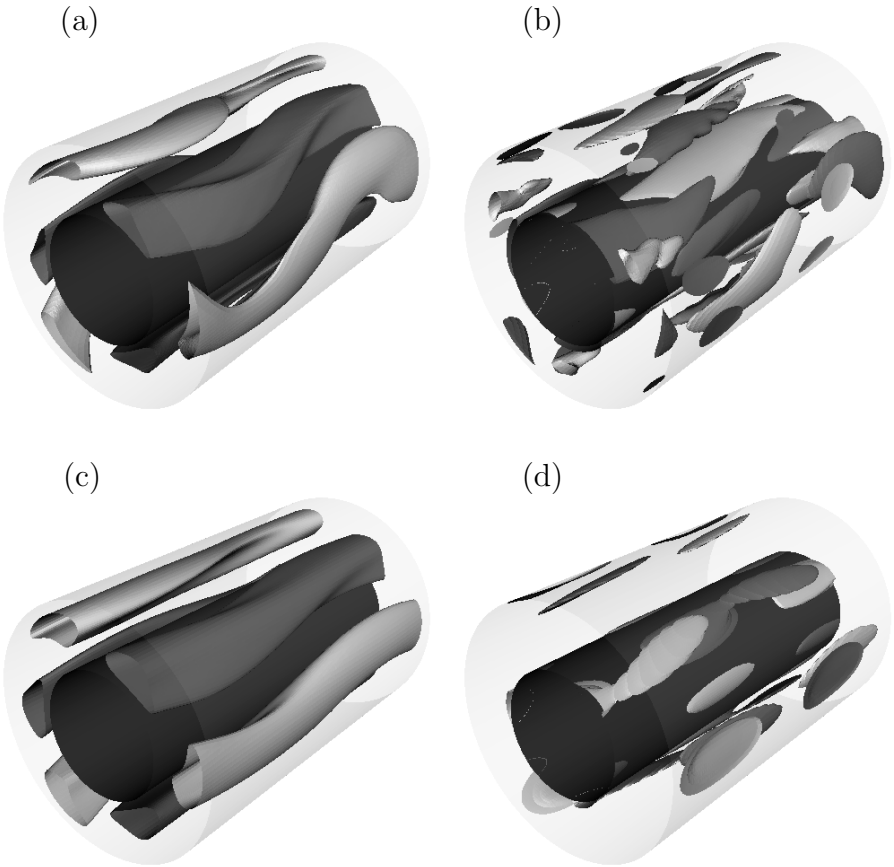

Figure 5.8: The axial variation of the streaks for the travelling-wave solutions for $(\eta, m_0, \alpha, R) = (0.5, 3, 0.51, 350)$. (a),(c): The isosurface of the axial velocity at $u = \pm 70$. Light/dark grey surfaces correspond to the fast/slow streaks. (b),(d): The isosurface of the axial vorticity at $\omega_x = \pm 90$. Light/dark grey surfaces correspond to positive/negative vorticities. (a) and (b) correspond to the upper-branch solution whereas (c) and (d) to the lower-branch solution.

	Upper				Lower			
(L, M, N)	Δ	c/R	$\|L_i\|_2$	$\|F_i\|_2$	Δ	c/R	$\|L_i\|_2$	$\|F_i\|_2$
(19,10,10)	1.56900	0.41746	3.3e4	4.9e-8	1.41512	0.35393	1.4e4	2.0e-9
(30,10,10)	1.56901	0.41746	4.1e4	8.2e-8	1.41511	0.35393	1.7e4	6.9e-9
(19,15,10)	1.57075	0.41717	3.4e4	5.3e-8	1.41716	0.35426	1.4e4	2.4e-9
(19,10,15)	1.56880	0.41751	3.4e4	4.6e-8	1.41512	0.35393	1.4e4	3.4e-9

Table 5.3: The momentum transfer Δ, the wavespeed c and the L_2-norms $\|L_i\|_2$ and $\|F_i\|_2$ at different truncation levels (L, M, N) for the non-axisymmetric solution at $(\eta, \alpha, m_0, R) = (0.1, 0.59, 1, 300)$.

velocities. Figures 5.8 (a) and (b) show the isosurfaces of the axial velocity component, u, and the axial vorticity component, $\omega_x = r^{-1}\partial_r(rw) - r^{-1}\partial_\theta v$, of the upper-solution branch. Those corresponding to the lower-branch solution are given in figures 5.8 (c) and (d). By superposing figure 5.8 (a) on figure 5.8 (b), or figure 5.8 (c) on figure 5.8 (d) it can be seen that the streaks are flanked by stronger vorticities.

5.2 Bifurcation of the mirror-symmetric solution

5.2.1 Results for wider gap case

In this section we continue the SCF solution to values of η as low as 0.1 for $m_0 = 1$. To maintain accuracy it is necessary to increase truncations to $(L, M, N) = (19, 10, 10)$ (see Table 5.3). The momentum transfer Δ of the continued solutions changes with α as indicated by the solid curves in figure 5.9. The amplitude coefficients of the solution which satisfy $m + n \in$ odd integers vanish at the points (circle), creating a new highly symmetric solution branch (dashed curve) as shown in figures 5.9 (a) and (b). The behaviour of the amplitudes suggests that this new type of solution satisfies the symmetry

$$\text{(iii)} : [u, v, w](\xi, y, \zeta) = [u, v, w](\xi + \pi, y, \zeta + \pi), \tag{5.4}$$

together with the symmetry (i). The combined symmetry, (i) and (iii), represents the mirror symmetry

$$\text{(i)} + \text{(iii)} : [u, v, w](\xi, y, \zeta) = [u, v, -w](\xi, y, -\zeta + \pi). \tag{5.5}$$

We label this type of solution as class $\mathcal{M}$, and the solution which was continued previously from PCF in section 5.1 as the class $\mathcal{S}$.

The branches of the classes $\mathcal{S}$ and $\mathcal{M}$ solutions change their shapes in a complex manner as R is varied from 360 to 320 (see figures 5.9 (a), (b) and (c)). During the transformation, some branches are reconnected due to the transcritical bifurcations and one closed curve of the class $\mathcal{S}$ and two closed curves of the class $\mathcal{M}$ are formed at $R = 300$. Each of these closed curves in the (α, Δ) plane corresponds to the cross-sections of the 'nose' in the (α, R, Δ) space. The tip of the nose for the class $\mathcal{S}$ is located at $R = 288.6$ with $\alpha = 0.59$, and the tips of the two noses for the class $\mathcal{M}$ are at $R = 291.8$ and $R = 294.7$ with $\alpha = 0.77$ and $\alpha = 0.86$, respectively, as shown in figure 5.10. Thus, the present solutions with $\eta = 0.1$, the first emerging state with increasing R is the class $\mathcal{S}$ solution, as is therefore similar to the PCF case, in which the Nagata solution first appears with increasing R. The flow fields of the class $\mathcal{S}$ solution and the two class $\mathcal{M}$ solutions along the axial direction at $R = 300$ are shown in figure 5.11. For all three solutions, low-speed streaks stay near the inner cylinder almost without changing their positions whereas fast-speed streaks oscillate in the azimuthal direction. The regions of the most violent cross-sectional motion coincide with the regions of the fast-speed streaks. The streaks and the axial vorticity for these solutions are given in figures 5.12, where the streaks are flanked by strong axial vortices similar to $\eta = 0.5$ case. The physical and mathematical explanation of this typical flow structure will be given in section 6.3.

For $m_0 = 2$, solutions of the class $\mathcal{M}$ and the class $\mathcal{S}$ first appear at Reynolds numbers about two times higher than those for $m_0 = 1$. Thus the optimum wavenumber for minimum R is given by $m_0 = 1$ for both of the solutions. Bifurcation points that connect the classes $\mathcal{S}$ and $\mathcal{M}$ have not been detected with this azimuthal wavenumber choice.

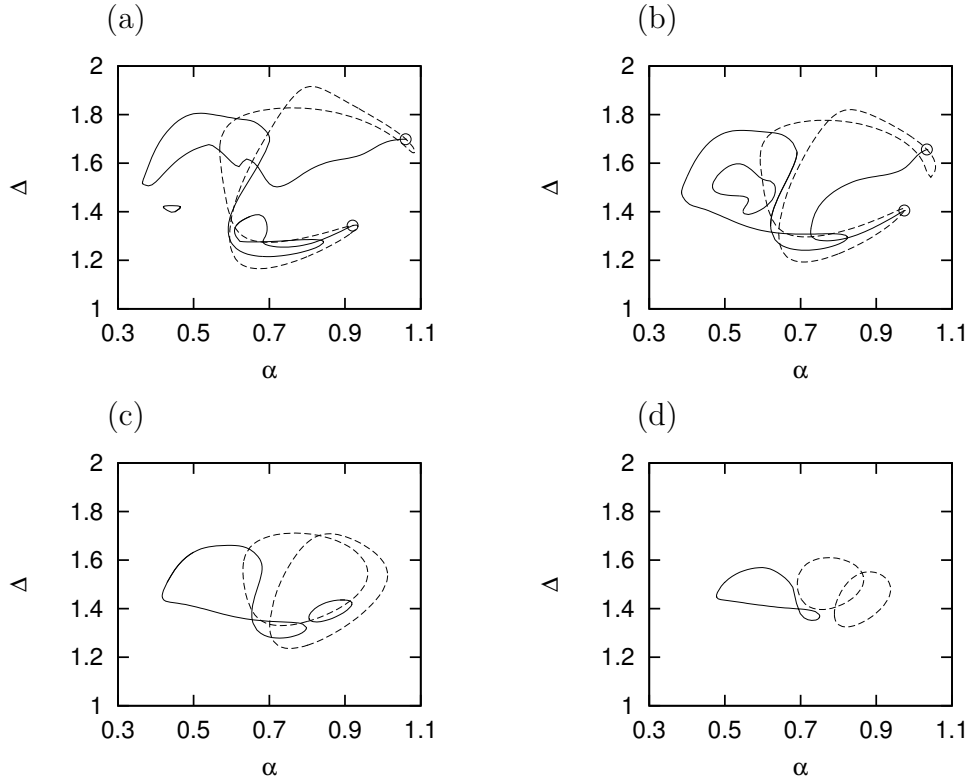

Figure 5.9: The momentum transfer of the solutions for $\eta = 0.1$. Solid/dashed curves represent the class $\mathcal{S}/\mathcal{M}$ solutions with $m_0 = 1$. (a): $R = 360$, (b): $R = 340$, (c): $R = 320$, (d): $R = 300$. Circles in (a) and (b) are the bifurcation points. The truncation level $(L, M, N) = (19, 10, 10)$ is used to draw the curve.

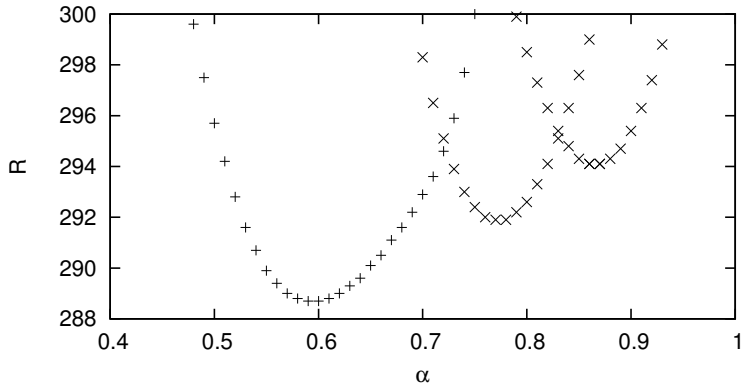

Figure 5.10: The saddle-node bifurcations for the non-axisymmetric solutions for $\eta = 0.1$. $+/\times$ represents the class $\mathcal{S}/\mathcal{M}$ solutions with $m_0 = 1$.

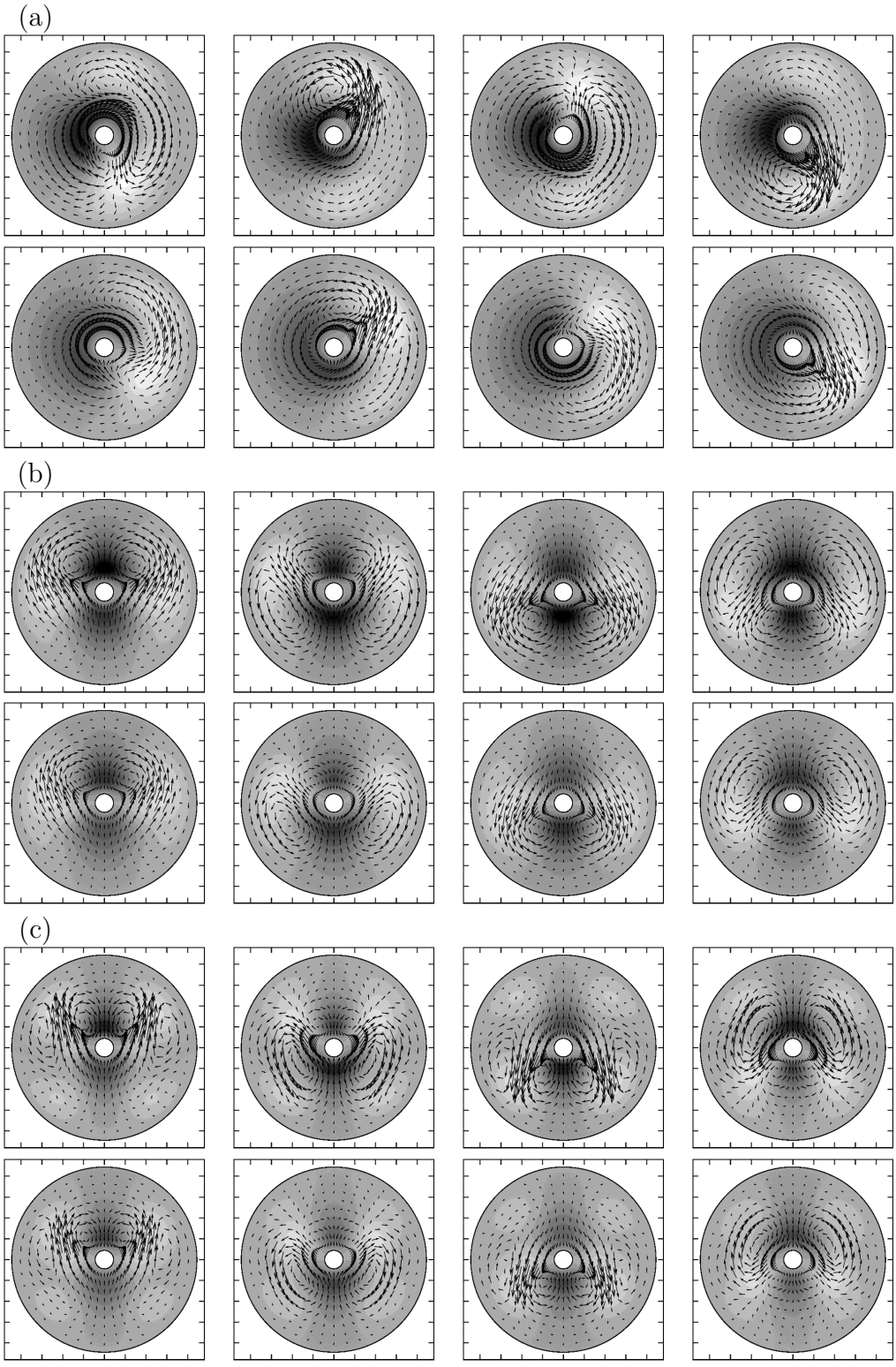

Figure 5.11: The disturbance flow field for $(\eta, m_0, R) = (0.1, 1, 300)$. The top/bottom four figures correspond to the upper/lower-branch solutions. Arrows indicate the projection of the velocity on the cross-section, $\xi = (k/4)(2\pi/\alpha)$, $k = 0, 1, 2, 3$ (from left to right). The grey scale represents the axial velocity component (light:fast,dark:slow). (a): the class $\mathcal{S}$ with $\alpha = 0.59$, (b): the class $\mathcal{M}$ with $\alpha = 0.77$, (c): the class $\mathcal{M}$ with $\alpha = 0.86$.

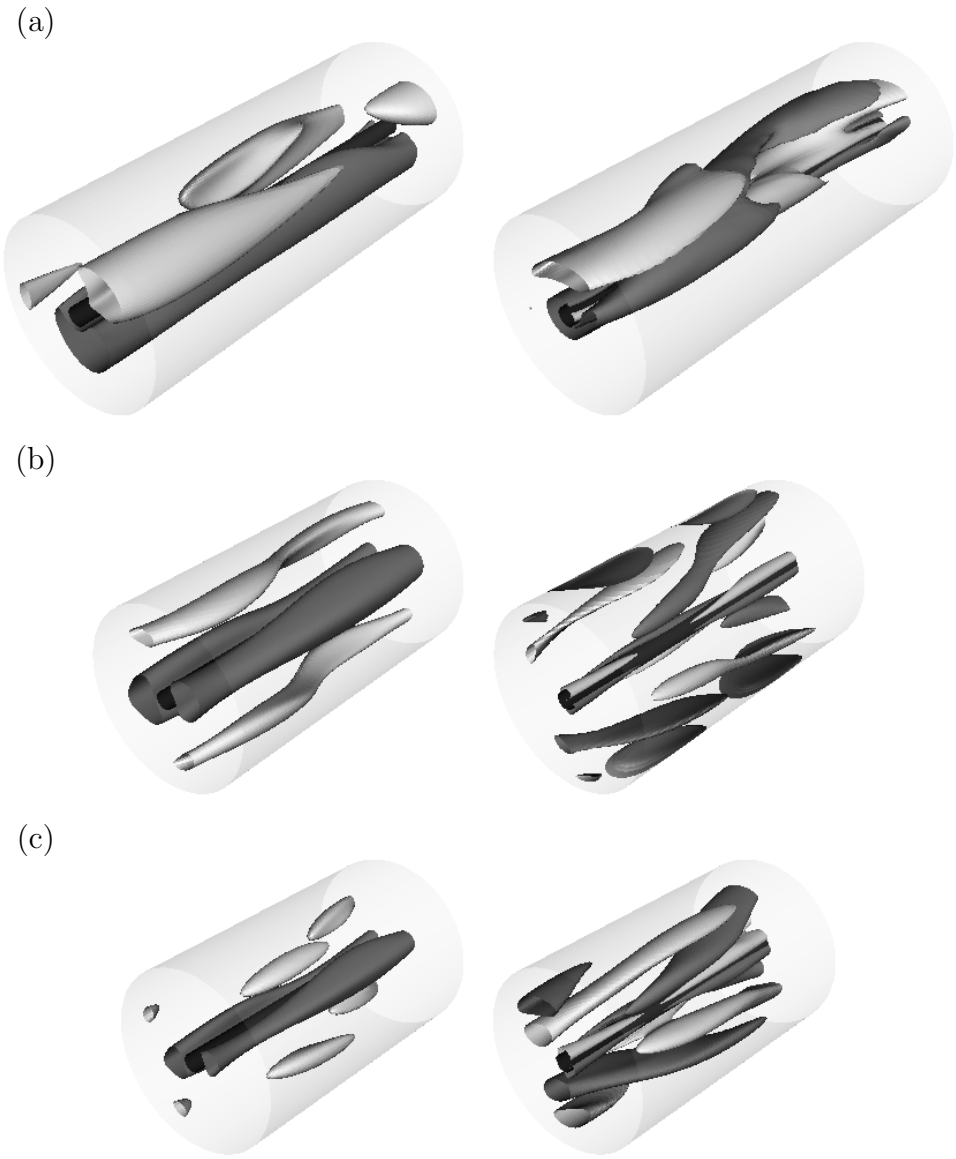

Figure 5.12: The axial variation of the streaks for the travelling-wave solutions for $(\eta, m_0, R) = (0.1, 1, 300)$. Left: The isosurface of the axial velocity at $u = \pm 50$. Light/dark grey surfaces correspond to the fast/slow speed streaks. Right: The isosurface of the axial vorticity at $\omega_x = \pm 50$. Light/dark grey surfaces correspond to positive/negative vorticities. (a): the class $\mathcal{S}$ with $\alpha = 0.59$, (b): the class $\mathcal{M}$ with $\alpha = 0.77$, (c): the class $\mathcal{M}$ with $\alpha = 0.86$.

5.2.2 The symmetry of PCF and SCF solutions

Here we deduce all possible symmetries of PCF and SCF solutions, and confirm that the results in the previous sections are mathematically consistent to the symmetries of the flow configurations.

Introducing $\mathbf{X} = [u, v, w, p, c, c_z](\xi, y, \zeta)$, we can express the Navier-Stokes equations (2.2) and (2.1) as $\mathbf{F}(\mathbf{X}) = \mathbf{0}$. Defining the translation operators

$$\tau_\xi^X [u, v, w, p, c, c_z](\xi, y, \zeta) = [u, v, w, p, c, c_z](\xi + \pi, y, \zeta), \tag{5.6}$$

$$\tau_\zeta^Z [u, v, w, p, c, c_z](\xi, y, \zeta) = [u, v, w, p, c, c_z](\xi, y, \zeta + \pi) \tag{5.7}$$

we find $\mathbf{F}(\mathbf{X}) = 0 \Leftrightarrow \mathbf{F}(\tau_\xi^X \mathbf{X}) = 0 \Leftrightarrow \mathbf{F}(\tau_\zeta^Z \mathbf{X}) = 0$ for any $X, Z \in \mathbb{R}$.

Since we consider solutions $\mathbf{X}$ in the periodic domain, $\mathbf{X} = \tau_\xi^m \mathbf{X} = \tau_\zeta^n \mathbf{X}$ for any $m, n \in \mathbb{Z}$. Therefore, note that τ_ξ^{m+X} and τ_ξ^X represent the same operator for any $m \in \mathbb{Z}$ and $X \in \mathbb{R}$ (similar argument also holds for τ_ζ^Z).

In the present section we consider only the planar geometry case $\eta = 1$, for which flows can possess the larger number of symmetries (see earlier discussion in section 5.1). Throughout we will consider the general antisymmetric basic flow profile $\mathbf{U_B} = U_B \mathbf{e}_x$ where $U_B(y) = -U_B(-y)$, which the PCF basic flow satisfies if an appropriate Galilean transformation is performed. This situation allows the following symmetries of *the system*:

$$\mathbf{F}(\mathbf{X}) = 0 \Leftrightarrow \mathbf{F}(\sigma_\zeta \mathbf{X}) = 0 \Leftrightarrow \mathbf{F}(\sigma_{\xi y} \mathbf{X}) = 0 \Leftrightarrow \mathbf{F}(\sigma_\zeta \sigma_{\xi y} \mathbf{X}) = 0, \tag{5.8}$$

where

$$\sigma_\zeta [u, v, w, p, c, c_z](\xi, y, \zeta) = [u, v, -w, p, c, -c_z](\xi, y, -\zeta), \tag{5.9}$$

$$\sigma_{\xi y} [u, v, w, p, c, c_z](\xi, y, \zeta) = [-u, -v, w, p, -c, c_z](-\xi, -y, \zeta). \tag{5.10}$$

Based on these relations, we next examine the symmetry of *the solutions*. The general

problem when we consider expression of symmetry of solutions is that it depends on the choice of the origin of the coordinate system. Thus we say solution $\mathbf{X}$ is symmetric under (denoted by s.u. for short) operator S if there exist $X, Z \in \mathbb{R}$ such that $\tau_\xi^X \tau_\zeta^Z \mathbf{X} = S\tau_\xi^X \tau_\zeta^Z \mathbf{X}$. With this definition, the allowable symmetry operations are clarified in the following theorem.

Theorem 1. We assume the solution $\mathbf{X}(\xi, y, \zeta)$ is periodic in (ξ, ζ) directions with the fundamental wavenumber pair (α, β), i.e. $\mathbf{X} = \tau_\xi^X \mathbf{X} \Leftrightarrow X \in \mathbb{Z}$ and $\mathbf{X} = \tau_\zeta^Z \mathbf{X} \Leftrightarrow Z \in \mathbb{Z}$. If $\mathbf{X}$ is s.u. S, where S is an arbitrary combination of $\tau_\xi^X, \tau_\zeta^Z, \sigma_\zeta$ and $\sigma_{\xi y}$ for any $X, Z \in \mathbb{R}$, then $\mathbf{X}$ is s.u. one of: *identity*, σ_ζ, $\tau_\xi^{1/2}\sigma_\zeta$, $\sigma_{\xi y}$, $\tau_\zeta^{1/2}\sigma_{\xi y}$, $\sigma_\zeta\sigma_{\xi y}$ or $\tau_\xi^\delta \tau_\zeta^\epsilon$ where δ, ϵ are non-integer real numbers.

The proof is as follows. Note that $\tau_\xi^X \sigma_{\xi y} \mathbf{X} = \sigma_{\xi y} \tau_\xi^{-X} \mathbf{X}$ for any $X \in \mathbb{R}$ and $\tau_\zeta^Z \sigma_\zeta \mathbf{X} = \sigma_\zeta \tau_\zeta^{-Z} \mathbf{X}$ for any $Z \in \mathbb{R}$. By using these relations, S can be expressed as one of $\tau_\xi^\delta \sigma_\zeta$, $\tau_\zeta^\epsilon \sigma_{\xi y}$, $\sigma_\zeta \sigma_{\xi y}$ or $\tau_\xi^\delta \tau_\zeta^\epsilon$ for some $\delta, \epsilon \in \mathbb{R}$. If $S = \tau_\xi^\delta \sigma_\zeta$, δ must be $\mathbb{Z}$ or $\mathbb{Z} + 1/2$ because $\mathbf{X} = S\mathbf{X} \Rightarrow \mathbf{X} = S^2\mathbf{X} = \tau_\xi^{2\delta}\mathbf{X}$. Similarly ϵ should belong to $\mathbb{Z}$ or $\mathbb{Z} + 1/2$ for $\tau_\zeta^\epsilon \sigma_{\xi y}$. Given that we cannot deduce any extra conditions for the case of the double translations, $S = \tau_\xi^\delta \tau_\zeta^\epsilon$. This completes the proof.

We can classify solutions $\mathbf{X}$ in terms of symmetries like as $\mathrm{Sym}(\sigma_\zeta) \equiv \{\mathbf{X}$ satisfies the requirement of the theorem 1 $|\mathbf{X}$ is s.u. σ_ζ but not s.u. $\tau_\xi^{1/2}\sigma_\zeta$, $\sigma_{\xi y}$, $\tau_z^{1/2}\sigma_{\xi y}$, $\sigma_\zeta\sigma_{\xi y}$ and $\tau_\xi^\delta\tau_\zeta^\epsilon$ $\}$. In principle it is possible to list all of the symmetry classes since the number of elements we have to consider is finite. There exist 15 distinct classes as follows:

- $\mathcal{I} \equiv \mathrm{Sym}()$,
- $\mathcal{I}^* \equiv \mathrm{Sym}(\sigma_\zeta\sigma_{\xi y})$,
- $\mathcal{E} \equiv \mathrm{Sym}(\sigma_{\xi y})$,
- $\mathcal{E}^* \equiv \mathrm{Sym}(\sigma_\zeta,\ \sigma_{\xi y},\ \sigma_\zeta\sigma_{\xi y})$,
- $\mathcal{S} \equiv \mathrm{Sym}(\tau_\xi^{1/2}\sigma_\zeta)$,
- $\mathcal{S}^* \equiv \mathrm{Sym}(\tau_\xi^{1/2}\sigma_\zeta,\ \sigma_{\xi y},\ \sigma_\zeta\sigma_{\xi y})$,
- $\mathcal{D} \equiv \mathrm{Sym}(\sigma_\zeta)$,
- $\mathcal{D}^* \equiv \mathrm{Sym}(\sigma_\zeta,\ \tau_\zeta^{1/2}\sigma_{\xi y},\ \sigma_\zeta\sigma_{\xi y})$,
- $\mathcal{R} \equiv \mathrm{Sym}(\tau_\zeta^{1/2}\sigma_{\xi y})$,
- $\mathcal{R}^* \equiv \mathrm{Sym}(\tau_\xi^{1/2}\sigma_\zeta,\ \tau_\zeta^{1/2}\sigma_{\xi y},\ \sigma_\zeta\sigma_{\xi y})$,
- $\mathcal{T}_{\epsilon,\delta} \equiv \mathrm{Sym}(\tau_\xi^\delta\tau_\zeta^\epsilon)$,
- $\mathcal{T}^*_{\epsilon,\delta} \equiv \mathrm{Sym}(\sigma_\zeta\sigma_{\xi y},\ \tau_\xi^\delta\tau_\zeta^\epsilon)$,

- $\mathcal{M} \equiv \mathrm{Sym}(\sigma_\zeta,\ \tau_\xi^{1/2}\sigma_\zeta,\ \tau_\xi^{1/2}\tau_\zeta^{1/2})$,
- $\mathcal{N} \equiv \mathrm{Sym}(\sigma_{\xi y},\ \tau_\zeta^{1/2}\sigma_{\xi y},\ \tau_\xi^{1/2}\tau_\zeta^{1/2})$,
- $\mathcal{M}^* \equiv \mathrm{Sym}(\sigma_\zeta,\ \tau_\xi^{1/2}\sigma_\zeta,\ \sigma_{\xi y},\ \tau_\zeta^{1/2}\sigma_{\xi y},\ \sigma_\zeta\sigma_{\xi y},\ \tau_\xi^{1/2}\tau_\zeta^{1/2})$.

Some symmetry classes fix the shift value (δ, ϵ) to $(\mathbb{Z}+1/2, \mathbb{Z}+1/2)$. The class of solution should be unchanged along the solution branch as long as there is no bifurcation and the symmetry of the system is preserved. In other words, if the symmetry of the system is changed, the class of solution could change without bifurcation. For example, in the case of $\eta \neq 1$, for solutions $\mathbf{F}(\mathbf{X}) = 0$ it is not the case that $\mathbf{F}(\sigma_{\xi y}\mathbf{X}) = 0$ and $\mathbf{F}(\sigma_\zeta\sigma_{\xi y}\mathbf{X}) = 0$. Therefore symmetries S that contain $\sigma_{\xi y}$ and $\sigma_\zeta\sigma_{\xi y}$ are no longer allowed, and the number of possible classes reduces to 5: $\mathcal{I}$, $\mathcal{D}$, $\mathcal{S}$, $\mathcal{T}_{\epsilon,\delta}$ and $\mathcal{M}$.

The solution $\mathbf{X}$ which is s.u. $S = \sigma_\zeta\sigma_{\xi y}$ is sometimes referred to as steady solution, because c and c_z must be zero in this case. Similarly, $c = 0$ if $\mathbf{X}$ is s.u. σ_ζ or $\tau_\xi^{1/2}\sigma_\zeta$, and $c_z = 0$ if $\mathbf{X}$ is s.u. $\sigma_{\xi y}$ or $\tau_\zeta^{1/2}\sigma_{\xi y}$. Note that these relations for wavespeeds hold when present particular Galilean flame, which assure the symmetry of basic flow, is chosen. For example, for plane Couette flow with basic flow $(U_B, W_B) = (R(1-y)/2, 0)$, steady solutions have $(c, c_z) = (R/2, 0)$ as we observed in figure 5.1 (b).

According to this classification, the Nagata solution in PCF belongs to class $\mathcal{S}^*$. However, with the introduction of non-zero curvature into the problem geometry, this solution becomes a class $\mathcal{S}$ solution by symmetry breaking of the system (c.f. section 5.1).

5.3 Linear stability of non-axisymmetric solutions

Finally in the present chapter, we examine the stability of the travelling-wave solutions in the previous sections. The strategy here is the same as that for basic solution, i.e. we superimpose an infinitesimal perturbations on the flow field (chapter 3). Here we restrict our attention to disturbances with the fundamental mode, namely the disturbance has the

same wavenumbers as the travelling-wave solution. The velocity field is now given by

$$\mathbf{u} = \mathbf{u}_{TW} + \check{\mathbf{u}} = (\overline{u}_{TW} + \overline{\check{u}})\mathbf{e}_x + (\overline{w}_{TW} + \overline{\check{w}})\mathbf{e}_\theta + \nabla \times \nabla \times ((\phi_{TW} + \check{\phi})\mathbf{e}_r) + \nabla \times ((\psi_{TW} + \check{\psi})\mathbf{e}_r), \tag{5.11}$$

where the subscript TW denotes the travelling-wave solution and the check $(\check{*})$ denotes the superimposed infinitesimal perturbations. The perturbations $\check{\phi}$, $\check{\psi}$, $\overline{\check{u}}$, $\overline{\check{w}}$ are expanded as

$$\check{\phi}(\xi, y, \zeta, t) = \sum_{l=0}^{L} \sum_{\substack{m=-M \\ (m,n)\neq(0,0)}}^{M} \sum_{n=-N}^{N} \check{X}^{(1)}_{lmn} \Phi_l(y) \exp(\mathrm{i}m\zeta + \mathrm{i}n\xi + st), \tag{5.12}$$

$$\check{\psi}(\xi, y, \zeta, t) = \sum_{l=0}^{L} \sum_{\substack{m=-M \\ (m,n)\neq(0,0)}}^{M} \sum_{n=-N}^{N} \check{X}^{(2)}_{lmn} \Psi_l(y) \exp(\mathrm{i}m\zeta + \mathrm{i}n\xi + st), \tag{5.13}$$

$$\overline{\check{u}}(y, t) = \sum_{l=0}^{L} \check{X}^{(1)}_{l00} U_l(y) \exp(st), \tag{5.14}$$

$$\overline{\check{w}}(y, t) = \sum_{l=0}^{L} \check{X}^{(2)}_{l00} W_l(y) \exp(st) \tag{5.15}$$

where the travelling-wave coordinates ζ and ξ and the truncation levels (L, M, N) must be the same as the travelling-wave solution.

Substituting expansions (5.12)–(5.15) into governing equations (2.8)–(2.11) for $\phi = \phi_{TW} + \check{\phi}$, $\psi = \psi_{TW} + \check{\psi}$, $\overline{u} = \overline{u}_{TW} + \overline{\check{u}}$ and $\overline{w} = \overline{w}_{TW} + \overline{\check{w}}$, and employing the same Fourier-Galerkin, Chebyshev-collocation technique as used for Newton's method in section 2.3, we obtain a linear algebraic eigenvalue problem. Using the same notation as in equation (2.21), this problem can be expressed as

$$\{D_{ij} + H_{ijk}X_k + H_{ikj}X_k + \mathrm{i}(mm_0c_\theta + n\alpha c)B_{ij}\}\check{X}_j = sB_{ij}\check{X}_j, \tag{5.16}$$

where $\check{X}_i \in \check{X}^{(j)}_{lmn}$ and $X_i \in X^{(j)}_{lmn}$.

Our numerical analysis shows that (5.16) has always two zero eigenvalues. These eigenvalues result from the fact that SCF is invariant under azimuthal and axial translations.

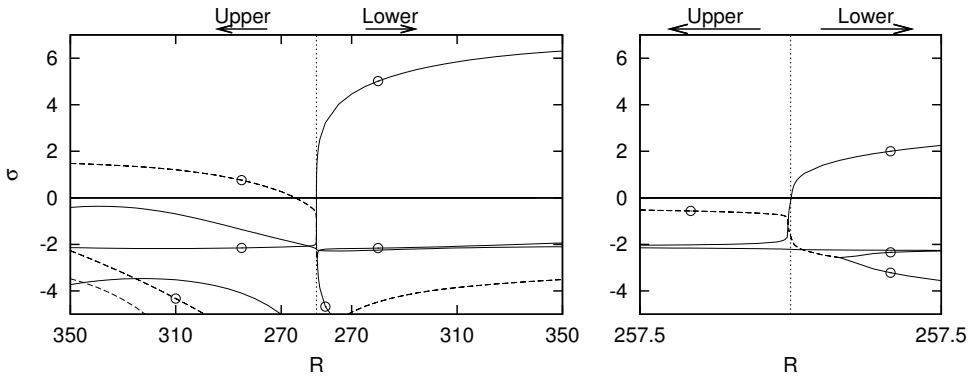

Figure 5.13: The real part σ of the growth rate s of the travelling-wave solution for $\eta = 0.5$ corresponding to those with $m_0 = 3$ at $\alpha = 0.51$ in figure 5.4. The solid/dashed curves imply that the imaginary part γ of the growth rate s is zero/non-zero. The figure includes two growth rates $s \equiv 0$ for any R. Curves with an open circle correspond to the perturbation with the symmetry (i). The right figure is a close-up near the saddle-node bifurcation point (dotted vertical line).

Figures 5.13 and 5.14 show real part σ of the growth rate s around the saddle-node in the case $\eta = 0.5$ and 0.1, respectively. Recall that the class $\mathcal{S}$ solution possesses the symmetry (i) only, whereas the class $\mathcal{M}$ solution possesses the symmetries (i) and (iii). The curves with an open circle in these figures correspond to the eigenvalues calculated by restricting $\check{X}_i$ to those with the symmetry (i) and the curves with a closed circle correspond to eigenvalues calculated by restriction to $\check{X}_i$ with the symmetry (iii). The curves with both open and closed circles correspond to the eigenvalues calculated by restricting $\check{X}_i$ to those with both of the symmetries (i) and (iii). It is seen that the lower-branch solutions are always unstable against the fundamental mode and, consistent with the bifurcation theory, the real eigenvalue crosses zero at the saddle-node bifurcation point (dotted vertical line). Except for figure 5.14 (c), the lower-branch solutions have only one growing eigenmode. These lower-branch solutions can be expected to play particularly important roles in transition dynamics, since such solutions can be realized in simulation by controlling only one flow parameter, e.g. energy (therefore these solutions are identical to edge states). For the same solution branches, it is also found that the upper-branch counterparts are stable in a small region next to the saddle-node. As R increased, these stable solutions soon become unstable against the perturbation with the symmetry (i): the corresponding eigenvalues are complex, and so some sort of time-dependent solutions which keep the shift-refection symmetry are expected.

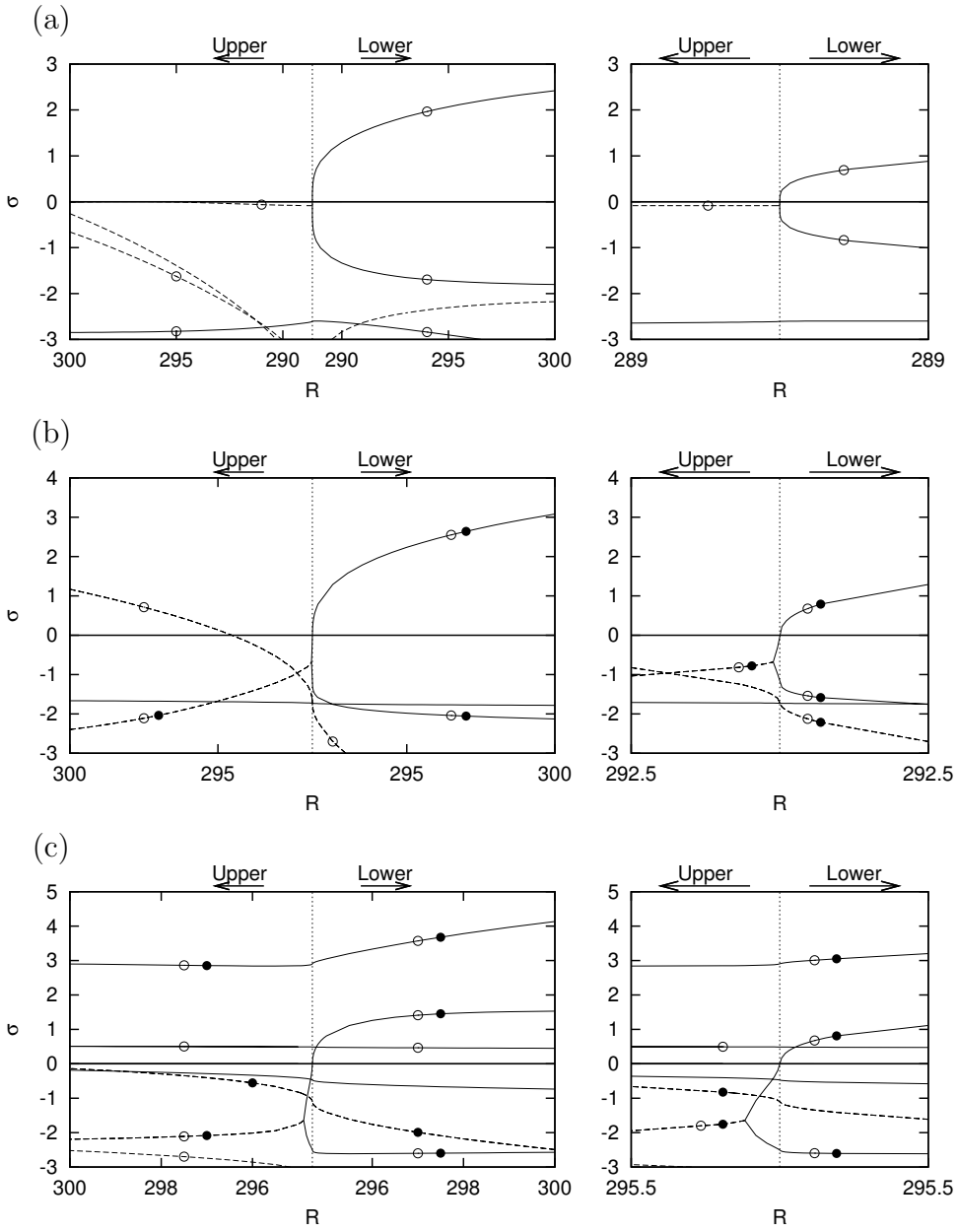

Figure 5.14: The real part σ of the growth rate s of the three travelling-wave solutions $(\eta, m_0) = (0.1, 1)$ corresponding to those in figure 5.10. The solid/dashed curves imply that the imaginary part γ of the growth rate s is zero/non-zero. The figures include two growth rates $s \equiv 0$ for any R. Curves with an open or closed circle correspond to the perturbation with the symmetry (i) or (iii). Curves with both open and closed circles correspond to the perturbation with the symmetries both (i) and (iii). The right figure is a close-up near the saddle-node bifurcation point (dotted vertical line). (a): the class $\mathcal{S}$ with $\alpha = 0.59$, (b): the class $\mathcal{M}$ with $\alpha = 0.77$, (c): the class $\mathcal{M}$ with $\alpha = 0.86$.

5.4 Summary

In order to investigate the possibility for the existence of finite-amplitude solutions other than axisymmetric solutions in chapter 4, especially in a relatively low Reynolds number region, we used the three-dimensional PCF equilibrium solution by Nagata (1990) in the limit of narrow gap ($\eta = 1$) and continued it to wider cases ($\eta < 1$). This homotopy approach proves to be successful and the resulting non-axisymmetric nonlinear solutions travelling in the axial direction are found. They are characterised by fast and slow speed streaks flanked by strong axial vortices, as is typical for other exact coherent structures.

These solutions result from saddle-node bifurcations at $R = O(10^2)$ and exist for a wide range of η. For $\eta = 0.5$, where the linear critical state is absent, the Reynolds number at the saddle-node bifurcations reaches a minimum, which is approximately 256.6 for the optimal azimuthal and axial wavenumbers $(m_0, \alpha) = (3, 0.51)$. Recalling that the linear critical state is absent for $\eta = 0.5$, it is very likely that the lower-branch solutions originate from the finite-amplitude streaky field at asymptotically large R as described by Wang, Gibson & Waleffe (2007) in the case of PCF. We will give a detailed discussion for this point in section 6.3.

We also obtained mirror symmetric solutions for $\eta = 0.1$ by bifurcation. There are two distinct mirror symmetric solution families at the low R range, which give minimum $R =$ 291.8 and 294.7. However, the lowest minimum Reynolds number 288.6 is still given by non-mirror symmetric solutions continued from PCF. All the minima for $\eta = 0.1$ are obtained when the azimuthal wavenumber $m_0 = 1$.

The linear stability analysis of non-axisymmetric travelling-wave solutions, though restricted to the fundamental mode, shows that the lower-branch solutions are always unstable, and that stable upper-branch solutions may exist in a small region next to the saddle-node bifurcation point. It is also found that the several lower-branch solutions only have one unstable mode and thus coincide to the 'edge states' in SCF.

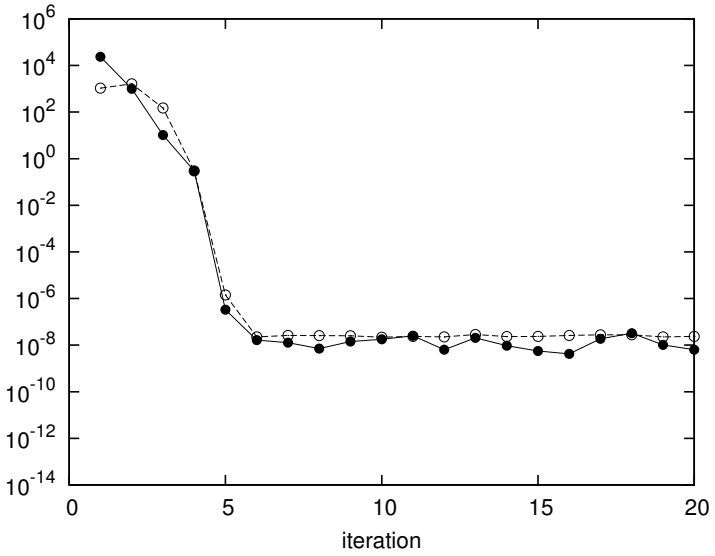

Figure 5.15: The accuracy of the solution for the nonlinear algebraic equation (2.21) based on the maximum relative error ϵ (closed circles) and the L_2-norm of the residual $\|F_i\|_2$ (open circles) as a function of the Newton-Raphson iteration. $(\eta, m_0, \alpha, R) = (0.5, 3, 0.50, 350)$. $(L, M, N) = (16, 8, 9)$. Double precision is used.

5.A Appendix

5.A.1 Convergence criterion of Newton-Raphson method

An example of the variation of ϵ in (2.22) as the Newton-Raphson iteration is repeated is shown in figure 5.15. The calculation is undertaken at $(\eta, m_0, \alpha, R) = (0.5, 3, 0.50, 350)$ with the resolution $(L, M, N) = (16, 8, 9)$. We use the converged solution at $(\eta, m_0, \alpha, R) = (0.5, 3, 0.51, 350)$ as an initial guess. Double precision arithmetic is used. We can see from the closed circles in figure 5.15 that the accuracy does not improve once the criterion (2.22) is satisfied at the fifth iteration. As for the L_2-norm of the residual of (2.21), $\|F_i\|_2$ is not reduced after the fifth iteration either (see the open circles in figure 5.15). However, the value of $\|F_i\|_2$ for the approximation obtained by using the criterion (2.22) smaller than that expected when compared with the typical order of the corresponding $\|L_i\|_2$ (see tables 4.1, 5.2 and 5.3). From figure 5.15, the tolerance 10^{-5} in (2.22) guarantees convergence with the signal-to-noise-floor ratio at $O(10^{-11})$–$O(10^{-12})$.

5.A.2 Symmetry for other basic flow field

(i) *Symmetry for system of symmetric basic flow*

For the reader who is interested in the possible symmetry of solutions for symmetric basic flow profile, i.e. $U_B(y) = U_B(-y)$, here we exhibit similar analysis for this case as in subsection 5.2.2 where antisymmetric basic flow is considered. In this case the system has symmetries

$$\mathbf{F}(\mathbf{X}) = 0 \Leftrightarrow \mathbf{F}(\sigma_\zeta \mathbf{X}) = 0 \Leftrightarrow \mathbf{F}(\sigma_y \mathbf{X}) = 0 \Leftrightarrow \mathbf{F}(\sigma_\zeta \sigma_y \mathbf{X}) = 0, \tag{5.17}$$

where $\sigma_y[u, v, w, p, c, c_z](\xi, y, \zeta) = [u, -v, w, p, c, c_z](\xi, -y, \zeta)$.
The straightforward calculation yields following 22 distinct classes.

- $\mathcal{I} \equiv \mathrm{Sym}()$,
- $\mathcal{I}^\ddagger \equiv \mathrm{Sym}(\sigma_y)$,
- $\mathcal{I}^\dagger \equiv \mathrm{Sym}(\tau_\zeta^{1/2}\sigma_y)$,
- $\mathcal{I}^\odot \equiv \mathrm{Sym}(\tau_\xi^{1/2}\sigma_y)$,
- $\mathcal{I}^\circ \equiv \mathrm{Sym}(\tau_\xi^{1/2}\tau_\zeta^{1/2}\sigma_y)$,
- $\mathcal{D} \equiv \mathrm{Sym}(\sigma_\zeta)$,
- $\mathcal{S} \equiv \mathrm{Sym}(\tau_\xi^{1/2}\sigma_\zeta)$,
- $\mathcal{P} \equiv \mathrm{Sym}(\sigma_y\sigma_\zeta)$,
- $\mathcal{Q} \equiv \mathrm{Sym}(\tau_\xi^{1/2}\sigma_y\sigma_\zeta)$,
- $\mathcal{T}_{\epsilon,\delta} \equiv \mathrm{Sym}(\tau_\xi^{\delta}\tau_\zeta^{\epsilon})$,
- $\mathcal{D}^\ddagger \equiv \mathrm{Sym}(\sigma_\zeta,\ \sigma_y,\ \sigma_y\sigma_\zeta)$,
- $\mathcal{D}^\dagger \equiv \mathrm{Sym}(\sigma_\zeta,\ \tau_\zeta^{1/2}\sigma_y,\ \sigma_y\sigma_\zeta)$,
- $\mathcal{D}^\odot \equiv \mathrm{Sym}(\sigma_\zeta,\ \tau_\xi^{1/2}\sigma_y,\ \tau_\xi^{1/2}\sigma_y\sigma_\zeta)$,
- $\mathcal{D}^\circ \equiv \mathrm{Sym}(\sigma_\zeta,\ \tau_\xi^{1/2}\tau_\zeta^{1/2}\sigma_y,\ \tau_\xi^{1/2}\sigma_y\sigma_\zeta)$,
- $\mathcal{S}^\ddagger \equiv \mathrm{Sym}(\tau_\xi^{1/2}\sigma_\zeta,\ \sigma_y,\ \tau_\xi^{1/2}\sigma_y\sigma_\zeta)$,
- $\mathcal{S}^\dagger \equiv \mathrm{Sym}(\tau_\xi^{1/2}\sigma_\zeta,\ \tau_\zeta^{1/2}\sigma_y,\ \tau_\xi^{1/2}\sigma_y\sigma_\zeta)$,
- $\mathcal{S}^\odot \equiv \mathrm{Sym}(\tau_\xi^{1/2}\sigma_\zeta,\ \tau_\xi^{1/2}\sigma_y,\ \sigma_\zeta\sigma_y)$,
- $\mathcal{S}^\circ \equiv \mathrm{Sym}(\tau_\xi^{1/2}\sigma_\zeta,\ \tau_\xi^{1/2}\tau_\zeta^{1/2}\sigma_y,\ \sigma_\zeta\sigma_y)$,
- $\mathcal{M} \equiv \mathrm{Sym}(\sigma_\zeta,\ \tau_\xi^{1/2}\sigma_\zeta,\ \tau_\xi^{1/2}\tau_\zeta^{1/2})$,
- $\mathcal{T}^\ddagger \equiv \mathrm{Sym}(\tau_\xi^{1/2}\tau_\zeta^{1/2},\ \sigma_{\xi y},\ \tau_\xi^{1/2}\tau_\zeta^{1/2}\sigma_{\xi y})$,
- $\mathcal{M}^\ddagger \equiv \mathrm{Sym}(\sigma_\zeta,\ \tau_\xi^{1/2}\sigma_\zeta,\ \tau_\xi^{1/2}\tau_\zeta^{1/2},\ \sigma_y,\ \tau_\xi^{1/2}\tau_\zeta^{1/2}\sigma_y,\ \sigma_y\sigma_\zeta,\ \tau_\xi^{1/2}\sigma_y\sigma_\zeta)$,
- $\mathcal{M}^\dagger \equiv \mathrm{Sym}(\sigma_\zeta,\ \tau_\xi^{1/2}\sigma_\zeta,\ \tau_\xi^{1/2}\tau_\zeta^{1/2},\ \tau_\zeta^{1/2}\sigma_y,\ \tau_\xi^{1/2}\sigma_y,\ \sigma_y\sigma_\zeta,\ \tau_\xi^{1/2}\sigma_y\sigma_\zeta)$.

(ii) *Symmetry for quasi-isotropic flow*

We can also investigate symmetry for a spatially periodic quasi-isotropic flow (invariant for arbitrary replacement of x, y and z) i.e. the system governing the flow is invariant under

$$R_{yxz}[u,v,w,p](x,y,z) = [v,u,w,p](y,x,z), \tag{5.18}$$

$$R_{xzy}[u,v,w,p](x,y,z) = [u,w,v,p](x,z,y), \tag{5.19}$$

$$R_{zyx}[u,v,w,p](x,y,z) = [w,v,u,p](z,y,x). \tag{5.20}$$

We assume the flow $\mathbf{X}$ is invariant under $\tau^{D,E,F}R_{yxz}$, $\tau^{D,F,E}R_{xzy}$ and $\tau^{F,E,D}R_{zyx}$ where $\tau^{F,E,D}$ denotes a shift operator. The superscripts $F, E, D \in [0, 1/2]$ represents the shift value in x, y and z directions divided by the fundamental period. Though we write these operators in general form above, as can be seen, a relation $\tau^{D,E,F}R_{yxz}\tau^{D,E,F}R_{yxz}\mathbf{X} = \tau^{D+E,D+E,0}\mathbf{X} = \mathbf{X}$, $D = E = F$ must be satisfied.

We further assume the flow $\mathbf{X}$ has reflectional symmetries

$$\sigma_x[u,v,w,p](x,y,z) = [-u,v,w,p](-x,y,z), \tag{5.21}$$

$$\sigma_y[u,v,w,p](x,y,z) = [u,-v,w,p](x,-y,z), \tag{5.22}$$

$$\sigma_z[u,v,w,p](x,y,z) = [u,v,-w,p](x,y,-z) \tag{5.23}$$

together with the shift operators $\tau^{F,E,D}$. Thus we can consider the flow $\mathbf{X}$ which is invariant under $\tau^{A,B,C}\sigma_x$, $\tau^{C,A,B}\sigma_y$, $\tau^{B,C,A}\sigma_z$ and $\tau^{D,D,D}R_{yxz}$, $\tau^{D,D,D}R_{xzy}$ and $\tau^{D,D,D}R_{zyx}$ and the symmetries generated by them. For such a flow, we find $A = B = C$ by considering $\tau^{D,D,D}R_{yxz}\tau^{C,A,B}\sigma_y\tau^{D,D,D}R_{yxz}\tau^{A,B,C}\sigma_x\mathbf{X} = \tau^{0,B+C,B+C}\mathbf{X} = \mathbf{X}$. The case $(A, D) = (0, 1/2)$ coincides to that first derived by Kida (1985) while the other cases $(A, D) = (0, 0), (1/2, 0)$ and $(1/2, 1/2)$ are also possible.

Chapter 6

Homotopy of mirror-symmetric solutions

For the past decade enormous efforts have been made to understand the dynamics of transitional and turbulent fluid motion in PCF and PF. In these flows recurrent coherent states, such as travelling waves, are transiently observed in experiments (e.g. Bech *et al.* 1995, Bottin *et al.* 1997, Bottin *et al.* 1998, Daviaud 1992, Darbyshire and Mullin 1995, Hof *et al.* 2004 and Hof *et al.* 2005) and numerical simulations (e.g. Hamilton *et al.* 1995, Kerswell & Tutty 2007, Schneider *et al.* 2007 and Willis & Kerswell 2008). However, the fact that these coherent states are unstable and the absence of a linear instability mechanism has previously prevented the discovery of nonlinear solutions to these linearly stable canonical flows.

Nevertheless, solutions to such a systems could have been obtained continuing from solutions of some other modified system by using the homotopy method. One common and effective modification for obtaining exact coherent structures, i.e. three-dimensional streamwise roll type finite-amplitude solutions, of shear flows is the introduction of an artificial force which creates finite-amplitude rolls and streaks. These rolls and streaks trigger linear instability in the modified system as explained by Waleffe's SSP. By continuing the bifurcating solution to the unforced objective system, a large number of nonlinear

Sym.	PCF	PF
$\mathcal{S}^*$	Nagata (1990)=Gibson *et al.* (2009): EQ1, EQ2, Gibson *et al.* (2009): EQ3 $\sim$ EQ6, Schneider *et al.*(2010): $\mathbf{u}_{EQ}$.	NA
$\mathcal{M}^*$	Itano & Generalis (2009), Gibson *et al.* (2009): EQ7, EQ8.	NA
$\mathcal{I}^*$	Gibson *et al.* (2009): EQ9 $\sim$ EQ13.	NA
$\mathcal{R}$	Gibson *et al.* (2009): TW1.	NA
$\mathcal{S}$	Nagata (1997)=Gibson *et al.* (2009): TW2, TW3, Schneider *et al.*(2010): $\mathbf{u}_{TW}$.	Faisst & Eckhardt (2003) =Pringle *et al.* (2009): S, Pringle *et al.* (2009): U.
$\mathcal{M}$	-	Pringle *et al.* (2009): M,N
$\mathcal{D}$	-	Pringle *et al.* (2009): D,Z

Table 6.1: The list of the known travelling-wave solutions in PCF and PF.

travelling-wave solutions for PCF and PF have been discovered (a summary of the known travelling-wave solutions to date is provided in table 6.1).

In addition to this SSP strategy, one may also anticipate that further solutions can be obtained by starting from a known solution in one problem configuration and then gradually changing the flow configuration to move to a configuration of a separate problem. It is particularly of interest to investigate homotopy connections between solutions for PCF, PF and SCF, since similar mirror-symmetric solutions have been commonly reported for these flows. In the following sections, we investigate homotopies from solutions for SCF obtained in chapter 5 to solutions for PCF and PF problems.

6.1 Towards plane Couette flow

6.1.1 Resultant homotopy path

Here we will show that two types of class $\mathcal{M}$ solutions found in section 5.2 can be followed back to PCF. The bifurcation diagram of these two solutions in SCF is replotted in figure 6.1 together with the class $\mathcal{S}$ solution. Though these two branches belong to the same symmetry class, we can observe a difference in the axial averaged flow fields in figure 6.2: one has large vortices whose scale is almost equal to the gap, whereas the other has

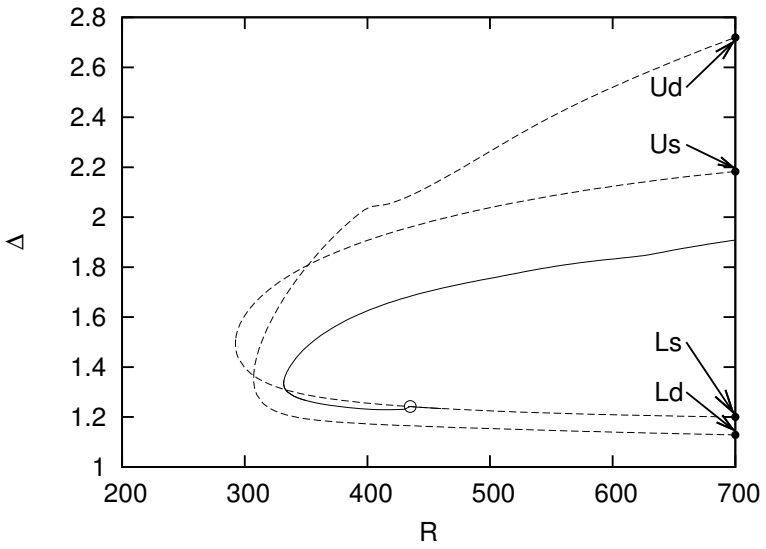

Figure 6.1: The momentum transfer of the SCF solutions for $(\eta, m_0, \alpha) = (0.1, 1, 0.75)$. The solid/dashed curves represent the class $\mathcal{S}/\mathcal{M}$ solutions. $(L, M, N) = (25, 16, 10)$. The circle is the bifurcation point. Note that $\beta \approx 0.82$.

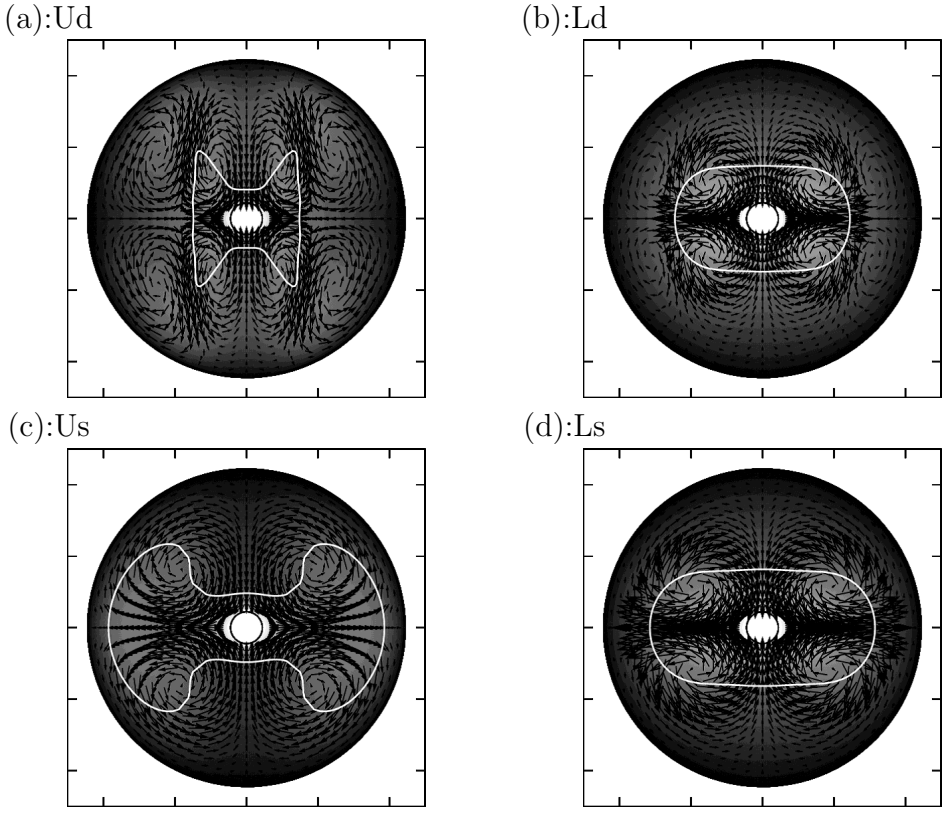

Figure 6.2: The axial averaged flow field of the SCF class $\mathcal{M}$ solutions for $(\eta, R, m_0, \alpha) = (0.1, 700, 1, 0.75)$. The grey scale represents the axial velocity component (light: fast, dark: slow). The white curves represents the critical layers, i.e. streak, steamwise averaged axial component of velocity, coincides with wavespeed of the travelling waves.

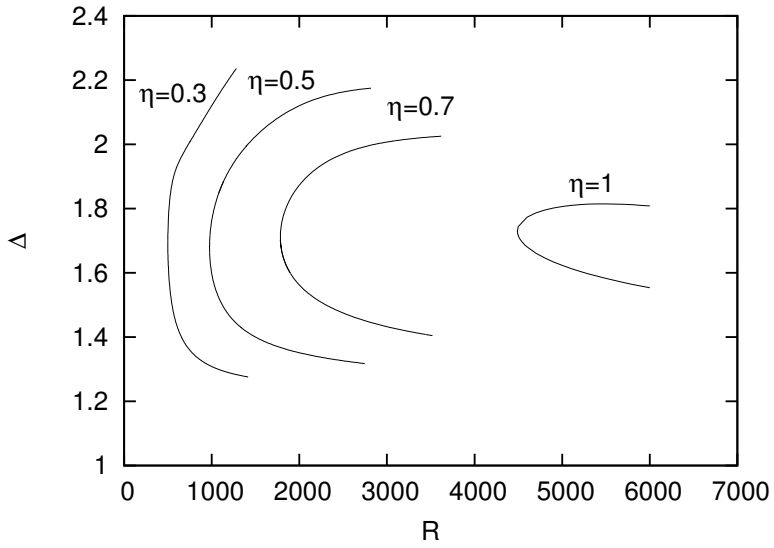

Figure 6.3: The SCF-PCF homotopy of the single-layer class $\mathcal{M}$ solutions for $(\alpha, \beta) = (0.75, 0.82)$. The range of truncation level $(L, M, N) \in [25, 40] \times [6, 16] \times [10, 26]$ is used.

double-layered, half gap sized vortices. Mathematically, this roll structure could change along the solution branch without bifurcation. However, it seems that the roll structure is roughly preserved as long as there is no rapid change of the branch shape compared to the overall. Indeed, the two branches of class $\mathcal{M}$ solutions in figure 6.1 reconnect when the axial wavenumber α is changed as we saw in figure 5.9. We confirm the flow structures change rapidly only in the vicinity of the reconnection point where the branches turn sharply.

The reconnection of these solution branch does not occur at higher values of η because the homotopy behavior with changing η for these two solution types differs. As shown in figure 6.3 the minimum Reynolds number for which the single-layer mode exists increases with η. In the PCF limit, as can be seen also from figure 6.6 (d), its saddle-node point is at $R = O(10^3)$ which is ten times higher than other known three-dimensional finite-amplitude solutions of PCF. On the other hand, the saddle-node point of the double-layer mode is relatively invariant to the change in η, and R remains low in the PCF limit. Figure 6.4 shows the variation of wall shear Δ as a function of α and β together with the existence region given by the projection onto the $\alpha - \beta$ plane for four different values of η under $R = 400$. The azimuthal wavenumber m_0 takes integer values along the two-dot chain lines as are shown in the lower projections. At $\eta = 0.3$, we thus find that solutions exist

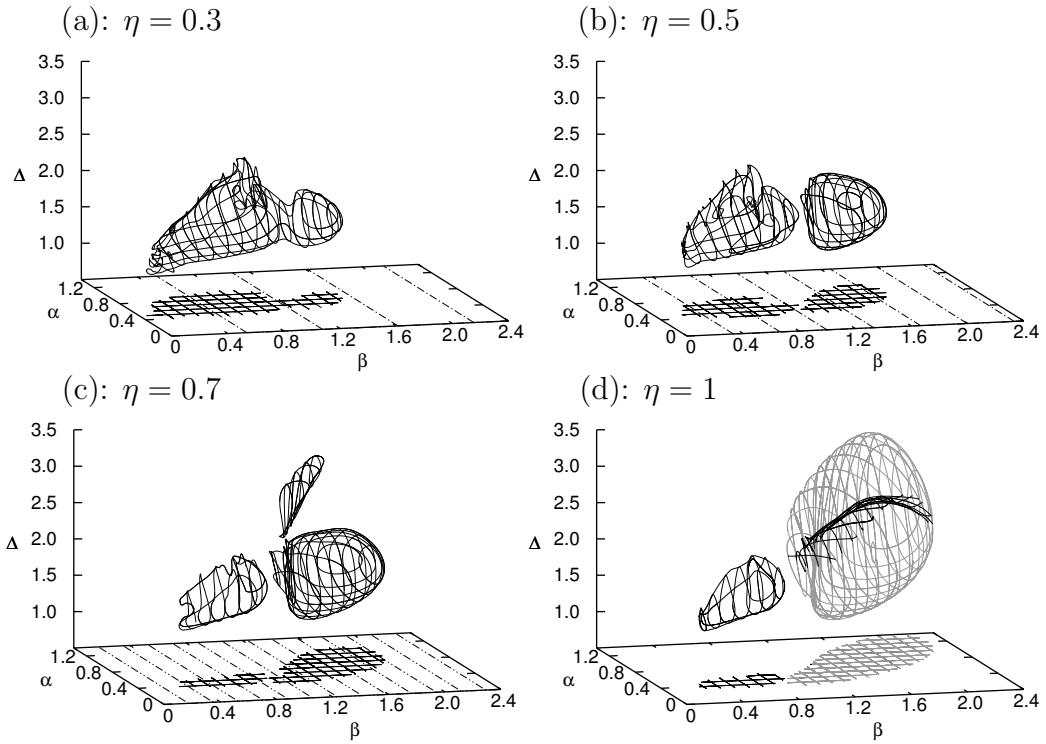

Figure 6.4: The SCF-PCF homotopy of the double-layer solutions for $R = 400$. The truncations used are within the range of $(L, M, N) \in [23, 30] \times [12, 30] \times [12, 22]$. The black/grey lines represent the class $\mathcal{M}/\mathcal{M}^*$ solutions.

only for $m_0 = 1, 2$. When η becomes larger than 0.3, the solution bubble separates into two bubbles. The bubble that exists for smaller values of β smoothly connects to PCF with only a small change in its shape. We call this solution the double-layer mode A. The homotopy of the solution bubble that exists for larger values of β is also smooth, but it joins at $\eta = 1$ with a third bubble which abruptly appears between $\eta = 0.5$ and 0.7. The upper and lower surfaces of the resultant large bubble at $\eta = 1$ is made of these two different bubbles. The contact surfaces of the two bubbles which was facing each other become a membrane forming in the large bubble at $\eta = 1$. At this planar limit, the outer surface of the solution bubble retrieves the steady symmetry, $\sigma_{\xi y}$, so that it belongs to class $\mathcal{M}^*$, whereas the solution membrane (i.e. the contact surface of the joined bubbles) remains of class $\mathcal{M}$. We call these solutions, the membrane and outer joined bubble solutions, double-layer mode B solutions. The exotic bifurcation scenario of this solution family accompanying the imperfection of the symmetry of the system around $\eta = 1$ will be examined in detail in subsection 6.1.2. Figure 6.5 shows the existence region of the solutions in the PCF limit. We can see the existence regions of the Nagata solution and

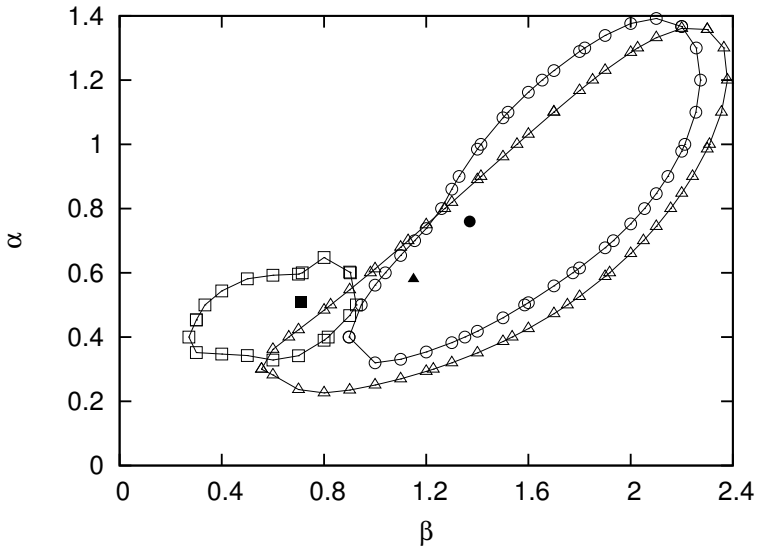

Figure 6.5: The open symbols chained by the solid lines represent the existence region of the PCF solutions at $R = 400$ in the wavenumber plane. The closed symbols show the optimal wavenumber pair. Triangle: the class $\mathcal{S}^*$ Nagata solution, square: the class $\mathcal{M}$ double-layer solution A, circle: the class $\mathcal{M}^*$ double-layer solution B.

double-layer mode B almost overlap whereas a larger spanwise structure, i.e. smaller β, is preferred for the double-layer mode A. With decreasing R each of the existence regions shrinks to a single point in the wavenumber plane and then disappears. As in the previous section, we term this special parameter set (R, α, β), at which R attains its global minimum for the particular solution, as the optimum parameter set. Using the optimum wavenumber pair, the bifurcation diagrams of all the PCF solutions obtained are summarized in figure 6.6. We can see the double-layer mode A has class $\mathcal{M}$ upper- and lower-branch solutions corresponding to the upper and lower surfaces of the bubble respectively, while the double-layer mode B has class $\mathcal{M}^*$ upper and lower branches, and a bifurcating class $\mathcal{M}$ solution branch corresponding to the upper and lower surfaces of the outer bubble, and the inner membrane respectively. From these properties, it is found that the $\mathcal{M}^*$ double-layer mode B coincides to known mirror-symmetric solutions (Itano & Generalis 2009 and EQ7 and EQ8 of Gibson *et al.* 2009, earlier can be found in Schmiegel 1999's low resolution result) whereas the $\mathcal{M}$ double-layer mode B, the single-layer mode and the double-layer mode A represent solutions previously unreported in the literature. We can see from the axial averaged flow field of these solutions (figure 6.7) that the single- and double-layer properties are preserved along the PCF-SCF homotopy. We can also see that the Nagata solution is

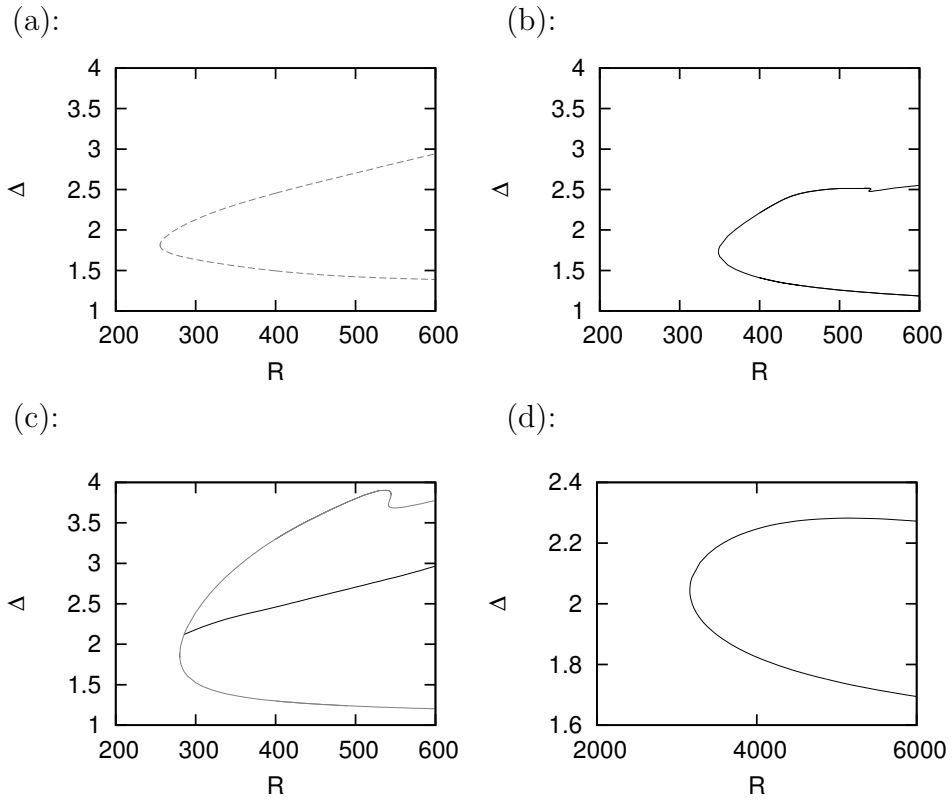

Figure 6.6: The bifurcation diagram for the PCF solutions with the optimum wavenumber pairs. (a): Nagata solutions ($(L, M, N) = (20, 10, 12)$, the optimum parameter set is $(R, \alpha, \beta) = (255.4, 0.58, 1.15)$), (b): Double-layer solutions A ($(L, M, N) = (25, 12, 22)$, the optimum optimum parameter set is $(R, \alpha, \beta) = (348.5, 0.51, 0.71)$), (c): Double-layer solutions B ($(L, M, N) = (23, 12, 16)$, the optimum optimum parameter set is $(R, \alpha, \beta) = (280.1, 0.75, 1.37)$), (d): Single-layer solutions ($(L, M, N) = (40, 6, 26)$, the optimum optimum parameter set is $(R, \alpha, \beta) = (3164.5, 0.74, 1.09)$). The grey dashed, grey solid and black solid lines represent the class $\mathcal{S}^*$, $\mathcal{M}^*$ and $\mathcal{M}$ solutions, respectively.

of a single-layer type structure.

Similar bubble separation/unification also occurs for the SCF-PCF homotopy path of class $\mathcal{S}$ solutions, but we do not show the details here because the bubbles have very complex shape at small η (c.f. figure 5.9). We only say here that the class $\mathcal{S}$ solutions continued from the Nagata solution to SCF do not always retrieve steady type symmetry, $\mathcal{S}^*$, when returned to PCF. For example, if η is decreased to 0.36 in figure 5.9, the branch is reconnected to another branch around $R = 350$. The new branch obtained by the reconnection instead return to the travelling-wave solution discovered by Nagata (1997). (These latter solutions are class $\mathcal{S}$, with optimum $(R, \alpha, \beta) = (315.2, 0.70, 1.36)$; we confirm these solutions are the same solution as TW2 and TW3 of Gibson *et al.* 2009).

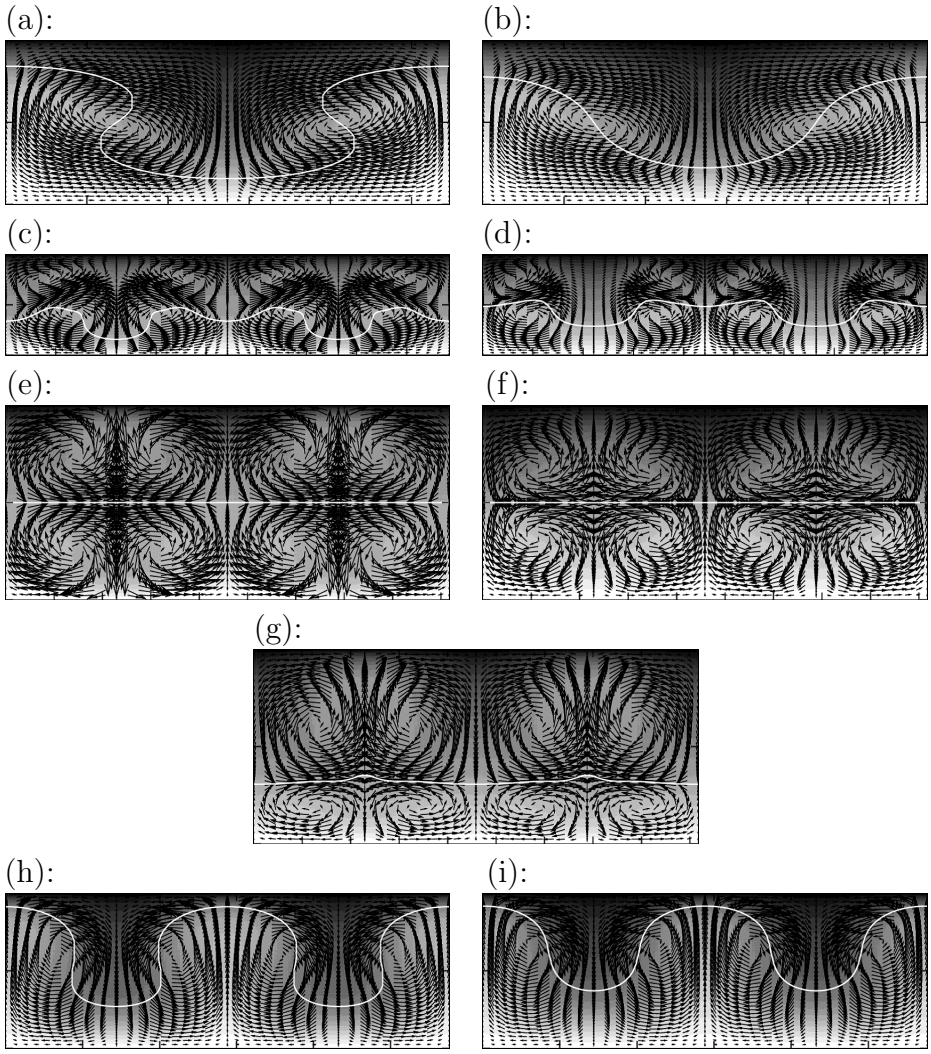

Figure 6.7: Same plot as figure 6.2 but for the PCF solutions at $R = 400$ for (a)–(g), at $R = 4000$ for (h) and (i). The optimal wavenumbers are used. The horizontal axis represents spanwise coordinate $z \in [0, 2\pi/\beta]$, and the vertical axis represents wall-normal coordinate $y \in [-1, 1]$. (a): the upper-branch and (b): the lower-branch Nagata solution; (c): the upper-branch and (d): the lower-branch double-layer solution A; (e): the upper-branch, (f): the lower-branch and (g): the bifurcating travelling-wave double-layer solution B; (h): the upper-branch and (i): the lower-branch single-layer solution.

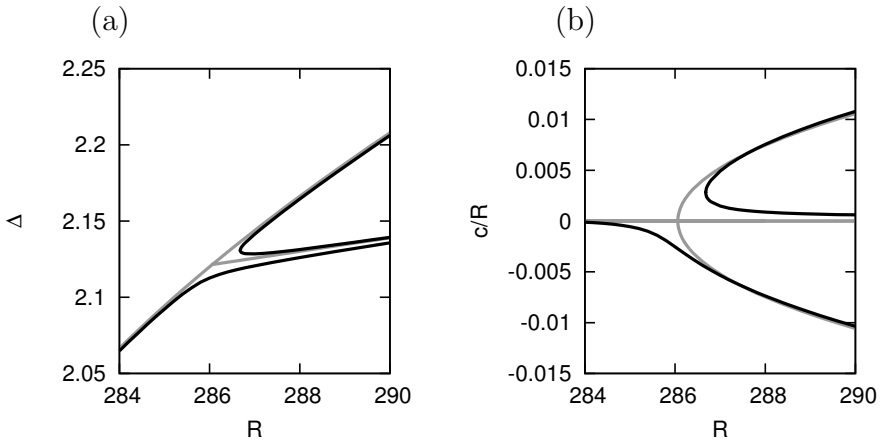

Figure 6.8: The imperfect bifurcation of the double-layer solution B in PCF when a plane Poiseuille flow component, R_p, is added for wavenumbers $(\alpha, \beta) = (0.75, 1.37)$. The measures of the nonlinearity are (a): the momentum transfer Δ and (b): the wavespeed c. The curves in grey and black correspond to $R_p = 0$ and $R_p = 0.1$, respectively.

Recall that we also observed the unification of the solution bubbles of class $\mathcal{M}$ solutions around similar values of η. The typical unification of solution bubbles around $\eta = 0.3$ can be considered to be due to the introduction of the inner cylinder, which begins to affect the flow structure when its diameter is comparable to the gap at this particular radius ratio.

6.1.2 Double structure of the travelling-wave solution branches

This subsection examines the bifurcation nature of class $\mathcal{M}$ double-layer solution B at $\eta \approx 1$. As we saw in figures 6.4 and 6.6 (c), there exist steady upper- and lower-branch solutions, here denoted by $\mathbf{X}_{EQ}$, and two bifurcating travelling-wave solution branches, here denoted by $\mathbf{X}^{+}_{TW}$ and $\mathbf{X}^{-}_{TW}$, at $\eta = 1$. The two travelling-wave solution branches which are overlapped in figure 6.6 (c), satisfy cross-parity $\sigma_{\xi y}\mathbf{X}^{\pm}_{TW} = \mathbf{X}^{\mp}_{TW}$ as long as the system has $\sigma_{\xi y}$ symmetry. Where $\pm$ refers sign of their non-zero wavespeeds relative to the steady solutions.

In order to examine the qualitative change of the bifurcation due to the imperfect symmetry of the system, which must resolve the degeneracy of $\mathbf{X}^{\pm}_{TW}$, it is convenient to consider a simpler situation, i.e. we perturb antisymmetric PCF profile by adding a symmetric

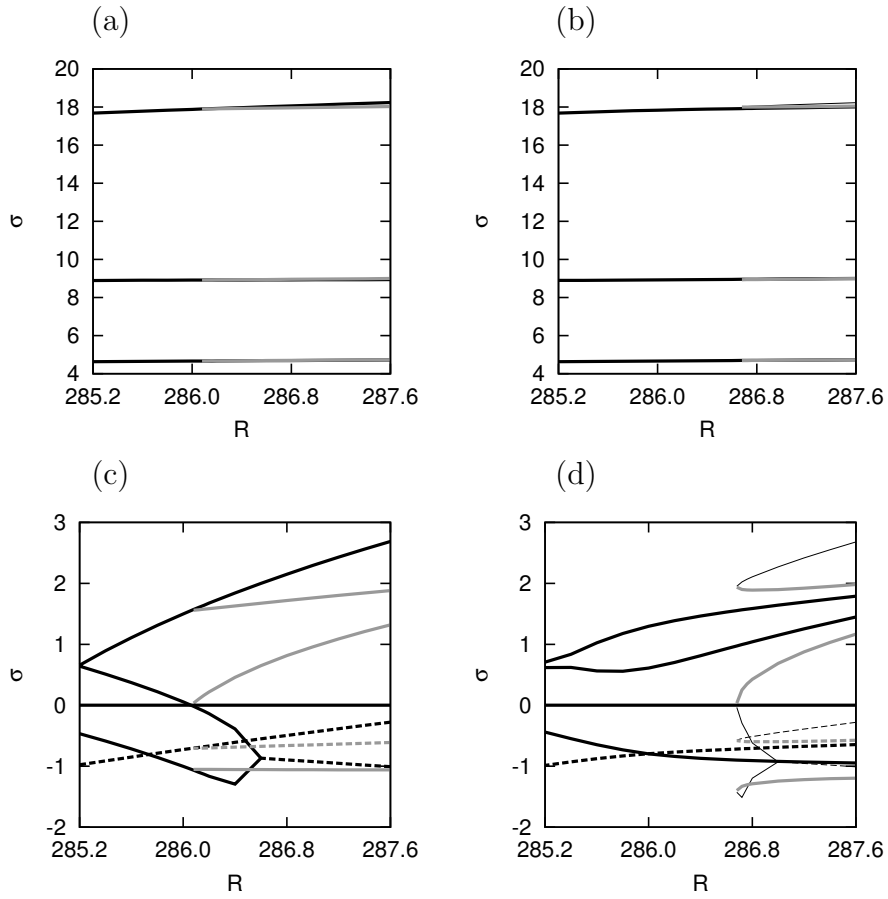

Figure 6.9: The real part of the growth rate of a perturbation for the double-layer solution B with $(\alpha, \beta) = (0.75, 1.37)$. The three largest real parts for $R_p = 0$ and $R_p = 0.1$ are shown in (a) and (b), respectively. The next largest real parts (from the fourth to the tenth) for $R_p = 0$ and $R_p = 0.1$ are shown in (c) and (d), respectively. The figures include two growth rates $s = \sigma + \mathrm{i}\gamma \equiv 0$ for all R, which result from the invariance of the solution to infinitesimal translations. The solid/dashed curves imply that σ is real/complex conjugate, respectively. For $R_p = 0$, the black and grey curves correspond to $\mathbf{X}_{EQ}$ and $\mathbf{X}^{\pm}_{TW}$, respectively. For $R_p = 0.1$, the black thick ($285.2 \leq R \leq 287.6$), black thin ($286.6 \leq R \leq 287.6$) and grey thick ($286.6 \leq R \leq 287.6$) curves correspond to travelling-wave solutions with negative, smaller positive and larger positive wavespeeds, respectively.

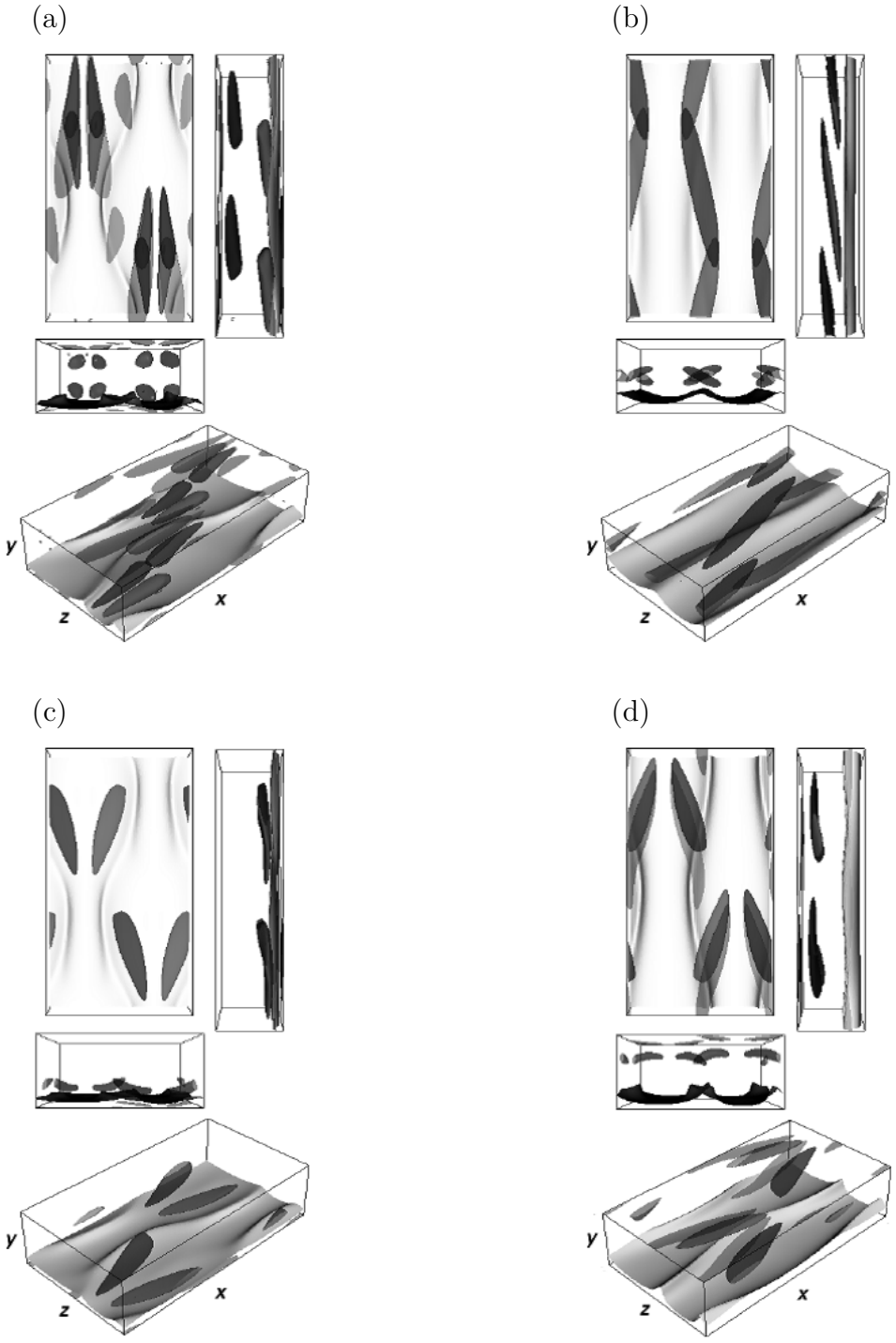

Figure 6.10: Isosurfaces of the streamwise velocity component U (grey) and the streamwise vorticity component ω_x (light grey: positive and dark grey: negative) of for the double-layer solution B with wavenumbers $(\alpha, \beta) = (0.75, 1.37)$ at $R = 400$. Isosurfaces is at $U = 120$ and (a): $|\omega_x| = 300$ for $\mathbf{X}_{EQ}$ upper-branch, (b): $|\omega_x| = 100$ for $\mathbf{X}_{EQ}$ lower-branch, (c): $|\omega_x| = 250$ for $\mathbf{X}^{+}_{TW}$ and (d): $|\omega_x| = 250$ for $\mathbf{X}^{-}_{TW}$. The isosurface of the streamwise velocity component U at $U = -120$ in each case is located near the boundary $y = 1$ symmetrically to the isosurface at $U = 120$, but not displayed for clarity.

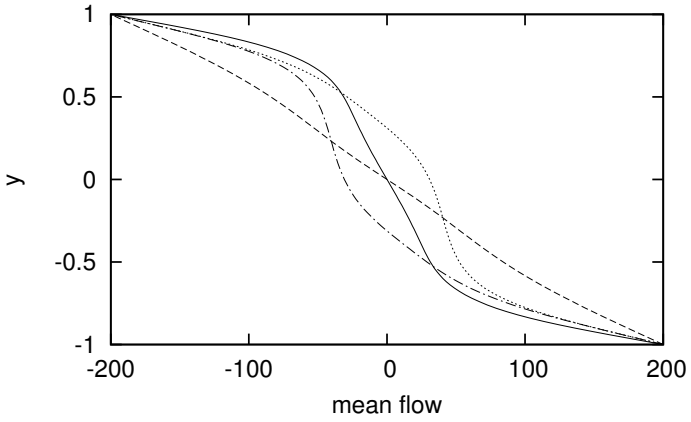

Figure 6.11: The mean flow $\overline{U}$ of $\mathbf{X}_{EQ}$ and $\mathbf{X}_{TW}^{\pm}$ with wavenumbers $(\alpha, \beta) = (0.75, 1.37)$ at $R = 400$ for the double-layer solutions B. The solid curve: the upper-branch steady solution $\mathbf{X}_{EQ}$. The dashed curve: the lower branch steady solution $\mathbf{X}_{EQ}$. The dash-dotted curve: the travelling-wave solution $\mathbf{X}_{TW}^{+}$. The dotted curve: the travelling-wave solution $\mathbf{X}_{TW}^{-}$.

Poiseuille flow component so that the basic flow takes the form of

$$U_B = -Ry/2 + R_p(1 - y^2). \tag{6.1}$$

Where R_p is the second Reynolds number associated with a pressure gradient in the Couette flow direction which causes symmetry breaking of $\sigma_{\xi y}$ symmetry of the system as in the case of $\eta < 1$.

Figure 6.8 shows the momentum transfer, Δ, and the wavespeed, c, for $\mathbf{X}_{EQ}$ and $\mathbf{X}_{TW}^{\pm}$ with $(\alpha, \beta) = (0.75, 1.37)$, which is the magnified portion of figure 6.6 (c), for the cases $R_p = 0$ and 0.1. As R_p is increased from zero, the pitchfork bifurcation at $R = R_B = 286.2$ for $R_p = 0$ is destroyed due to the symmetry breaking of the system as in the case of $\eta < 1$. The section of the $\mathbf{X}_{EQ}$ branch for $R < R_B$ and the travelling-wave branch with $c \leq 0$ form a smooth branch with negative wavespeeds whereas the section of the $\mathbf{X}_{EQ}$ branch for $R > R_B$, on the other hand, forms a new branch with a saddle-node point at R slightly larger than R_B by connecting with the travelling-wave branch with $c \geq 0$.

In order to further elucidate the bifurcation structure, the stability of $\mathbf{X}_{EQ}$ and $\mathbf{X}_{TW}^{\pm}$ is analyzed when $R_p = 0$ and $R_p = 0.1$ near $R = R_B$. The strategy to obtain the growth rate σ for these solutions is the same as in section 5.3. Figure 6.9 shows the results of

the stability analysis where (a) and (c) correspond to the unperturbed case with $R_p = 0$ whereas (b) and (d) to the perturbed case with $R_p = 0.1$. For both cases, the three largest real parts are shown in the upper parts of the figures (figures 6.9 (a) and (b)). From these figures it is clear that all the solution branches are unstable. The next largest real parts (from the fourth to the tenth) are shown in the lower parts of the figures (figures 6.9 (c) and (d)). As shown in figure 6.9 (c) for $R_p = 0$ the fifth largest real part of the growth rate for $\mathbf{X}^{EQ}$ changes from positive to negative as R is increased. It crosses zero at $R = R_B = 286.2$, giving rise to the bifurcation of the travelling-wave solutions, $\mathbf{X}^{\pm}_{TW}$. The fifth largest real part of the growth rates for $\mathbf{X}^{+}_{TW}$ and $\mathbf{X}^{-}_{TW}$, which are degenerate in figure 6.9, starts from zero at this point and increases with R. Hence these eigenvalues crossing zero are purely real, and bifurcating travelling-wave solutions must have zero wavespeed at the bifurcation point. However, away from the bifurcation point the bifurcating solutions are travelling waves because the associated eigenfunction breaks steady symmetry (i.e. $\sigma_{\xi y}$).

For perturbed case $R_p = 0.1$, we can see from figure 6.9 (d) that for the travelling wave branch with a negative wavespeed, which are originally $\mathbf{X}^{-}_{TW}$ and $\mathbf{X}_{EQ}$, the sign of the growth rates of the linear disturbance are unchanged with changing R, implying no bifurcations from this branch. In contrast, near $R = 286.6$ the fifth largest real parts of the growth rate for the two travelling-wave branches with positive wavespeeds, which are originally $\mathbf{X}^{+}_{TW}$ and $\mathbf{X}_{EQ}$, join together at zero creating a saddle-node bifurcation.

Isosurfaces of the total streamwise velocity component U and the streamwise vorticity component ω_x for these solutions with $(\alpha, \beta) = (0.75, 1.37)$ at $R = 400$ are plotted in figure 6.10. All of the plots are presented for a domain comprising the full height of the channel and one period in both the streamwise and spanwise directions. For all plots, high speed streaks corresponding to the ridges of the isosurface of $U = 120$ are located near the boundary at $y = -1$. High-speed streaks with opposite sign are also located near the boundary at $y = 1$, but these are not plotted for clarity. It can be seen that there are two streaks varying in a varicose way in the streamwise direction, due to the mirror symmetry. For the upper-branch of $\mathbf{X}_{EQ}$, we can see strong streamwise vortices of equal strength situated near the boundaries at $y = \pm 1$, whereas they are located near the

midplane $y = 0$ for the lower-branch of $\mathbf{X}_{EQ}$. Strong quasi-streamwise vortices are located in a neighbourhood of the bottom boundary $y = -1$ for $\mathbf{X}^{+}_{TW}$, whereas, consistent with the cross-parity, they are found near the upper boundary $y = 1$ for $\mathbf{X}^{-}_{TW}$.

The total mean flow $\overline{U}$ shown in figure 6.11 also reflects the differing symmetries. It can be seen that mean flows of both the upper- and lower-branch of the $\mathbf{X}_{EQ}$ are anti-symmetric about the midplane $y = 0$, whereas those of the travelling-wave solutions, $\mathbf{X}^{+}_{TW}$ and $\mathbf{X}^{-}_{TW}$, are asymmetric.

6.2 Towards pipe flow

We also show that class $\mathcal{M}$ solution in SCF can be continued to PF. In this section the flow is assumed to be driven by an axial pressure gradient together with the movement of the inner cylinder. As a consequence, the basic flow profile $\mathbf{U}_B = U_B \mathbf{e}_x$ is obtained by

$$U_B(r) \;=\; R\frac{\ln(r/r_b)}{\ln \eta} + R_p \frac{r^2 - r_b^2 - 2r_p^2 \ln(r/r_b)}{r_p^2 - r_b^2 - 2r_p^2 \ln(r_p/r_b)}, \tag{6.2}$$

and can be seen to depend on R, the Reynolds number induced by sliding, R_p, the Reynolds number induced by the axial pressure gradient, and η, the radius ratio. This system is often refereed to as annular Couette-Poiseuille flow in the case of non-zero R and R_p. Note that if $R = 0$, i.e. the case called annular Poiseuille flow, U_B takes the largest value R_p at $r = r_p = r_b\sqrt{\frac{\eta^2-1}{2\ln\eta}}$. The definition of R_p is consistent with the basic flow expressed by (6.1).

With this basic flow profile we next consider the limit as $\eta \to 0$ in which the basic flow coincides with that of PF

$$U_B(r) = R\frac{r_b^2 - r^2}{4r_m}, \tag{6.3}$$

together with axial pressure gradient

$$\frac{R_p}{R} = \Pi(\eta) = \frac{r_p^2 - r_b^2 - 2r_p^2 \ln(r_p/r_b)}{r_b^2(\eta^2 - 1)}. \tag{6.4}$$

However, the infinitesimally thin inner cylinder still has a non-negligible effect on the disturbance in this limit. We discuss how to eliminate this effect in the next subsection.

6.2.1 Eliminating process of inner cylinder

Firstly, we examine the analytic condition at the centreline $r = 0$ which is needed for pipe flow calculation. Let us consider the circular domain in Cartesian coordinates,

$$B \equiv \{(x_1, x_2) \in \mathbb{R}^2 : x_1^2 + x_2^2 \leq r_b^2\} \tag{6.5}$$

and cylindrical coordinates,

$$B^\circ \equiv \{(r, \theta) \in \mathbb{R}_{\geq 0} \times \mathbb{R} : r \in [0, r_b], \theta \in [0, 2\pi)\}. \tag{6.6}$$

Because of the singularity at $r = 0$, $C^\infty(B^\circ)$ does not ensure $C^\infty(B)$. Here we say that $f(r, \theta) \in B^\circ$ is an analytic function if $f \circ \varrho^{-1}(x_1, x_2) \in C^\infty(B)$ introducing inverse polar mapping

$$\begin{aligned} \varrho : \mathbb{R}^2 &\rightarrow \mathbb{R}_{\geq 0} \times \mathbb{R}/(2\pi\mathbb{Z}) \\ (x_1, x_2) &\mapsto (\sqrt{x_1^2 + x_2^2}, \arctan(x_2/x_1)). \end{aligned} \tag{6.7}$$

We approximate f by using a truncated series in a usual spectral method.

$$f(r, \theta) \approx f_{LM}(r, \theta) = \sum_{l=0}^{L} \sum_{m=-M}^{M} X_{lm} \mathscr{P}_l^m(r) e^{\mathrm{i}m\theta} + \text{c.c.}, \tag{6.8}$$

where $\mathscr{P}_l^m(r)$ is lth-order polynomial basis function. To ensure the analyticity at the centreline of $f_{LM}(r, \theta)$ for any truncated sum, each function $\mathscr{P}_l^m(r)e^{\mathrm{i}m\theta}$ should be $C^\infty(B)$. We can paraphrase this analyticity condition to the condition for $\mathscr{P}_l^m(r)$ as follows (see Eisen *et al.* 1991 for example).

Theorem 2. The following three statements are equivalent:

(i): $\mathscr{P}_l^m(r)e^{\mathrm{i}m\theta} \in C^\infty(B)$, i.e. is analytic,

(ii): $\mathscr{P}_l^m(r)e^{\mathrm{i}m\theta}$ can be rewritten as a polynomial in x_1 and x_2,

(iii): $\mathscr{P}_l^m(r)$ satisfies the following conditions (a) and (b):

(a, parity condition) : m is odd (even) $\Rightarrow$ $\mathscr{P}_l^m(r)$ is odd (even) function,

(b, order condition) : minimum order of $\mathscr{P}_l^m(r) \geq |m|$.

One basis set which can satisfy the above conditions is the Zernike basis (Zernike 1934),

$$\mathscr{Z}_l^m(r) = \sum_{s=0}^{(l-m)/2} (-1)^s \frac{(l-s)!}{s!(\frac{m+l}{2}-s)!(\frac{l-m}{2}-s)!} r^{l-2s}. \tag{6.9}$$

Note that the above conditions represent the analytic condition for a scalar function. Therefore we further need the conditions for the potentials so that the velocity field is to be analytic in cylindrical domain $D \equiv \{(x_1, x_2) \in B, x_3 \in [0, L_3]\}$.

Theorem 3. $\phi/r, \psi/r, \overline{v}/r, \overline{w} \in C^\infty(D) \Rightarrow$ velocity field $[u, v, w]^T$ given by (2.8) can be rewritten as a $C^\infty(D)$ vector field in Cartesian coordinates.

The proof of this theorem is straightforward. Let us denote velocity field in Cartesian coordinates $[u_1, u_2, u_3]^T = \Theta[v, w, u]^T$ by using the orthogonal transformation

$$\Theta \equiv \begin{bmatrix} \cos\theta & -\sin\theta & 0 \\ \sin\theta & \cos\theta & 0 \\ 0 & 0 & 1 \end{bmatrix}.$$

Unit vectors in the x_1, x_2, x_3 directions are obtained by$[\mathbf{e}_{x_1}, \mathbf{e}_{x_2}, \mathbf{e}_{x_3}] = [\mathbf{e}_r, \mathbf{e}_\theta, \mathbf{e}_x]\Theta^{-1}$. If we write the curl operator in matrix form for Cartesian and cylindrical coordinate as

$$A \equiv \begin{bmatrix} 0 & -\partial_{x_3} & \partial_{x_2} \\ \partial_{x_3} & 0 & -\partial_{x_1} \\ -\partial_{x_2} & \partial_{x_1} & 0 \end{bmatrix}, \qquad A^\circ \equiv \begin{bmatrix} 0 & -\partial_z & r^{-1}\partial_\theta \\ \partial_z & 0 & -\partial_r \\ -r^{-1}\partial_\theta & \partial_r + r^{-1} & 0 \end{bmatrix}$$

respectively, then we have $A = \Theta A^{\circ} \Theta^{-1}$. Therefore

$$
\begin{aligned}
[\mathbf{e}_r, \mathbf{e}_\theta, \mathbf{e}_x] \begin{bmatrix} v \\ w \\ u \end{bmatrix} &= [\mathbf{e}_r, \mathbf{e}_\theta, \mathbf{e}_x] \left\{ A^{\circ} A^{\circ} \begin{bmatrix} \phi \\ 0 \\ 0 \end{bmatrix} + A^{\circ} \begin{bmatrix} \psi \\ 0 \\ 0 \end{bmatrix} + \begin{bmatrix} 0 \\ \overline{v} \\ \overline{w} \end{bmatrix} \right\} \\
&= [\mathbf{e}_{x_1}, \mathbf{e}_{x_2}, \mathbf{e}_{x_3}] \left\{ AA \begin{bmatrix} x\phi/r \\ y\phi/r \\ 0 \end{bmatrix} + A \begin{bmatrix} x\psi/r \\ y\psi/r \\ 0 \end{bmatrix} + \begin{bmatrix} -y\overline{v}/r \\ x\overline{v}/r \\ \overline{w} \end{bmatrix} \right\}.
\end{aligned}
$$

The terms in curly brackets in the last line equals $[u_1, u_2, u_3]^T$ and this is $C^{\infty}(D)$. The proof is completed.

In view of theorems 2 and 3, each basis function for potentials and mean flows must satisfy the modified parity and the order conditions to assure the analyticity of flow field. However, higher order conditions are not required for the current computations because the centerline is not chosen as a collocation point. Indeed, although many authors use a non-analytic basis to calculate PF (for example, Kerswell and co-workers omit order conditions, whereas Shimizu & Kida (2009) only consider analyticity of scalar potentials), their results seem to be reliable. Hence we can relax the above conditions to the minimum requirement, namely boundary conditions at the centreline. Expressing each basis function Φ_l, Ψ_l, U_l and W_l as a Taylor expansion $\sum_{k=0}^{l} q_k r^k$ and applying the analytic condition to the leading order, we can find these proper boundary conditions at $r = 0$:

$$\Phi_l : q_0 = q_2 = 0 \quad \Rightarrow \quad \Phi_l = \partial_r(\Phi_l/r) = 0 \ \text{ if } m = 0, \tag{6.10}$$

$$\Phi_l : q_0 = q_1 = 0 \quad \Rightarrow \quad \Phi_l = \partial_r \Phi_l = 0 \ \text{ if } m \neq 0, \tag{6.11}$$

$$\Psi_l : q_0 = 0 \quad \Rightarrow \quad \Psi_l = 0, \tag{6.12}$$

$$U_l : q_0 = 0 \quad \Rightarrow \quad U_l = 0, \tag{6.13}$$

$$W_l : q_1 = 0 \quad \Rightarrow \quad \partial_r W_l = 0. \tag{6.14}$$

In order to smoothly transform these conditions to those corresponding to the no-slip

conditions, we consider the linear combination of these boundary conditions at $r = 0$,

$$\begin{cases} (\Phi_l)' = 0 & \text{if } m = 0, \\ (1-\epsilon)(\Phi_l)' - \epsilon(\Phi_l/r)' = 0 & \text{if } m \neq 0, \\ \Phi_l = \Psi_l = U_l = (1-\epsilon)W_l - \epsilon W_l' = 0. \end{cases} \tag{6.15}$$

We can construct a basis which satisfies (6.15) at $r = 0$ and the no-slip conditions at $r = r_b$ by using modified Chebyshev polynomials as

$$\Phi_l(r) = \begin{cases} r(2-r)^2(rT_l(r-1) + \epsilon(-1)^l) & \text{if } m = 0 \\ r(2-r)^2 rT_l(r-1) & \text{if } m \neq 0 \end{cases}, \tag{6.16}$$

$$\Psi_l(r) = r(2-r)T_l(r-1), \tag{6.17}$$

$$U_l(r) = r(2-r)T_l(r-1), \tag{6.18}$$

$$W_l(r) = (2-r)(rT_l(r-1) + \frac{2\epsilon}{2-\epsilon}(-1)^l). \tag{6.19}$$

This expression coincides with the previously used basis if $(\eta, \epsilon) = (0, 0)$, whereas the effect of inner cylinder vanishes if $(\eta, \epsilon) = (0, 1)$.

6.2.2 Resultant homotopy path

The homotopy path from SCF to PF is thus made by the following three procedures:

- (i) : Add an axial pressure gradient to adjust the basic flow to be parabolic.
- (ii) : Consider the limit as $\eta \to 0$.
- (iii) : Eliminate the effect of the inner cylinder by considering the limit as $\epsilon \to 1$.

The last procedure can be done by using basis (6.16)–(6.19).

Note here that at final pipe state, pressure gradient balances the basic flow shear on the outer cylinder, i.e. $U' = U_B' = -R$, and the deviation of Δ from its laminar value is always

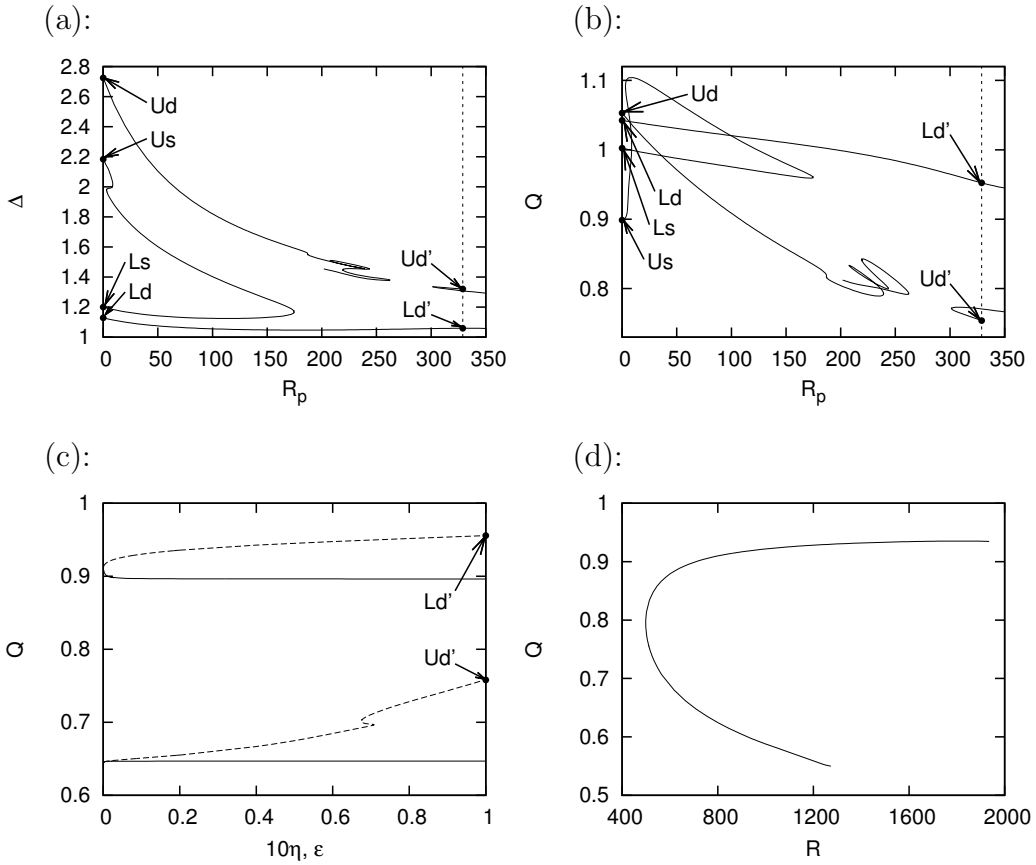

Figure 6.12: The SCF-PF homotopy. (a): The change of momentum transfer Δ, fixing $(\eta, \epsilon, R, m_0, \alpha) = (0.1, 0, 700, 1, 0.75)$. (b): Same result as (a) but for flux Q. (c), the dashed lines: The change of flux Q against η, fixing $(\epsilon, R, R_p, m_0, \alpha) = (0, 700, \Pi R, 1, 0.75)$. (c), the solid lines: The change of flux Q against ϵ, fixing $(\eta, R, R_p, m_0, \alpha) = (0.1, 700, \Pi R, 1, 0.75)$. (d): The bifurcation diagram of PF solution, namely $(\eta, \epsilon, R_p) = (0, 1, \Pi R)$ for $(m_0, \alpha) = (1, 0.73)$. $(L, M, N) = (30, 26, 18)$ are chosen, but for around $(\eta, \epsilon) = (0, 0)$, L is pushed to 50.

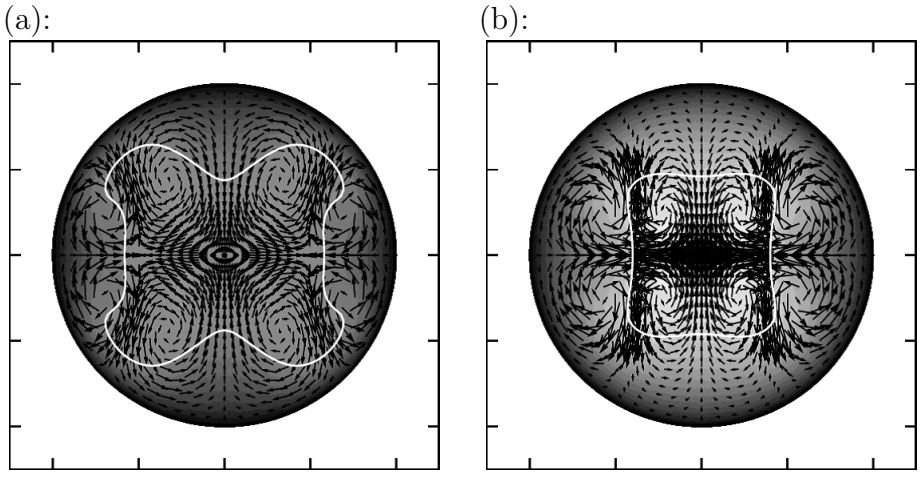

Figure 6.13: Same plot as figure 6.2 but for the PF solutions at $(R, m_0, \alpha) = (1000, 1, 0.73)$. (a): Upper-branch. (b): Lower-branch.

0 for any equilibrated nonlinear solutions. For this reason during the homotopy we instead use the normalized flux

$$Q = \frac{\int_{r_a}^{r_b} (\overline{u} + U_B) r dr}{\int_{r_a}^{r_b} U_B r dr} \tag{6.20}$$

to measure the solutions.

Figure 6.12 (a) shows the variation of momentum transfer Δ during the procedure (i). Solutions marked Ud, Ld, Us and Ls in the figures correspond to those of figure 6.1. The basic flow profile (6.2) becomes parabolic at $R_p = \Pi R$ where the vertical dotted line is traced in the figures. Only the lower branch of the double-layer mode could successfully reach this limit. As can be seen, the upper-branch was followed through a large number of turning points without reaching $R_p = \Pi R$, before computation was abandoned. The upper-branch starting from $R_p = \Pi R$ in the figure is derived by a roundabout route via the lower branch. The same homotopy paths for (i) in terms of Q are shown in figure 6.12 (b). In figure 6.12 (c), the solid lines show the variation of flux Q during the procedure (ii) while the dotted lines represent the variation during the procedure (iii). Figure 6.12 (d) shows the solution branch of the double-layer mode at the final single pipe state obtained by the homotopy. In this figure, we slightly change α to 0.73, to optimize the bulk Reynolds number $R_b = Q \int_{r_a}^{r_b} U_B r dr / 2 r_m$. Our solution takes a minimum bulk Reynolds number at $R_b = 772/4$ which confirms that this solution is the same solution as the M1 found by Pringle & Kerswell (2007). The plot of the structure of this flow provided in figure 6.13 further shows the similarity of our double-layer type solution and M1. As for the PCF-SCF homotopy, this solution preserves its double-layer vortex pattern even in the pipe geometry limit.

On the other hand, we confirm the single-layer mode experiences a turning point before R_p reaches ΠR for various (R, α, β). Though it is known that PF has a single-layer type class $\mathcal{M}$ solution family (labelled N by Pringle *et al.* 2009), this result suggests that the single-layer class $\mathcal{M}$ solution of SCF cannot continue to this class of flows. The branch of class $\mathcal{S}$ solutions of SCF with $m_0 = 1$ is also unable to reach pipe flow by this homotopy

due to the many folds of the branches when the pressure gradient increases.

As a check of the homotopy method exhibited in this section, we confirm that the solutions of pipe flow calculated by basis (6.16)–(6.19) could be recalculated using the following Zernike-based basis,

$$\Phi_l(r) = r(1-r^2)^2 \mathscr{Z}_l^m(r), \tag{6.21}$$

$$\Psi_l(r) = r(1-r^2) \mathscr{Z}_l^m(r), \tag{6.22}$$

$$U_l(r) = r(1-r^2) \mathscr{Z}_l^0(r), \tag{6.23}$$

$$W_l(r) = (1-r^2) \mathscr{Z}_l^0(r). \tag{6.24}$$

Note that the flow field, which is now mapped in $(x, r, \theta) \in [0, 2\pi/\alpha] \times [-1, 1] \times [0, 2\pi/m_0]$, is analytic with this expression. By constructing an initial guess from a least-square interpolation of the solution calculated by basis (6.16)–(6.19), Newton's method successfully converged within a few iterations.

6.3 Self-sustaining mechanism: the forcing from wave to vortex

The aim of this section is to confirm the large Reynolds number asymptotic structure in three-dimensional finite-amplitude solutions we obtained. The possible theory we can apply is vortex-wave interaction (VWI) theory introduced by Hall & Smith (1991), whose quantitative agreement to the Nagata solution has been confirmed recently by Hall & Sherwin (2010).

First, we briefly summarize the VWI theory. For the sake of simplicity, we here use Cartesian coordinates in the narrow-gap limit. Assuming $\alpha \sim O(1)$, the total velocity of

travelling-wave solution propagating in streamwise direction expands as

$$U = A_0 U_0(y,z) + \sum_{m=1}^{\infty} A_m (U_m(y,z) e^{\mathrm{i}m\alpha(x-ct)} + \text{c.c.}), \tag{6.25}$$

$$V = V_0(y,z) + \sum_{m=1}^{\infty} A_m (V_m(y,z) e^{\mathrm{i}m\alpha(x-ct)} + \text{c.c.}), \tag{6.26}$$

$$W = W_0(y,z) + \sum_{m=1}^{\infty} A_m (W_m(y,z) e^{\mathrm{i}m\alpha(x-ct)} + \text{c.c.}) \tag{6.27}$$

where c.c. represents complex conjugate. The Fourier decomposed velocities $[U_m, V_m, W_m](y,z)$ are $O(1)$ for all m and the amplitudes $A_m \in \mathbb{R}_{\geq 0}$, where $\mathbb{R}_{\geq 0}$ is the set of non-negative real numbers, measure the Reynolds number dependence of the order of each terms. In VWI theory, any component which is proportional to the 0th/1st streamwise Fourier mode is referred to as "vortex"/"wave" and plays an important role. In the "vortex" component, U_0 represents the streaks, whereas V_0 and W_0 represent the streamwise rolls. The reason why the same order of amplitudes are used in all three velocity components arises from requiring $[U_m, V_m, W_m](y,z)$ satisfy continuity equation (recall $\alpha \sim O(1)$). However difficulties arise for the 0th terms because the streamwise component, streak, is free from this balance. Bearing in mind U_0 includes the basic flow, the proper choice is $A_0 = R$. We will see from the following streamwise-averaged Navier-Stokes equations (6.29)–(6.32) why the amplitude of roll components should be $O(1)$, thereby deducing so-called R^{-1} scaling of rolls. It is known that for the lower branch solution, the higher the value of m the faster the decay of the amplitude coefficients A_m (Wang *et al.* 2007 for PCF, Viswanath 2009 for PF). With this motivation, we assume $A_m^2 \to 0$ and $A_{m+1}/A_m \to 0$ as $R \to \infty$ for any $m \geq 1$, and the proper expansion of the pressure is determined as follows so that the pressure terms balance the nonlinear terms,

$$P = A_0 G x + P_0(y,z) + A_0 \sum_{m=1}^{\infty} A_m (P_m(y,z) e^{\mathrm{i}m\alpha(x-ct)} + \text{c.c.}) \tag{6.28}$$

where G represents the constant streamwise pressure gradient. Substituting expansions

(6.25)–(6.28) into (2.2) for U, V, W and P and taking the streamwise average,

$$V_0\partial_y U_0 + W_0\partial_z U_0 = G + \partial^2_{yy}U_0 + \partial^2_{zz}U_0 + F_x, \tag{6.29}$$

$$V_0\partial_y V_0 + W_0\partial_z V_0 = -\partial_y P_0 + \partial^2_{yy}V_0 + \partial^2_{zz}V_0 + F_y, \tag{6.30}$$

$$V_0\partial_y W_0 + W_0\partial_z W_0 = -\partial_z P_0 + \partial^2_{yy}W_0 + \partial^2_{zz}W_0 + F_z, \tag{6.31}$$

$$\partial_y V_0 + \partial_z W_0 = 0 \tag{6.32}$$

subject to

$$U_0 - U_B = V_0 = W_0 = 0 \text{ at } y = \pm 1. \tag{6.33}$$

We refer to these equations as the vortex system hereafter. Where $F_x = O(A_0^{-1}A_1^2), F_y = O(A_1^2), F_z = O(A_1^2)$ are forcing terms arising from the nonlinear interaction of the higher harmonics which rapidly decay as R increases. However, we need forcing $\mathbf{F} \equiv F_y\mathbf{e}_y + F_z\mathbf{e}_z$, which is the only energy input to the roll components, to sustain the solution. Therefore we need the "wave" in order to maintain the "vortex". This point can be resolved by examining the Galerkin projection of the first streamwise Fourier mode onto the Navier-Stokes equations (i.e. wave system). The leading part of resultant equation is inviscid linearized Navier-Stokes equations for the fundamental wave, $\mathbf{U}_1$ and P_1, and exhibits a singularity at the critical layer, where U_0 equals to c. This can be found by the following two-dimensional Rayleigh equation

$$\partial^2_{yy}P_1 + \partial^2_{zz}P_1 - \alpha^2 P_1 - 2\frac{\partial_y U_0}{U_0 - c}\partial_y P_1 - 2\frac{\partial_y U_0}{U_0 - c}\partial_y P_1 = 0, \tag{6.34}$$

subject to

$$\partial_y P_1 = 0 \text{ at } y = \pm 1, \tag{6.35}$$

which are equivalent to the wave system derived above (Hall & Horseman 1991). Due to the singularity, the critical layer analysis reveals that $\mathbf{F}$ does not decay at the critical layer in

the manner of the Dirac delta function. The asymptotic form of the force $\mathbf{F}^\infty \equiv (F_y^\infty, F_z^\infty)$ in the limit as $R \to \infty$ can be explicitly calculated as a function of P_1 and U_0. Since the result of the force is manifested in a finite jump at the critical layer, it is convenient to introduce normal and tangential distance (n, s) from the critical layer instead of (y, z). The unit vectors in these directions are obtained in terms of U_0 as $\mathbf{e}_n = -\frac{\partial_y U_0}{\partial_n U_0}\mathbf{e}_y - \frac{\partial_z U_0}{\partial_n U_0}\mathbf{e}_z$ and $\mathbf{e}_s = -\frac{\partial_z U_0}{\partial_n U_0}\mathbf{e}_y + \frac{\partial_y U_0}{\partial_n U_0}\mathbf{e}_z$ where $\partial_n U_0 = \sqrt{(\partial_y U_0)^2 + (\partial_z U_0)^2}$. Here the signs of these vectors are determined so that $\mathbf{e}_n = \mathbf{e}_y$ and $\mathbf{e}_s = \mathbf{e}_z$ when the basic flow is undisturbed. A jump appears in the component of roll velocity tangential to the critical layer at this layer, $\mathscr{V}_0 = \mathbf{e}_s \cdot (V_0\mathbf{e}_y + W_0\mathbf{e}_z)$, as $[\frac{\partial \mathscr{V}_0}{\partial n}]_-^+ \neq 0$ and pressure, P_0, as $[P_0]_-^+ \neq 0$ where $\pm$ signs represent values just above and below the critical layer. As a consequence, the vortex system (6.29)–(6.32), Rayleigh equation (6.34) and $\mathbf{F}^\infty(P_1, U_0)$ comprise a closed system in the limit as $R \to \infty$. Hall & Sherwin (2010) solved this system numerically for PCF.

6.3.1 Detailed physical mechanism of VWI structure

Figures 6.14, 6.15 and 6.16 show the magnitude of the forcing $|\mathbf{F}|$ calculated by (6.30) and (6.31) for the solutions obtained in the previous chapter. The forcing spreads out across the entire layer for the upper-branch solutions because the assumption of the behavior of A_m in the limit as $R \to \infty$ does not hold. By contrast, for all lower-branch solutions, the forcing is confined to the critical layer, where white curves are traced in the corresponding velocity plot figures 6.2, 6.7 and 6.13, in agreement with VWI theory. Further, we can see that the forcing in these cases is always manifested as a pair of strongly forced localize regions on the critical layer. By comparing the pictures of the velocity fields and forcing, we can find that the force is situated near points at which the rolls create outward jets along the critical layer. We can see this picture more clearly in figure 6.18, where the rolls , streaks, and forced regions are superimposed for two typical PCF solutions, the class $\mathcal{S}^*$ Nagata solution and the class $\mathcal{M}^*$ double-layer solution B at sufficiently high R. Further, the plot of the tangential forcing along the critical layer $F_s \equiv \mathbf{e}_s \cdot \mathbf{F}$, figure 6.17, reveals that a pair of forces described above correspond to a positive-negative peak. From the

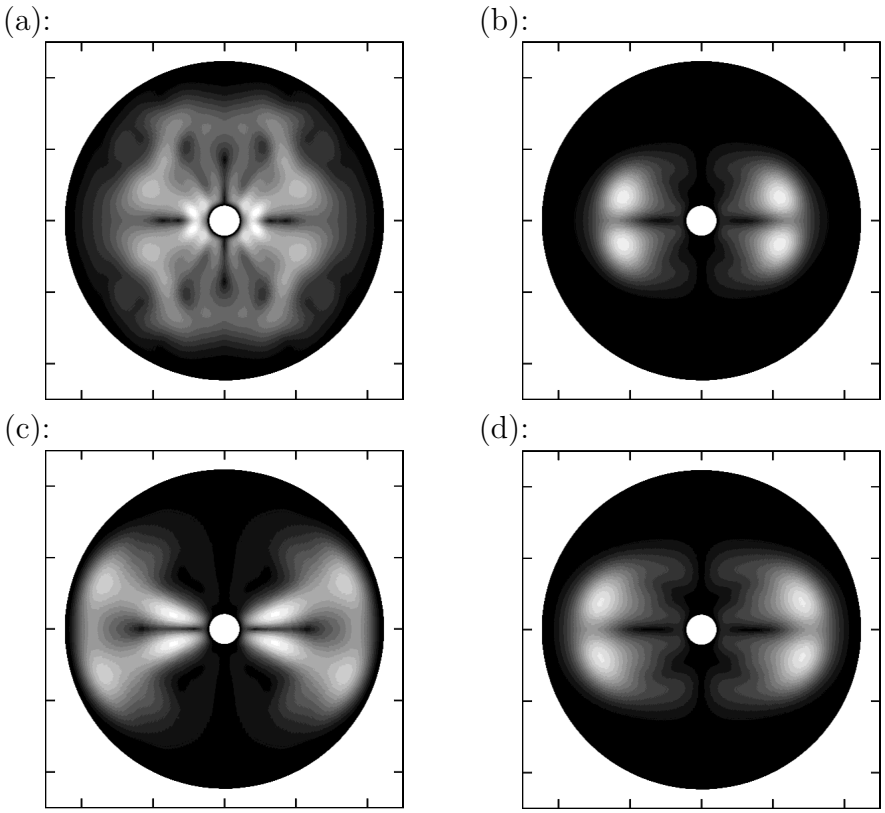

Figure 6.14: The magnitude of the forcing $|\mathbf{F}|$ for the flow fields of the SCF solutions pictured in figure 6.2. Black colour represents zero forcing.

figure, it can also be seen that the shear $\partial_n U_0$ takes a maximum value in the streaks.

The peak of streak shear, the wave forcing at the critical layer and the outward jets of rolls we observed are correspond to the trinity of elements of Waleffe's SSP cycle. Here we reconstruct this cycle, but locally in terms of VWI context, restricting attention to the lower branch class $\mathcal{M}^*$ solution (same solution as figure 6.7 (f)) for simplicity. From the symmetry, we can deduce that the critical layer for this flow is given by $y = 0$. There are therefore no curvature effects of the critical layer which appear in the formulation by Hall & Sherwin (2010). However, in more general cases we note from figures (6.2), (6.7) and (6.13) that curvatures of the critical layer for the lower-branch solutions in typically smaller than that of the upper-branch solutions and, a similar mechanism should exist if the curvature is sufficiently small.

This assumption simplify the asymptotic functional form of the wave forcing at the critical

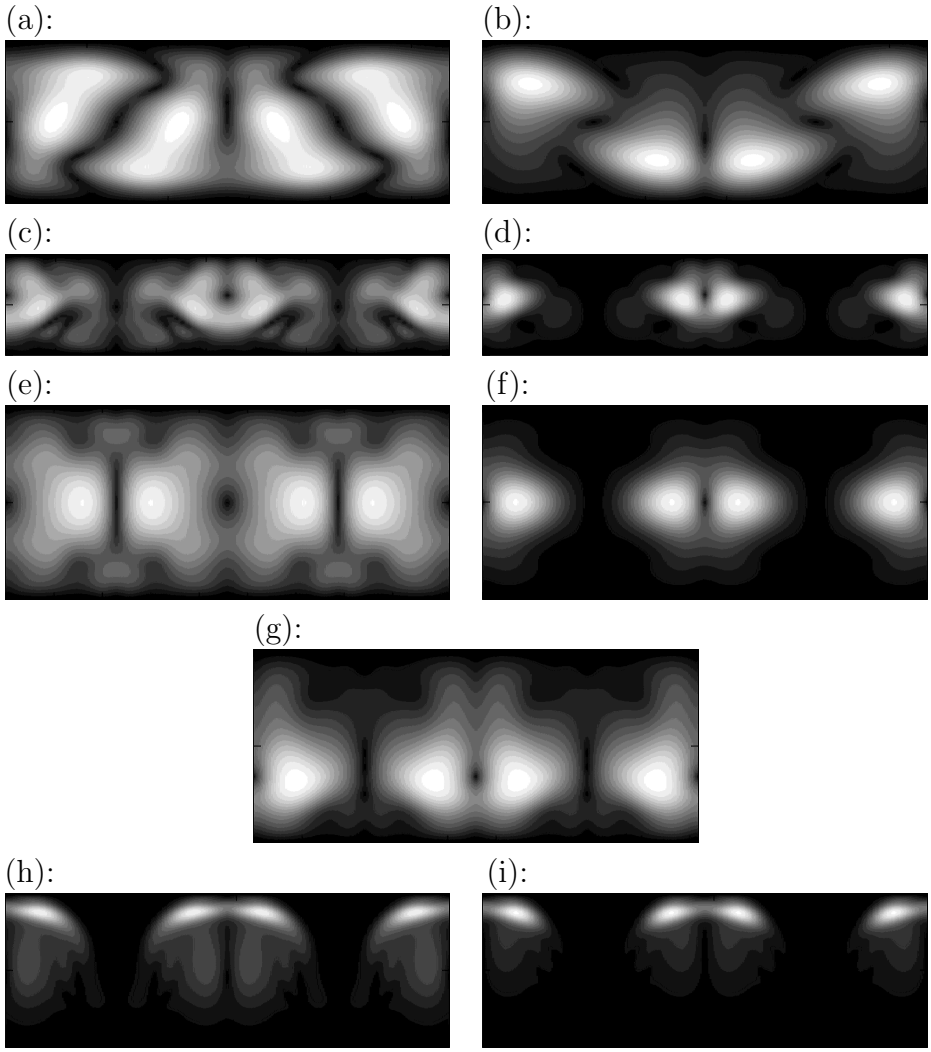

Figure 6.15: Same plots as figure 6.14 but for the flow fields of the PCF solutions pictured in for figure 6.7.

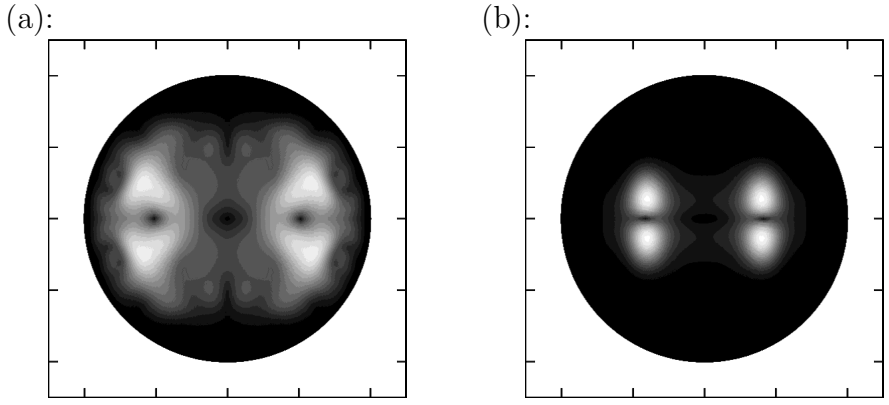

Figure 6.16: Same plots as figure 6.14 but for the flow fields of the PF solutions pictured in figure 6.13.

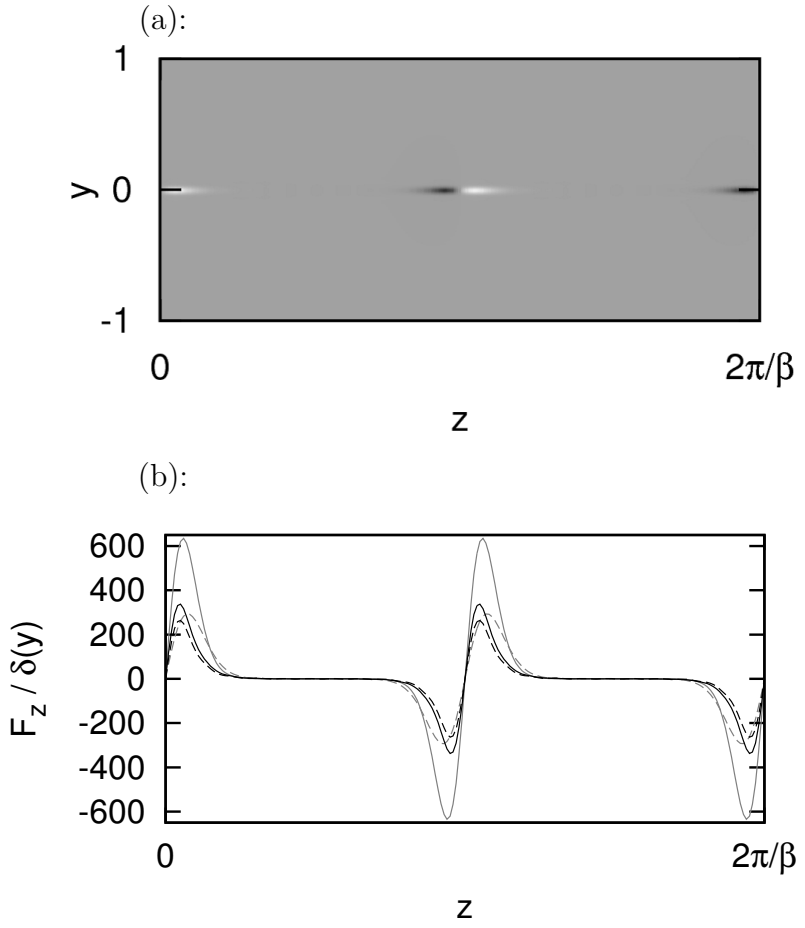

Figure 6.17: The forcing on the rolls at high Reynolds number for a lower branch class $\mathcal{M}^*$ solution of PCF. The optimal wave number pair is used (same as figure 6.7 (f) except for R and resolution $(L, M, N) = (180, 4, 22)$). (a): The bright/dark colour represents positive/negative F_z for $R = 6 \times 10^5$. (b): The forcing at $y = 0$. The solid lines represent exact calculations, $F_z\sqrt{2\pi}R^{-1/3}$, whereas the dashed lines represent VWI calculations, $F_z^{\infty}/\delta(y)$. The grey and black correspond to $R = 6 \times 10^3$ and $R = 6 \times 10^5$, respectively.

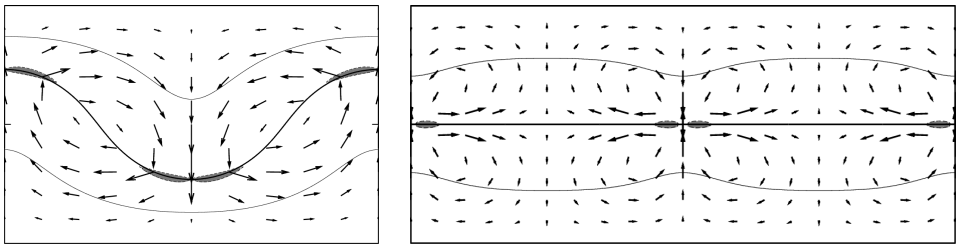

Figure 6.18: The visualization of the solutions of PCF. Left: The lower branch Nagata solution (class $\mathcal{S}^*$) at $(R, \alpha, \beta) = (2 \times 10^5, 1, 2)$ calculated by $(L, M, N) = (120, 5, 50)$. Right: The lower branch double-layer class $\mathcal{M}^*$ solution at $(R, \alpha, \beta) = (2 \times 10^5, 0.75, 1.37)$ calculated by $(L, M, N) = (180, 4, 22)$. The horizontal axis represents spanwise coordinate $z \in [0, 2\pi/\beta]$, whereas vertical axis represents wall-normal coordinate $y \in [-1, 1]$. The thick solid lines show the position of the critical layer $(U_0 - c) = 0$, while the thin solid lines show the position of the iso-contours $(U_0 - c) = 0.5 \times (U_0|_{y=\pm 1} - c)$. The vectors indicate roll velocity (V_0, W_0) and the greyed ovals represent the strongly forced regions where $|\mathbf{F}|$ is greater than the half of its maximum.

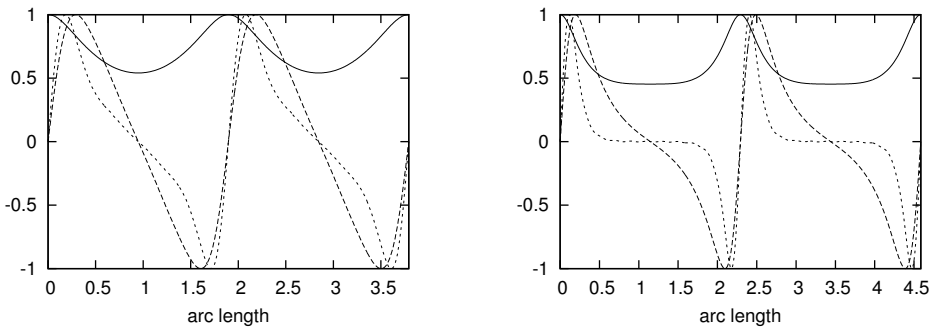

Figure 6.19: The streak shear $\partial_n W_0$ (solid line), the wave force $F_s = \mathbf{e}_s \cdot \mathbf{F}$ (dotted line) and the component of the roll velocity tangent to the critical layer $\mathscr{V}_0 = \mathbf{e}_s \cdot (V_0 \mathbf{e}_y + W_0 \mathbf{e}_z)$ (dashed line). The horizontal axis represents arc length of critical layer from $z = 0$. All dependent variables are normalized by their maximum value. Left / right figures correspond to left / right figures of figure 6.18 respectively.

layer $y = 0$ (see Hall & Sherwin 2010 for the complete expression) as

$$F_y^\infty = 0, \tag{6.36}$$

$$F_z^\infty = -C_1 \partial_z \{(\alpha \partial_y U_0)^{-5/3} |\partial_z P_1|^2\} \delta(y), \tag{6.37}$$

where δ represents the Dirac delta function and $C_1 = 2\pi(2/3)^{2/3}(-2/3)!$. Here A_1 should be $R^{-1/6}$ in order that the effect of the force $A_0^{-5/3} A_0^2 A_1^2 \sim O(1)$. With respect to figure 6.17 (b), in which we plot forcing on the critical layer, it can be seen that the exact expression F_z asymptotes to that of VWI expression F_z^∞ along the critical layer. In this comparison, the delta function $\delta(y)$ in (6.37) is approximated by normalized Gaussian function $e^{-y^2/2a^2}/\sqrt{2\pi}a$ whose width a was chosen to the order of critical layer thickness $R^{-1/3}$, and hence $\delta(0) \approx R^{1/3}/\sqrt{2\pi}$.

Next we examine how the forcing affects rolls. We can calculate the jump in the roll velocity across the critical layer by integrating equation (6.31) from just below to just above the critical layer as

$$-\left[\frac{\partial \mathscr{V}_0}{\partial n}\right]_-^+ = -\left[\frac{\partial W_0}{\partial y}\right]_-^+ = \int_{0-}^{0+} F_z^\infty dy. \tag{6.38}$$

Recalling that W_0 is even function in y by symmetry, if F_z^∞ is positive (negative), W_0 takes a maximum (minimum) at $y = 0$. This dependence of W_0 on F_z^∞ clearly represents that

the positive and negative peaks of the forcing create jets in the roll component. The jets advect fast fluid from the near wall to the vicinity of the critical layer and hence the peak of the streak shear is formed.

Finally we link the peaks of the streak shear and the wave forcing. We just consider a toy problem here since it is not possible to give a proof for the general case. Two assumptions is are made. (i): $y = 0$ represents the critical layer as in the case of $\mathcal{M}^*$ class solution; (ii): the streak profile can be approximated by the simple profile $U_0 - c = -C_2 y \exp(-\lambda z^2/2)$ with real constants C_2 and $\lambda > 0$, with which the streak shear (y derivative of this profile) has single peak at $z = 0$ on the critical layer. With these assumptions, separation of variables $P_1(y, z) = \check{P}_1(y)\hat{P}_1(z)$ is possible. Setting $Z = \sqrt{\lambda}z$, $B(Z) = \exp(Z^2)\hat{P}_1(z)$ satisfies the following Hermite differential equation,

$$\partial_{ZZ}^2 B - 2Z\partial_Z B + 2(k-1)B = 0, \tag{6.39}$$

where k is the separation variable constant. This suggests P_1 (and so the forcing) is given by damped oscillatory waves with strong peaks around the origin. To verify this analysis, we compare the model with the numerical results of figure 6.17. The profiles of the plots in the figure suggests that the non-oscillation case $k = 0$ express in the solution for B to equation (6.39). Consistent with the observation of full solutions, the corresponding solution $\partial_z \hat{P}_1(z) \propto e^{-\lambda z^2}$ implying $P_1(y, z) = -P_1(y, -z)$, i.e. the strong wave is at the axis of shift-reflection symmetry. Substituting U_0 and P_1 of the toy problem into expression (6.37), the forcing takes form

$$F_z^\infty = C_3 z \exp(-7\lambda z^2/6)\delta(y), \tag{6.40}$$

where C_3 is a positive undetermined constant. The forcing (6.40) indeed has positive-negative peaks in the vicinity of the origin. Note that both the class $\mathcal{M}^*$ solution and the model, U_0 expand as $C_2(-y + \lambda y z^2/2) + \cdots$ around the origin. Estimating λ by this comparison for the case of figure 6.17, $R = 6 \times 10^5$, we find expression (6.40) has a peak at 0.112. This is sufficiently close to that of exact calculation, 0.108, and of VWI calculation,

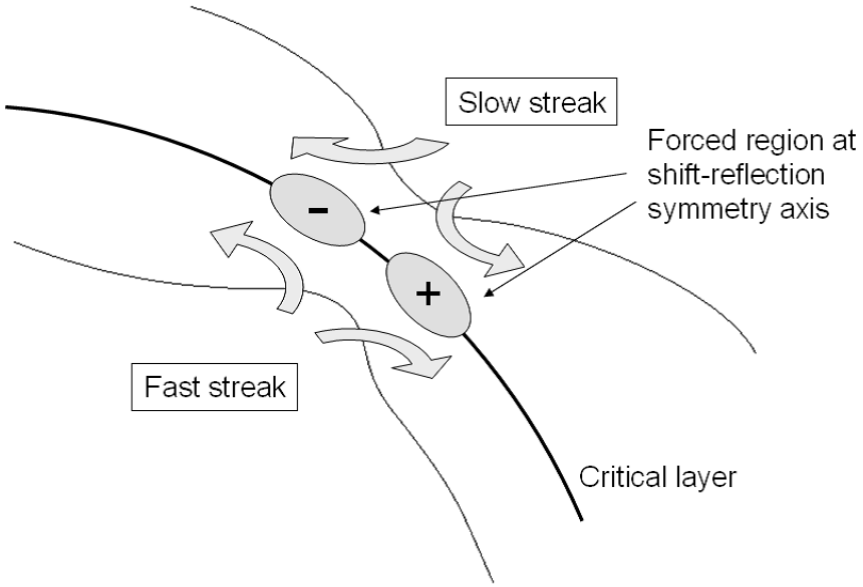

Figure 6.20: The schematic of interaction between the peak of the streak shear (solid lines), the wave forcing at the critical layer (ovals) and the outward jets of the rolls (arrows).

0.109. Also, note that we can prove there can be no forcing if U_0 is independent of the spanwise variable z as follows. Seeking a solution of the form $P_1(y,z) = \check{P}_1(y)\hat{P}_1(z)$ in (6.34), we find that $\hat{P}_1(z) \propto e^{\mathrm{i}C_4 z}$. So assuming $\hat{P}_1(z)$ does not cause exponential growth, i.e. $C_4 \in \mathbb{R}$, it is sufficient to show that $\partial^2_{yy}\check{P}_1 - C_5\check{P}_1 - 2\frac{\partial_y U_0}{U_0-c}\partial_y\check{P}_1 = 0$ has only trivial solutions for some positive constant $C_5 = \alpha^2 + C_4^2$. Multiplying the complex conjugate of $\check{P}_1$ and integrating between the walls, we find

$$\int_{-1}^{1} \frac{C_5|\check{P}_1|^2 + |\partial_y\check{P}_1|^2}{|U_0-c|^2}dx = \left[\frac{\partial_x|\check{P}_1|^2}{|U_0-c|^2}\right]_{-1}^{1} = 0. \tag{6.41}$$

Only $\check{P}_1 \equiv 0$ satisfies this equation. Similar arguments also hold for the cylindrical case, because the Rayleigh equation (6.34) leads to $\partial^2_{rr}\check{P}_1 + \frac{1}{r}\partial_r\check{P}_1 - C_5\check{P}_1 - 2\frac{\partial_r U_0}{U_0-c}\partial_r\check{P}_1 = 0$, and $\check{P}_1$ satisfies the similar equation

$$\int_{r_a}^{r_b} \frac{C_5|\check{P}_1|^2 + |\partial_r\check{P}_1|^2}{|U_0-c|^2}rdr = \left[r\frac{\partial_r|\check{P}_1|^2}{|U_0-c|^2}\right]_{r_a}^{r_b} = 0. \tag{6.42}$$

Therefore, if U_0 is slowly varying in the spanwise direction, as in the case of no streaks, the forcing will be weak.

The schematic of overall interaction process is pictured in figure 6.20. The local self-

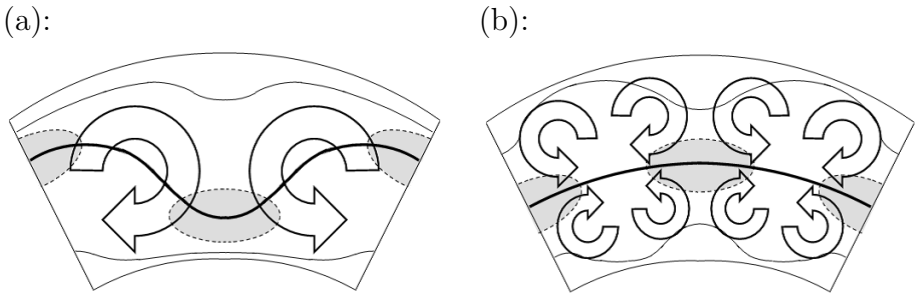

Figure 6.21: The schematic of a typical single-layer solution (left) and double-layer solution (right). The allows and lines represent the rolls and the contours of streaks respectively. The thick lines represent the critical layer. The grey elliptic ovals are the forced regions where the outward jets are induced.

sustaining mechanism explains why spatially localized roll patterns can be observed in subcritical shear flow transition. Indeed, spanwise localized solutions of PCF have been are recently found by Schneider *et al.* (2010), and the present theory can explain the mechanism of this solution. An important feature of equilibrated VWI type flow is that it requires an $O(1)$ streak modification to the basic flow as suggested in equation (6.41). However, note that if we consider the wavenumber dependence of the streak modification, this modification should be scaled by β when we assume the spanwise localization of flow field (c.f. section 4.3, where the mean flow of streamwise localized axisymmetric solution is discussed).

We note here that the homotopy behavior of the lower-branch double-layer solution is relatively robust in comparison with other branches; i.e. it is easy to continue such solutions when we change the geometry or the basic flow profile compared to the upper-branch solutions or lower branch single layer solutions. The mechanism stated above also enables to explain this difference in homotopy behaviours of the lower-branch single- and double-layer modes because the spatial distribution of locally forced region can be affected by the change of the basic flow and the geometry. The point is the critical layer must pass through the locally forced region where jets occur at the side of the rolls.

For single-layer type solutions, jets are created between two rolls and the wall. As a result, the critical layer is curved so that it gets close to both of the walls where the jets are created (figure 6.21 (a)). The peaks of the streak shear which produce these jets are due

to concentration of U_0 contours in a neighbourhood of the critical layer. It seems that one-sided forcing is also possible (figure 6.14 (d) and figure 6.15 (i)), but it is driven by the same mechanism.

In contrast, the critical layer is always located away from the walls for the double-layer solution. In this case, jets are induced between the two vortex layers (figure 6.21 (b)). As a consequence, the critical layer is nearly parallel to the walls, perpendicular to the basic flow gradient. In other words, the shear of the basic flow is almost uniform along the critical layer for the case of the planer-cylindrical homotopy. Because of this special property, the sustaining mechanism at the critical layer is maintained when the basic flow profile is varied along the homotopy of lower branch double-layer mode.

6.3.2 VWI process in high Reynolds number sliding Couette flow

Finally, we investigate VWI structure for high Reynolds number SCF solutions. The vortex system for a cylindrical coordinate system can be written as

$$V_0\partial_r U_0 + r^{-1}W_0\partial_\theta U_0 = G + \partial_{rr}^2 U_0 + r^{-1}\partial_r U_0 + r^{-2}\partial_{\theta\theta}^2 U_0 + F_x, \quad (6.43)$$

$$V_0\partial_r V_0 + r^{-1}W_0\partial_\theta V_0 - r^{-1}W_0^2 = -\partial_r P_0 + \partial_{rr}^2 V_0 + r^{-1}\partial_r V_0 + r^{-2}\partial_{\theta\theta}^2 V_0 - r^{-2}V_0 - 2r^{-2}\partial_\theta W_0 + F_r, \quad (6.44)$$

$$V_0\partial_r W_0 + r^{-1}W_0\partial_\theta W_0 + r^{-1}V_0 W_0 = -r^{-1}\partial_\theta P_0 + \partial_{rr}^2 W_0 + r^{-1}\partial_r W_0 + r^{-2}\partial_{\theta\theta}^2 W_0 - r^{-2}W_0 + 2r^{-2}\partial_\theta V_0 + F_\theta, \quad (6.45)$$

$$\partial_r V_0 + r^{-1}V_0 + r^{-1}\partial_\theta W_0 = 0. \quad (6.46)$$

Figure 6.22 shows the visualization of roll, streak and forcing calculated by above equations for double-layer class $\mathcal{M}$ solutions at $(\eta, R) = (1/42, 6\times10^4)$ (this radius ratio corresponds to that used by experimental work by Shands *et al.* 1980). In the figure, we can find typical roll, streak and forcing interaction described in the previous subsection (c.f. figure 6.20).

It is also possible to compare the forcing field $\mathbf{F} = F_r\mathbf{e}_r + F_\theta\mathbf{e}_\theta$ with the VWI asymptotic

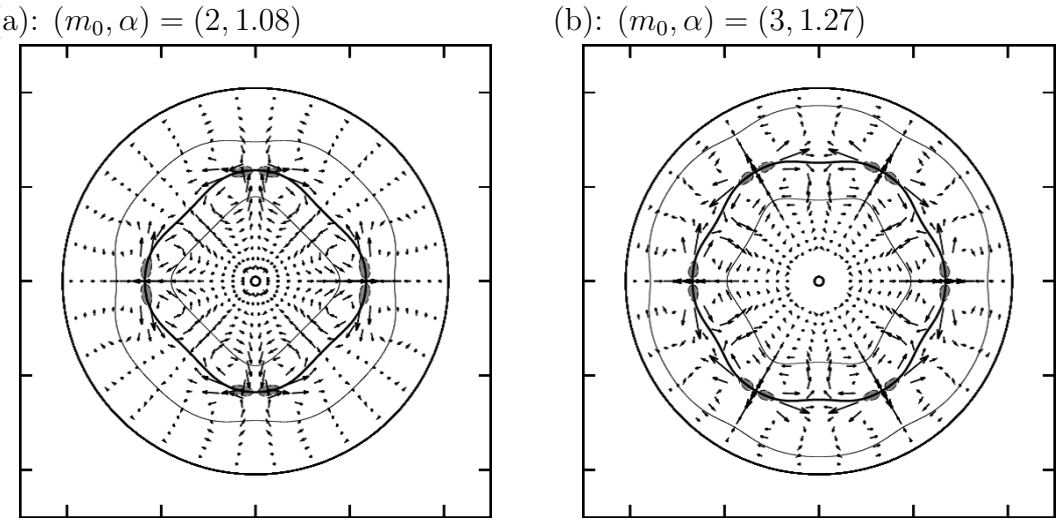

Figure 6.22: The visualizations of double layer class $\mathcal{M}$ solutions of SCF for $(\eta, R) = (1/42, 6 \times 10^4)$. The thick solid curves show the position of the critical layer $(U_0 - c) = 0$, while the thin curves show the position of the iso-contours $(U_0 - c) = 0.1 \times (U_0|_{r=r_a} - c)$ and $(U_0 - c) = 0.1 \times (U_0|_{r=r_b} - c)$. The vectors indicate roll velocity (V_0, W_0) and greyed ovals represent strongly forced regions where $|\mathbf{F}|$ is greater than half of its maximum.

calculation. The finite jump by Hall & Sherwin (2010) at the critical layer $r = r_c$ yields

$$\frac{r_c'}{r_c}[\partial_r W_0]_{r_c-}^{r_c+} = [\partial_r V_0]_{r_c-}^{r_c+} = \frac{r_c'}{r_c} J(\theta) \tag{6.47}$$

$$[P_0]_{r_c-}^{r_c+} = K(\theta) \tag{6.48}$$

where

$$J(\theta) = \frac{C_1}{a^{5/3}\Theta^5 r_c^3}\left\{\left(-\frac{7}{2}\frac{\Theta'}{\Theta} - \frac{5}{3}\frac{a'}{a} - 2\frac{r_c'}{r_c}\right)|\partial_\theta P_1|^2 + \partial_\theta|\partial_\theta P_1|^2\right\}, \tag{6.49}$$

$$K(\theta) = \frac{C_1}{a^{5/3}\Theta^5 r_c^3}\left(2\Theta - 1 - \frac{r_c''}{r_c}\right)|\partial_\theta P_1|^2, \tag{6.50}$$

$a = \alpha(\partial_r U_0)/\Theta$ and $\Theta = 1 + (r_c'/r_c)^2$. Integrating roll equations (6.45) and (6.46) across the critical layer, we obtain

$$K - \left(\frac{r_c'}{r_c}\right)\Theta J = \int_{r_c-}^{r_c+} F_r^\infty \frac{\partial_n U_0}{\partial_r U_0} dn = \frac{F_r^\infty}{\delta(n)}\frac{\partial_n U_0}{\partial_r U_0}, \tag{6.51}$$

$$-\left(\frac{r_c'}{r_c}\right)K - \Theta J = \int_{r_c-}^{r_c+} F_\theta^\infty \frac{\partial_n U_0}{\partial_r U_0} dn = \frac{F_\theta^\infty}{\delta(n)}\frac{\partial_n U_0}{\partial_r U_0}. \tag{6.52}$$

In figure 6.23, we plot the forcing at the critical layer, a good quantitative agreement

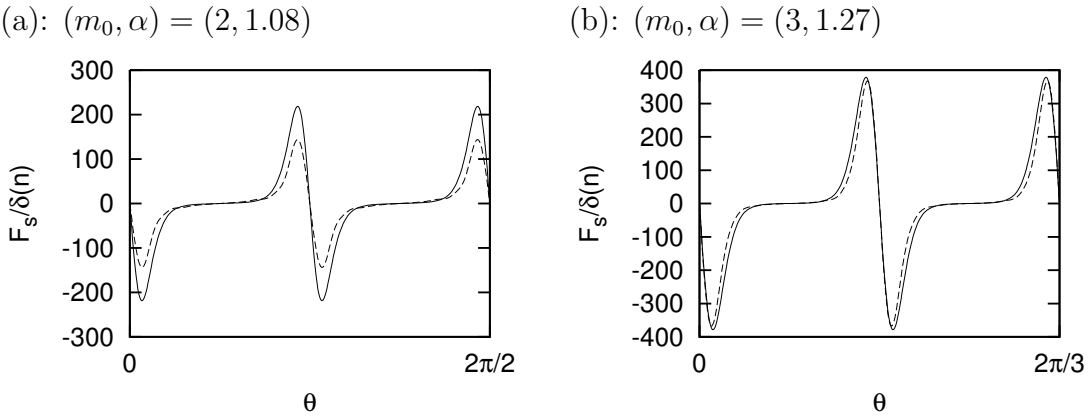

Figure 6.23: The tangential forcing at the critical layer $r = r_c$ for high Reynolds number SCF solutions. (a) and (b) correspond to those of figure 6.22. The solid lines represent exact calculations, $F_s\sqrt{2\pi}R^{-1/3}$, whereas the dashed lines represent VWI calculations, $F_s^{\infty}/\delta(n)$. The reader who notices that the sign difference to figure 6.17 should refer the notice in the beginning of section 5.1.

of the exact and the asymptotic form of tangential forcing F_s can be seen. Note that in the comparison, $\mathbf{e}_s = -\frac{\partial_\theta U_0}{r_c \partial_n U_0}\mathbf{e}_r + \frac{\partial_r U_0}{\partial_n U_0}\mathbf{e}_\theta$ and $\partial_n U_0 = \sqrt{(\partial_r U_0)^2 + (r_c^{-1}\partial_\theta U_0)^2}$. The delta function $\delta(n)$ is approximated by the same Gaussian function normal as in the last subsection.

6.4 Summary

The homotopy of three-dimensional solutions between flows with planar, cylindrical and circular cross-section has been developed. We started the homotopy from the solutions of SCF and continued to PCF and PF. The two types of mirror-symmetric solution found in section 5.2, one with a single-layer and the other with a double-layer streamwise vortex structure, were used as the starting points for the homotopies. The single- and double-layer structures belong to the same symmetry class and therefore mathematically can change from one to the other without bifurcation, and these structures are preserved along our homotopy paths.

It is found that the homotopy of the double-layer solution is relatively easy. As a result, we obtain solutions that include those of Itano & Generalis (2008) for PCF and Pringle & Kerswell (2007) for PF. Though the homotopy sometimes failed for upper-branch solutions,

we were always able to continue the lower branch solution between the three flows with distinct cross-sections, keeping $R \sim O(10^2)$. On the other hand, the resultant solution appears at a much higher Reynolds number than other known finite-amplitude solutions for PCF, while we were unable to continue the single-layer mode to PF.

For any η, all of the new solutions discovered in this thesis belong to class $\mathcal{M}$, i.e. these are mirror-symmetric travelling waves. According to table 6.1, where the list of solutions of PCF are summarized, our study provides the first discovery of class $\mathcal{M}$ solutions in PCF. For these solutions, it is found that there exist overlapped solution branches corresponding to positive and negative speed travelling-wave solutions. This degeneracy is resolved when the system's symmetry is imperfect due to the introduction of curvature.

The three-dimensional solutions obtained are characterized by their streamwise-averaged velocity field, i.e. roll-streak coherent structure. To sustain the streamwise averaged field, i.e. the "vortex", it is well known that we need nonlinear forcing from the streamwise fluctuation velocity field, the "wave". This forcing is the key of the sustaining mechanism of finite-amplitude solutions as explained in Waleffe's SSP and in VWI theory, which had been developed in the asymptotic field of study, and was recently applied to lower-branch exact coherent structures. We examine the forcing of the solutions obtained, and it is found that this forcing nucleates as a pair of positive-negative strong portions on the critical layer for lower-branch solutions. At the strongly forced region, outward jets in the roll component and the peak of the streak shear are commonly observed.

We use VWI theory as a basic tool and developed the self-sustaining process which can work locally as follows: the positive-negative forcing create outward tangential jets to the critical layer. These jets arise in the roll component and form a part of outer edge of the rolls. The rolls advect fast streaks to the critical layer so that the streak shear takes a maximum that amplifies the wave pressure, which in turn creates a strong force and so on. Though VWI theory is an asymptotic approach varied for asymptotically large R, it seems that the flow structures presented above can be observed for lower-branch solutions even at moderate Reynolds numbers.

As stated above, the local mechanism requires consistency of the roll structure and the critical layer, i.e. the critical layer must be sandwiched by rolls or a roll and a wall. The single-layer solutions is the latter case, for which there is a curved critical layer which significantly cuts across the basic shear layer. In contrast, the former case corresponds to the double-layer solutions, the critical layer is located between a double vortex pattern. This means that the shear of basic flow is almost constant along the critical layer which is nearly parallel to the wall in this case. Because this property is preserved even when the basic flow and boundary are changed, this double-layer solutions are therefore relatively easy to continue to other flow geometries by homotopy.

6.A Appendix

6.A.1 Homotopy of axisymmetric solutions

(i) *Towards plane Couette flow*

One might ask about the connection between the present two-dimensional solutions for SCF presented in chapter 4 with similar two-dimensional streamwise localized solutions in PCF, which have been discussed in shear flow transition community. Such two-dimensional solutions in PCF are first obtained by homotopy continuation of Tollmien-Schlichting wave solutions in plane Poiseuille flow to PCF, decreasing pressure gradient and adding mutual motion of upper and lower walls (Cherhabili & Ehrenstein 1995, we call this solution 2DEQ hereafter). However, the question of the existence of this solution is still not confirmed due to its problematical sensitivity to the number of Fourier modes in the streamwise direction (Rincon 2007, Ehrenstein *et al.* 2008). Though similar states have been discovered in slightly perturbed PCF by using different axial discretization method by Barkley & Tuckerman (1999), Mehta (2004) and Mehta & Healey (2005), corresponding solutions in pure PCF have not yet been discovered.

To make a comparison with 2DEQ, we continue the solution branch of SCF to PCF. The

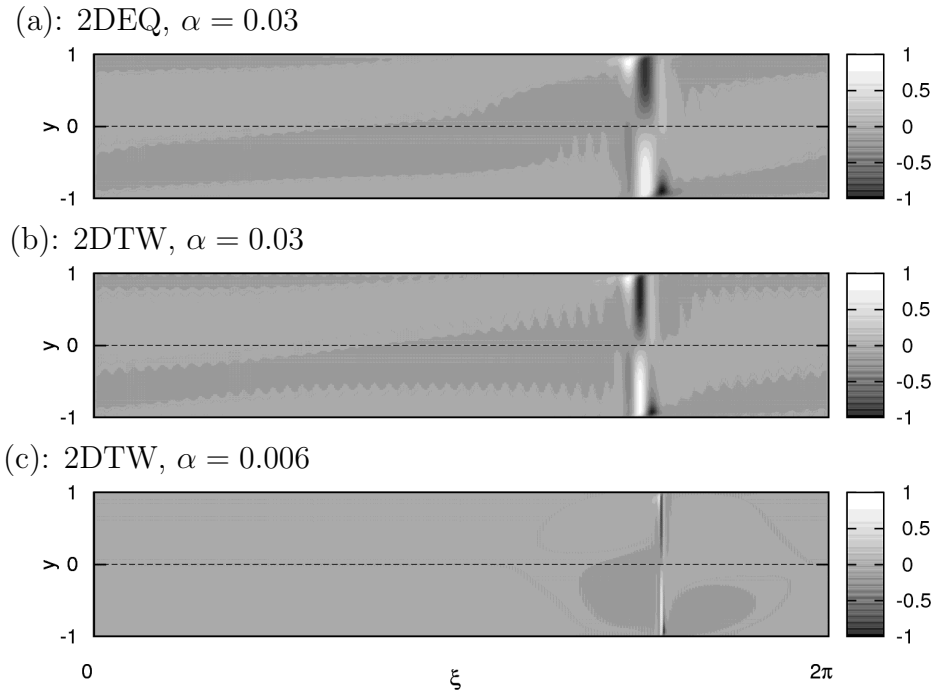

Figure 6.24: The axial fluctuation velocity field $\tilde{u}/R$ for the two-dimensional solutions for PCF with $(\eta, R) = (1,\ 5300)$. The truncation level $(L, N) = (39, 60)$ is used for (a) and (b) while $(L, N) = (39, 250)$ is used for (c). The dashed lines represent the locations of the critical layers.

continuation is successful if we use a low resolution level and we label this solution as 2DTW. The resultant solution is compared to 2DEQ in figure 6.24 (a) and (b) under the same calculation conditions. Though the visualization shows similar streamwise localized pattern, these solutions are distinct. The crucial difference of these solutions is that 2DTW does not possesses symmetry about the mid-gap observed in 2DEQ (i.e. 2DEQ is a steady solution whereas 2DTW is a travelling-wave solution).

Figure 6.25 shows the results of resolution test of these solutions. This figure shows all coefficients including leading parts are sensitive to the resolution, in contrast to figure 4.18. In addition, there exists the upper bound of resolution: it is not possible to increase N from 120 to 121 for 2DEQ, from 63 to 64 for 2DTW for fixed values of the physical parameters. It is possible to increase N if we decrease α as in figure 6.24 (c), however, another difficulty comes up. This can be seen in figure 6.26, where the axisymmetric solutions obtained is plotted in η–(αR) parameter space. From the figure, we can see the solution in figure 6.24 (c) violates the energy criteria in Appendix 4.A.2 while all other computation conducted

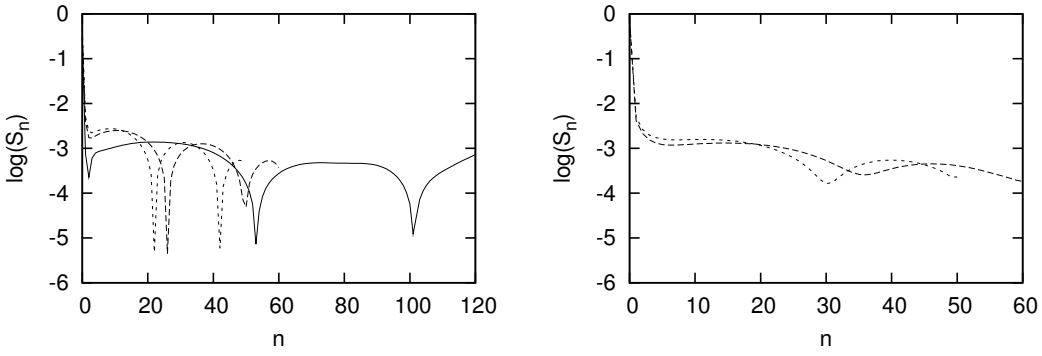

Figure 6.25: The spectral intensity $S_n = \left|\overline{ue^{-in\xi}}\right| |_{y=y_c}/R$ for various streamwise truncation level N. The parameters used are the same as those of figure 6.24. The truncation level in wall-normal direction is fixed to $L = 39$. Left/right figures represent the results for 2DEQ / 2DTW. The solid, dashed and dotted curves represent the results with $N = 120$, $N = 60$ and $N = 50$, respectively.

in this paper is comfortably settled within the energy boundary.

In view of all the above unphysical behaviours, we conclude that any solutions found above the existence threshold of axisymmetric solutions determined by reliable computation in subsection 4.1 to be $\eta_{\max} = 0.33$–0.40, are numerical artifacts. This conclusion is consistent to non-existence of nonlinear two-dimensional asymptotic structure of PCF (c.f. section 4.2). Although the solution 2DTW does not exist for pure PCF, it may have some relevance to perturbed PCF as for 2DEQ.

(ii) *Towards pipe flow*

Homotopy of localized axisymmetric solutions from SCF to PF is also an interesting subject, because it is widely known that localized disturbances, called 'puffs', are frequently found in pipe flow experiments. To find solution of PF, we add axial pressure gradient to axisymmetric solution found in section 4.1 fixing $\eta = 0.1$.

However, R_p does not reach the parabolic limit $R_p/R = \Pi \approx 0.46$, even when R and α are adjusted. As a result of the optimization of R_p/R, it is found that long-wave and high R situation is preferred. The maximum R_p/R achieved within our computational restriction is 0.41. We confirm further increasing of R nor decreasing of η does not so much improve this value. As for SCF–PCF case, the requirement of long-wave structure in this limit

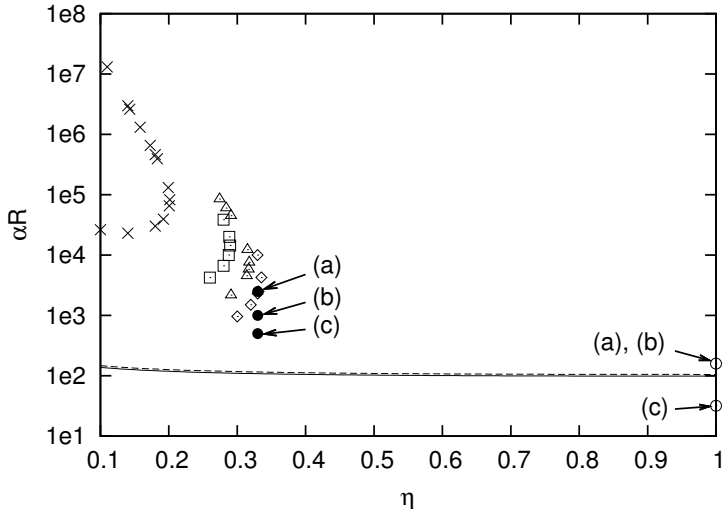

Figure 6.26: The η–αR parameter space plot of the solutions obtained in this section and chapter 4 together with the energy boundary for $\alpha = 0$ (solid line) and $\alpha = 0.6546$ (dashed line). The marks $\times, \square, \triangle$ and $\diamond$ represent the existence edges of LR modes for $\alpha = 0.6546, 0.2, 0.1$ and 0.05 (same points as figure 4.6). The filled and open circles correspond to the solutions in figure 4.16 and figure 6.24, respectively.

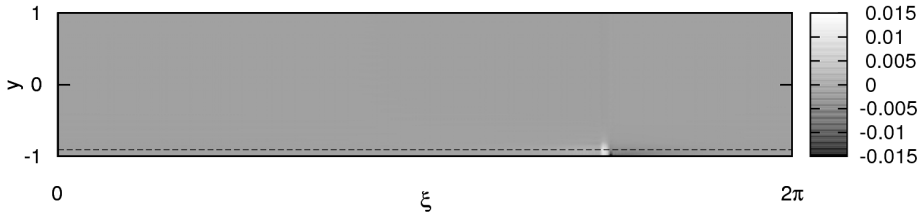

Figure 6.27: The axial fluctuation velocity field $\tilde{u}/R$ for the axisymmetric solution with $(\eta, R, R_p, \alpha) = (0.1,\ 5.2 \times 10^6,\ 0.41R,\ 0.01)$. The truncation level $(L, N) = (58, 212)$ is used. The dashed line represents the location of the critical layer.

corresponds to the long-wave breakdown of two-dimensional asymptotic structure, which inhibits high R axisymmetric asymptotic theory of PF (c.f. section 4.2 and 4.3). In order to maintain long-wave version of asymptotic structure, $O(1)$ mean-flow modification is needed since Rayleigh equation cannot have a solution if the mean flow is close to a parabola.

The mean flow for $R_p/R = 0.41$ is pictured in figure 6.28. As the figure shows the modification part is very weak compared to the basic flow and the total mean-flow profile is close to the parabolic profile. This phenomena suggests that the failure of the continuation to PF is due to the absence of nonlinear asymptotic structure.

Other evidence for the result that solutions cannot be continued to PF, is that the strongest velocity fluctuation on the critical layer is confined to the inner wall (figure 6.27). Thus

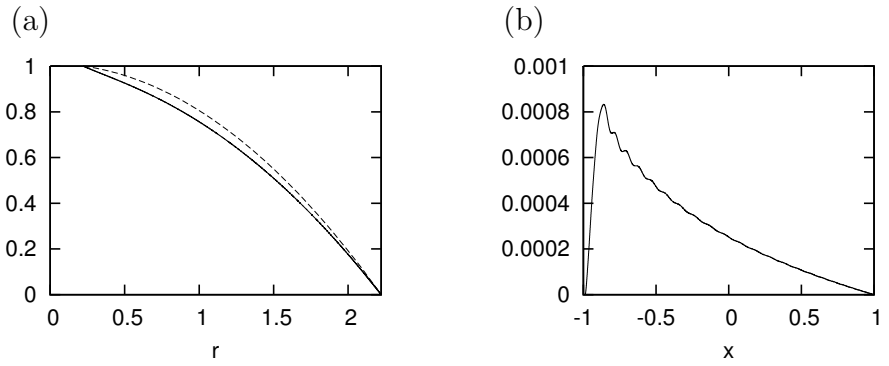

Figure 6.28: The mean flow of the axisymmetric solution with $(\eta, R, R_p, \alpha) = (0.1, 5.2\times10^6, 0.41R, 0.01)$. The truncation level $(L, N) = (58, 212)$ is used. (a): The total mean flow $\overline{U}/R$ (solid line) and the parabolic base flow profile (dashed line), where the parameter R_p/R takes $\Pi \approx 0.46$. (b): The mean-flow distortion $\overline{u}/R$.

removal of the inner cylinder in the homotopy would destroy the sustaining mechanism of the solution.

We, therefore, conclude that there is little hope for two-dimensional counterpart of homotopy path from SCF to PF solutions.

Chapter 7

Conclusion

This thesis has considered the problem of flow between two infinitely long co-axial cylinders mutually sliding in the axial direction, called sliding Couette flow (SCF). A number of finite-amplitude solutions are discovered and compared to theoretical large Reynolds number asymptotic structures. Also, homotopy connections between the solutions of SCF and those of plane Couette flow (PCF) and pipe flow (PF) are considered.

Let us conclude the stability properties of SCF in the R–η parameter plane in figure 7.1.

Our linear stability analysis with respect to axisymmetric and non-axisymmetric disturbances shows that the basic flow of SCF exhibits linear instability only to axisymmetric disturbances (chapter 3). As shown in the figure, the instability exists at $R > O(10^6)$ when $\eta < 0.1415$, where the long-wave cut-off occurs.

From these linear neutral points, the branch of axisymmetric finite-amplitude travelling wave solutions bifurcates subcritically (chapter 4). Along the branch Reynolds number can be reduced to around $O(10^4)$. The flow field of this type of solution is characterized by distinct wall boundary layers and a nonlinear critical layer structure qualitatively agreeing with the nonlinear axisymmetric asymptotic theory that is developed in the same chapter. The critical layer structure is sensitive to the basic flow profile, which in turn depends on η. Indeed, both the numerical and asymptotic solutions cannot be continued beyond at

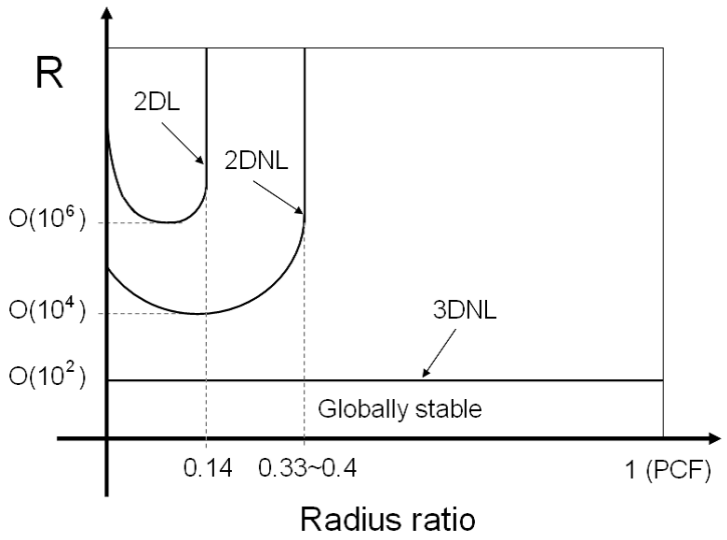

Figure 7.1: The schematic illustration of the stability property of SCF. Depicted are the stability boundaries for two-dimensional linear (2DL), two-dimensional nonlinear (2DNL) and three-dimensional nonlinear (3DNL) perturbations. Below the 3DNL threshold, SCF is globally stable, i.e. any disturbance decay ultimately.

some value of η, estimated to be around 0.33–0.40. Our computations suggest that these nonlinear cut-offs occur in the long-wave limit as for the linear instability. The long-wave situation breaks the multi-layered asymptotic flow structure and a streamwise localized disturbance emerges instead.

In SCF, there also exist three-dimensional, non-axisymmetric solutions with various kinds of symmetric streamwise roll structure (chapter 5 and 6). Most of these solutions arise in a saddle-node bifurcation at $R \sim O(10^2)$ for wide range of values of the radius ratio, at least from $\eta = O(10^{-1})$ to narrow-gap limit $\eta = 1$, i.e. PCF. Thus even when the two-dimensional instability is absent in SCF, turbulence could be triggered by a three-dimensional streamwise roll type instability as has been observed in other shear flows. The asymptotic structure of the non-axisymmetric solutions can be well explained by VWI theory. In contrast to two-dimensional asymptotic theory, the VWI structure is sustained via streamwise rolls, which can be present in shear flows with any cross-section. This is consistent to the absence of cut-off behaviour for the non-axisymmetric solutions, i.e. the solutions do not vanish as η varies. Further, our observations elucidate that a spanwise localized roll structure can also sustain this type of solution.

Now the overall stability properties of SCF are summarized. The results suggest that for any η, the global stability boundary of SCF, below which the flow always ultimately returns to the laminar flow, is determined by the three-dimensional nonlinear stability boundary at $R \sim (10^2)$, since there is no solution on which the turbulent trajectory hangs.

A schematic illustration of the finite-amplitude solution branches for $\eta < 0.1415$ is presented in figure 7.2. With increasing η, the two-dimensional solution branch detaches from the linear instability at $\eta = 0.1415$ and finally disappear at $\eta = 0.33 - 0.40$. For both two- and three-dimensional solutions, the lower-branch solutions show quantitative agreement with asymptotic theory, while the asymptotic structure of the upper-branch solutions remains an open problem.

All of these numerical investigations indicate subcritical transition to turbulence in SCF, though the evidence for such a phenomenon has yet to be observed in experiment or simulation studies. As R is increased, the present results suggest that the flow would first encounter a three-dimensional instability triggered by the lower-branch three-dimensional solutions, whose asymptotic structure is governed by VWI theory. However, we note here that one of the notable properties of the axisymmetric asymptotic solution, and one which agrees with the asymptotic behaviour of the numerically-computed two-dimensional lower branch solutions, is that all disturbances decay as R is increased. This means that when we consider practical laminar flow control at high R, the two-dimensional Tollmien-Schlichting type flow structure could become more important than the VWI type streamwise roll equilibrated states, which require an $O(1)$ modification of the mean flow, because it would be 'closer' to laminar flow in the sense of disturbance magnitude (e.g. disturbance norm or energy). Thus it is likely that the axisymmetric solutions opens up the route to transition first in some cases. We also note here that for moderate R, it is known that an $O(R^{-1})$ streamwise roll can trigger shear-flow transition by the lift-up mechanism (e.g. Darbyshire & Mullin 1995, Hof *et al.* and Lemoult *et al.*). When R is sufficiently large, the axisymmetric solutions, which have $O(R^{-1/6})$ deviation from the basic flow, would also affect this route to transition where the magnitude of the disturbance evolves from $O(R^{-1})$ to an $O(1)$ size.

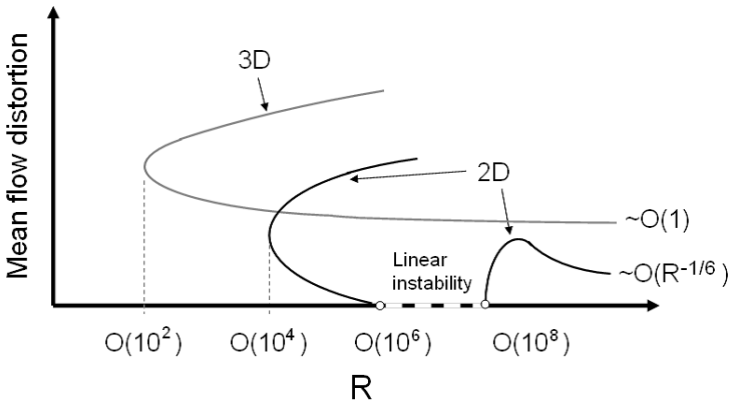

Figure 7.2: Schematic illustration of the bifurcation diagram of SCF when $\eta < 0.1415$.

Although the present thesis mainly concentrates on SCF, the story presented above would be commonly observed for a one-parameter family of flows which exhibit linear instability below a critical value of that parameter. For these flows, it is often found that, as the critical value is approached, the linearly unstable region due to Tollmien-Schlichting wave type two-dimensional instability recedes to $R \to \infty$ with the wavenumber scaling as $O(R^{-1})$ (e.g. see Cowley & Smith (1985) for plane Couette-Poiseuille flow and Gittler (1993) for annular Couette-Poiseuille flow, the corresponding generalization to a cylindrical geometry). The present study suggests that there also exists a long-wave cut-off for two-dimensional nonlinear instabilities, e.g. finite-amplitude solutions for plane Couette-Poiseuille flow (Cherhabili & Ehrenstein 1995) and annular Couette-Poiseuille flow (Wong & Walton 2012). Although only the two-dimensional results are known for these flows, the existence of three-dimensional solutions is a promising area of future work. Such solutions would easily be obtained by homotopy continuation from our three-dimensional solutions.

SCF also has a strong connection to PF. We can continue non-axisymmetric solutions of SCF to the PF solution (chapter 6). Also, the axisymmetric solutions presented here are particularly interesting since they appear to have some connection to the initiation of localized turbulent spots. However, it should be noted that our solutions of SCF cannot be linked directly to fully developed 'puffs' in pipe flow, because the axisymmetric asymptotic solution presented in this study does not exist in pipe flow (see remark at the beginning of section 4.2 and Appendix 6.A.1). Instead, by analogy with our results, it might be expected

that a more relevant asymptotic model for that situation would be the spiral wave structure given by Smith & Bodonyi (1982a), and in particular its long-wave limit, which gives a threshold amplitude for the instability. The continuation method developed in this thesis serves to find one of the possible root to this type of solution together with the similar spiral wave linear instability of annular Couette-Poiseuille flow (Walton 2005). Another probable modification for the starting point of continuation is introduction of artificial body force which distorts the mean flow as in Smith & Bodonyi (1982a)'s asymptotic theory. If such a force can induce linear instability in pipe flow, it thus yields another possible starting point for finding such spiral solutions.

Further advanced applications of the present work include investigation of the transition control of curved external boundary-layer flow surrounding an object in flight where we have to additionally consider the spatial development of the disturbance. Despite the large extension from the present SCF work, where the flow is homogeneous in the streamwise direction, it is clearly of interest to apply our results to such a configuration, which is more relevant to practical problems. In particular, our finding of the agreement of two-dimensional asymptotic and numerical solutions could help to control the Tollmien-Schlichting waves, which are the first instability from the leading edge in spatial developing boundary layer problems. Furthermore, the local self-sustaining mechanism we found can be used to control successive three-dimensional streamwise roll type disturbances: it should be possible to eliminate the embryo of the growing disturbance with a minimal effort, by breaking the local roll-streak-wave balance.

Bibliography

Arney, M. S., Bai, R., Guevara, E., Joseph, D. D. & Liu, K. 1993 Friction factor and holdup studies for lubricated pipelining-I: experiments and correlations. *Intl J. Multiphase Flow* **19**, 1061–1076.

Barkley, D. & Tuckerman, L. S. 1999 Stability analysis of perturbed plane Couette flow. *Phys. Fluids* **11**, 1187–1195.

Bech, K. H., Tillmark, N. & Alfredsson, P. H. 1995 An investigation of turbulent plane Couette flow at low Reynolds numbers. *J. Fluid Mech.* **286**, 291–325.

Bottin, S., Dauchot, O. & Daviaud, F. 1997 Intermittency in a locally forced plane Couette flow. *Phys. Rev. Lett.* **79**, 4377–4380.

Bottin, S., Dauchot, O. & Daviaud, F. 1998 Experimental evidence of streamwise vortices as finite amplitude solutions in transitional plane Couette flow. *Phys. Fluids* **10**, 2597–2607.

Benney, D. J. & Bergeron, R. F. 1969 A new class of nonlinear waves in parallel flows. *Stud. Appl. Math.* **48**, 181–204.

Bodonyi, R. J., Smith, F. T. & Gajjar, J. 1983 Amplitude-dependent stability of boundary layer flow with a strongly nonlinear critical layer. *IMA J. Appl. Math.* **30**, 1–19.

Brown, S. N. & Stewartson, K. 1978 The evolution of a small inviscid disturbance to a marginally unstable stratified shear flow; stage two. *Proc. R. Soc. Lond.* A **363**, 174–194.

Cherhabili, A. & Ehrenstein, U. 1995 Spatially localized two-dimensional equilibrium states in plane Couette flow. *Eur. J. Mech. B/Fluids* **14**, 677–696.

Chida, K., Sakaguchi, S., Wagatsuma, M. & Kimura, T. 1982 High-speed coating of optical fibres with thermally curable silicone resin using a pressurised die. *Electron. Lett.* **18**(16), 713–715.

Cipolla, K. M. & Keith, W. L. 2003 High Reynolds number thick axisymmetric turbulent boundary layer measurements. *Exp. Fluids* **35**, 477–485.

Cvitanović, P., Artuso, R., Mainieri, R. Tanner, G. & Vattay, G. 2011 *Chaos: Classical and Quantum.*, Copenhagen: Niels Bohr Inst.

Clever R. M. & Busse, F. H. 1997 Tertiary and quaternary solutions for plane Couette flow. *J. Fluid Mech.* **344**, 137–153.

Cowley, S. J. & Smith, F. T. 1985 On the stability of Poiseuille-Couette flow: a bifurcation of infinity. *J. Fluid Mech.* **156**, 83–100.

Daviaud, F., Hegseth, J. & Berg, P. 1992 Subcritical transition to turbulence in plane Couette flow. *Phys. Rev. Lett.* **69**, 2511–2514.

Darbyshire, A. G. & Mullin, T. 1995 Transition to turbulence in constant-mass-flux pipe flow. *J. Fluid Mech.* **289**, 83–114.

Davies, S. J. & White, C. M. 1928 An experimental study of the flow of water in pipes of rectangular section. *Proc. Roy. Soc. A* **119**, 92–107.

Davis, R. E. 1969 On the high Reynolds number flow over a wavy boundary. *J. Fluid Mech.* **36**, 337–346.

Drazin, P. G. & Reid, W.H. 1981 *Hydrodynamic Stability.* Cambridge University Press.

Ehrenstein, U., Nagata, M. & Rincon, F. 2008 Two-dimensional nonlinear plane Poiseuille-Couette flow homotopy revisited. *Phys. Fluids* **20**, 064103.

Eisen, H., Heinrichs, W. and Witsch, K. 1991 Spectral collocation methods and polar coordinate singularities *J. Comput. Phys.* **96**, 241–257.

Faisst, H. & Eckhardt, B. 2003 Traveling waves in pipe flow. *Phys. Rev. Lett.* **91**, 224502.

Frei, Ch., Lüscher, P & Wintermantel, E. 2000 Thread-annular flow in vertical pipes. *J. Fluid Mech.* **410**, 185–210.

Gibson, J. F., Halcrow, J. & Cvitanovic, P. 2008 Visualizing the geometry of sate-space in plane Couette flow. *J. Fluid Mech.* **611**, 107–130.

Gibson, J. F., Halcrow, J. & Cvitanovic, P. 2009 Equilibrium and travelling-wave solutions of plane Couette flow. *J. Fluid Mech.* **638**, 243–266.

Gittler, Ph. 1993 Stability of Poiseuille-Couette flow between concentric cylinders. *Acta Mechanica.* **101**, 1–13.

Haberman, R. 1972 Critical layers in parallel flows. *Stud. Appl. Math.* **51**, 139–161.

Hall, P. & Horseman, N. J. 1991 The linear inviscid secondary instability of longitudinal vortex structures in boundary layers. *J. Fluid Mech.* **232**, 357–375.

Hall, P. & Sherwin, S. 2010 Streamwise vortices in shear flows: harbingers of transition and the skeleton of coherent structures. *J. Fluid Mech.* **661**, 178–205.

Hall, P. & Smith, F. T. 1991 On strongly nonlinear vortex/wave interactions in boundary-layer transition. *J. Fluid Mech.* **227**, 641–666.

Healey, J. J. 1991 On the neutral curve of the flat-plate boundary layer: comparison between experiment, Orr-Sommerfeld theory and asymptotic theory. *J. Fluid Mech.* **288**, 59–73.

Henningson, D., Spalart, P. & Kim, J. 1987 Numerical simulations of turbulent spots in plane Poiseuille and boundary-layer flow. *Phys. Fluids* **30**(10), 2914–2917.

Herbert, Th. 1976 Periodic secondary motions in a plane channel. *Proc. Int. Conf.*

on Numer. Methods Fluid Dyn., 235. Springer.

Hof, B., van Doorne, C. W. H., Westerweel,J. & Nieuwstadt, F. T. M. 2005 Turbulence regeneration in pipe flow at moderate Reynolds numbers. *Phys. Rev. Lett.* **95**, 214502.

Hof, B., van Doorne, C. W. H., Westerweel,J., Nieuwstadt, F. T. M., Faisst, H., Eckhardt, B., Wedin, H. Kerswell, R. R. and Waleffe, F. 2004 Experimental observation of nonlinear traveling waves in turbulent pipe flow. *Science* **305**(5690), 1594–1598.

Itano, T. & Generalis, S. C. 2009 Hairpin vortex solution in plane Couette flow: a tapestry of knotted vortices. *Phys. Rev. Lett.* **102**, 114501.

Itano, T. & Toh, S. 2001 The dynamics of bursting process in wall turbulence. *J. Phys. Soc. Jpn.* **70**, 703–716.

Joseph, D. D. 1976 *Stability of Fluid Motions, Vols I and II.* Springer.

Joseph, D. D. & Carmi, S. 1969 Stability of Poiseuille flow in pipes, annuli, and channels. *Quart. Applied Math.* **26**, 575–599.

Judd, K. L., Kubler, F. & Schmedders, K. 2000 Computing equilibria in infinite-horizon finance economics: the case of one asset. *J. econ. dyn. control.* **24**, 1047–1078.

Kawahara, G. & Kida, S. 2001 Periodic motion embedded in plane Couette turbulence: regeneration cycle and burst. *J. Fluid Mech.* **449**, 291–300.

Kida, S. 1985 Three-dimensional periodic flows with high-symmetry. *J. Phys. Soc. Jpn.* **54**(6), 2132–2136.

Lemoult, G., Aider, J. & Wesfreid. 2012 Experimental scaling law for the sub-critical transition to turbulence in plane Poiseuille flow. **Phys. Rev. E 85**, 025303(R).

de Lozar, A., Mellibovsky, F., Avila, M. & Hof, B. 2012 Edge state in pipe flow experiments. *Phys. Rev. Lett.* **108**, 214502.

Melville, R. C., Trajković, L., Fang, S. & Watson, L. T. 1993 Artificial parameter homotopy methods for the DC operating point problem. *IEEE Trans. Computer-Aided Design* **12**(6), 861–877.

Meseguer, A. & Trefethen, L. N. 2003 Linearized pipe flow to Reynolds number 10^7. *J. Comp. Phys.* **186**, 178–197.

Marques, F. 1990 On boundary conditions for velocity potentials in confined flows: Application to Couette flow. *Phys. Fluids A* **A2**, 729–737.

Mehta, P. G. 2004 A unified well-posed computational approach for 2D Orr-Sommerfeld problem. *J. Comput. Phys.* **199**(2), 541–557.

Mehta, P. G. & Healey, T. J. 2005 On steady solutions of symmetry-preserving perturbations of the two-dimensional Couette flow problem. *Phys. Fluids* **17**, 094108.

Nagata, M. 1990 Three-dimensional finite amplitude solutions in plane Couette flow: bifurcation from infinity. *J. Fluid Mech.* **217**, 519–527.

Nagata, M. 1997 Three-dimensional traveling-wave solutions in plane Couette flow. *Phys. Rev. E* **55**, 2023–2025.

Nishioka, M., Iida, S. and Ichikawa, Y. 1975 An experimental investigation of the stability of plane Couette flow. *J. Fluid Mech.* **72**(4), 731–751.

Orszag, S. A. & Kells, L. C. 1980 Transition to turbulence in plane Poiseuille and plane Couette flow. *J. Fluid Mech.* **72**(4), 731–751.

Panoliaskos, A., Hallett, W. L. H. & Garis, I. 1985 Prediction of optical fiber coating thickness. *Appl. Opt.* **24**, 2309–2312.

Preziosi, L. & Rosso, F. 1990 Stability of a viscous liquid between sliding pipes. *Phys. Fluids A* **2**(7), 1158–1162.

Pringle, C. C. T., Duguet, Y. & Kerswell, R. R. 2009 Highly symmetric travelling waves in pipe flow. *Phil. Trans. R. Soc. A* **367**, 457–472.

Pringle, C. C. T. & Kerswell, R. R. 2007 Asymmetric, herical and mirror-symmetric travelling waves in pipe flow. *Phys. Rev. Lett.* **99**(2), 074502.

Reynolds, O. 1883 An experimental investigation of the circumstances which determine whether the motion of water shall be direct or sinuous and the law of resistance in parallel channels. *Phil. Trans. R. Soc.* **174**, 935–982.

Rincon, F. 2007 On the existence of two-dimensional nonlinear steady states in plane Couette flow. *Phys. Fluids* **19**, 074105.

Romanov, V. A. 1973 Stability of plane parallel Couette flow. *Funct. Anal. Appl.* **7**, 137–146.

Serrin, J. 1959 On the stability of viscous fluid motions. *Arch. Rat. Mech. Anal.* **3**, 1–13.

Schlichting, H. 1933 Laminare Strahlenausbreitung. *Z. Angew Math. Mech.* **13**, 260–263.

Schmiegel, A. 1999 Transition to turbulence in linearly stable shear flows. PhD thesis. Philipps-Universität Marburg.

Schneider, T. M., Gibson, J. F. & Burke, J. 2010 Snakes and ladders: localized solutions of plane Couette flow. *Phys. Rev. Lett.* **104**, 104501.

Shands, J., Alfredsson, H. & Lindgren, E. R. 1980 Annular pipe flow subject to axial motion of the inner boundary. *Phis. Fluids.* **23**(10), 2144–2145.

Shimizu, M. & Kida, S. 2009 A driving mechanism of a turbulent puff in pipe flow. *Fluid Dyn. Res.* **41**, 045501.

Skufca, J. D., Yorke, J. A. & Eckhardt, B. 2006 Edge of chaos in a parallel shear flow. *Phys. Rev. Lett.* **96**, 174101–174104.

Smith, F. T. & Bodonyi R. J. 1982a Amplitude-dependent neutral modes in the Hagen-Poiseuille flow through a circular pipe. *Proc. R. Soc. Lond.* A **384**, 463–489.

Smith, F. T. & Bodonyi R. J. 1982b Nonlinear critical layers and their development in streaming-flow instability. *J. Fluid Mech.* **118**, 165–185.

Tadmor, Z. & Bird, R. B. 1974 Rheological analysis of stabilizing forces in wire-coating dies. *Polym. Eng. Sci.* **14**(2), 124–136.

Tollmien, W. 1929 Uber die Entstehung der Turbulenz. *Nachr. Ges. Wiss. Gottingen Math-Pyhs. Kl. II*, 21–44.

Tutty, O. R. 2008 Flow along a long thin cylinder. *J. Fluid Mech.* **602**, 1–37.

Vaskopulos, T., Polymeropoulos, C. E. & Zebib, A. 1993 Heat transfer from optical fibre during the drow process. *J. Mat. Proc. Manuf. Sci.* **1**, 261–271.

van Veen, L. & Kawahara, G. 2011 Homoclinic tangle on the edge of shear flows. *Phys. Rev. Lett.* **107**, 114501.

Viswanath, D. 2009 The critical layer in pipe flow at high Reynolds number. *Phil. Trans. R. Soc. A* **367**, 561–576.

Waleffe, F. 1995 Hydrodynamic stability and turbulence: beyond transients to a self-sustaining process. *Stud. Appl. Math.* **95**, 319–343.

Waleffe, F. 1998 Three-dimensional coherent states in plane shear flows. *Phys. Rev. Lett.* **81**(19), 4140–4143.

Waleffe, F. 2003 Homotopy of exact coherent structures in plane shear flows. *Phys. Fluids* **15**(6), 1517–1534.

Walton, A. G. 2002 The temporal evolution of neutral modes in the impulsively started flow through a pipe of circular cross-section. *J. Fluid Mech.* **457**, 339–376.

Walton, A. G. 2003 The nonlinear instability of thread-annular flow at high Reynolds number. *J. Fluid Mech.* **477**, 227–257.

Walton, A. G. 2004 Stability of circular Poiseuille-Couette flow to axisymmetric disturbances. *J. Fluid Mech.* **500**, 169–210.

Walton, A. G. 2005 The linear and nonlinear stability of thread-annular flow. *Phil. Trans. R. Soc. A* **363**, 1223–1233.

Walton, A. G. 2011 The stability of developing pipe flow at high Reynolds number and the existence of nonlinear neutral centre modes. *J. Fluid Mech.* **684**, 284–315.

Wang, J., Gibson, J. F. & Waleffe, F. 2007 Lower branch coherent states in shear flows: transition and control. *Phys. Rev. Lett.* **98**, 204501.

Wedin, H. & Kerswell, R. R. 2004 Exact coherent structures in pipe flow: travelling wave solutions. *J. Fluid Mech.* **508**, 333–371.

Willis, A. P. & Kerswell, R. R. 2008 Coherent structures in localised and global pipe turbulence. *Phys. Rev. Lett.* **100**, 124501.

Wong, A. W. H. & Walton, A. G. 2012 Axisymmetric travelling waves in annular Couette-Poiseuille flow. *Q. J. Mech. Appl. Math.* **65**, 293–311.

Zahn, J. P., Toomre, J., Spiegel, E. A. & Gough, D. O. 1974 Nonlinear cellular motions in plane Poiseuille channel flow. *J. Fluid Math.* **64**, 319–345.

Zernike, F. 1934 Beugungstheorie des Schneidenverfahrens und Seiner Verbesserten Form, der Phasenkontrastmethode. *Physica.* **1**, 689–704.